Significant improvement of photoresponsivity of $BaSi_2$ passivated by atomic H and exploring the H states via muon spin rotation

Xu Zhihao

February 2021

Significant improvement of photoresponsivity of $BaSi_2$ passivated by atomic H and exploring the H states via muon spin rotation

Xu Zhihao

Doctoral Program in Nano-Science and Nano-Technology

Submitted to the Graduate School of

Pure and Applied Sciences

in Partial Fulfillment of the Requirements

for the Degree of Doctor of Philosophy in

Engineering

at the

University of Tsukuba

Abstract

Solar cells have been developed over half of a century and applied in daily life. A high conversion efficiency (η) is always expected to achieve via new materials or technologies. Nowadays, thin-film solar cells composed of materials such as CdTe, CIGS, and organic-inorganic perovskite have attracted increasing attention owing to their low cost and high η. However, these materials contain toxic or scarce elements. Considering these circumstances, we have focused on semiconducting material barium disilicide ($BaSi_2$). It has attractive features for solar cell applications such as a suitable band gap of 1.3 eV for a single-junction solar cell, high absorption coefficients exceeding those of CIGS, a long minority-carrier lifetime above 10 μs, and a large minority-carrier diffusion length of 10 μm due to inactive grain boundaries. Furthermore, epitaxial $BaSi_2$ thin films can be grown on Si(111) and Si(100) substrates by molecular beam epitaxy. The lattice mismatch between the Si substrate and $BaSi_2$ thin film is small. Because of these advantages, $BaSi_2$ has a great potential to be solar cells or a light absorber layer in thin-film solar cell applications. Recently, we achieved an η approaching 10% in p-$BaSi_2$/n-Si. However, in this solar cell, the built-in potential is as small as 0.2 V because of the low electron affinity of $BaSi_2$ (3.2 eV). The experimentally obtained open-circuit voltage is thus smaller than 0.5 V, limiting the η. Hence, we next moved on to $BaSi_2$ homojunction solar cells and first demonstrated that the operation of $BaSi_2$ homojunction solar cells on the p^+-Si substrate. To achieve high η in homojunction solar cells, the formation of high-quality $BaSi_2$ light absorber layer is important.

According to a first-principle calculation, from the viewpoint of formation energy, Si vacancies are more likely to locate at Si(3) sites in the Si tetrahedron and act as point defects in $BaSi_2$ regardless of whether the growth conditions are rich or poor in Si. The calculation also revealed that Si vacancies generate dangling bonds and thereby localized states within the band gap, leading to the degradation of the minority-carrier properties of $BaSi_2$. The defects in $BaSi_2$ films and bulk polycrystalline $BaSi_2$ has also been measured by deep-level transient spectroscopy, Raman spectroscopy, electron paramagnetic resonance, and photoluminescence. Therefore, passivation of defects in $BaSi_2$ is particularly important for their use in solar cell applications. In this doctoral thesis, we first investigate the effect of atomic hydrogen (H) supply on the photoresponsivity enhancement of undoped and boron (B)-doped $BaSi_2$ films. Then, we explore H states and position in undoped $BaSi_2$ using muon spin rotation.

In chapter 3, we demonstrate the effect of H passivation on both the photoresponsivity and minority-carrier lifetime of $BaSi_2$ epitaxial films. Atomic H is applied to $BaSi_2$ films at 580 ºC and change H supply duration in the range of 1−30 min, followed by capping with an amorphous Si layer. The photoresponsivity of the films changes considerably depending on H supply duration and reach a maximum of 2.5 A/W at a wavelength of 800 nm for the sample passivated for H supply duration of 15 min under a bias voltage of 0.3 V applied to the front-surface indium-tin-oxide electrode with respect to the back-surface aluminum electrode. This value is approximately one order of magnitude higher than the highest value previously reported. Microwave photoconductivity decay measurement reveals that the minority-carrier lifetime of the $BaSi_2$ film with the highest photoresponsivity is 14 μs. We also calculate the total density of states of $BaSi_2$ by *Ab initio* studies when one Si vacancy exists in a unit cell, and one, two, and three H atoms occupy Si vacancy or interstitial sites. In certain cases, H passivation of the Si dangling bonds can markedly decrease trap concentration. From both experimental and theoretical viewpoints, we conclude that an atomic H supply is beneficial for $BaSi_2$ solar cells.

In chapter 4, we investigate the H effect on the photoresponsivity of 500-nm-thick B-doped p-$BaSi_2$ films. The photoresponsivity reaches ~4 A/W of H passivated lightly B-doped $BaSi_2$, which is about twice the highest value reported for H passivated undoped $BaSi_2$ films, because of an increased minority-carrier lifetime, as measured by the microwave-detected photoconductivity decay. Furthermore, *Ab initio* studies are used to

interpret and understand experimental observations by analyzing states in the gap region, which can act as traps, in B-doped p-$BaSi_2$ with H incorporation. Moreover, the effect that atomic H had on the performance of B-doped p-$BaSi_2$/n-Si heterojunction solar cells is also studied. The saturation current density is found to decrease by three orders of magnitude with the atomic hydrogen supply, and the η is increased up to 6.2%. Deep-level transient spectroscopy revealed a reduction of defect densities induced by the atomic hydrogen.

Chapter 5, we explore H states and position by an advanced technique, which is muon spin rotation. An implanted muon beam binds electrons to form muonium. Their response to thermal activation shows that muonium accompanies a shallow energy level of approximately 31 meV below the conduction band minimum, indicating that atomic H also serves an electronically active donor impurity in $BaSi_2$. This result is in good agreement with *Ab initio* studies showing that a localized half-filled peak appears approximately 40 meV below the conduction band minimum if the first neighbors of the H atom are one Si atom and one Ba atom.

Table of contents

Chapter 1 Introduction *1*

1.1 Energy consumption and global warming 1

1.2 Photovoltaics 2

1.3 Solar cell materials 4

1.4 Reference 9

Chapter 2 Introduction of $BaSi_2$. *11*

2.1 General information of $BaSi_2$ 11

2.2 Fabrication methods of $BaSi_2$ 12

2.3 Optical and electric properties of $BaSi_2$ 15

2.4 Dopants 18

2.5 p-$BaSi_2$/n-Si heterojunction solar cell 18

2.6 n^+-$BaSi_2$/p-$BaSi_2$/p^+-$BaSi_2$ homojunction solar cell 18

2.7 Aim of this work 20

2.8 Reference 23

Chapter 3 H passivated a-Si layer and undoped $BaSi_2$ *25*

3.1 Introduction 25

3.2 Experiment 26

3.3 Results and discussion 28

3.4 Summary 39

3.5 Reference 40

Chapter 4 H passivated p-$BaSi_2$, n-$BaSi_2$, and p-$BaSi_2$/n-Si heterojunction solar cells *41*

4.1 H passivation p-$BaSi_2$ 41

4.1.1 Introduction 41

4.1.2 Experiment 41

4.1.3 Results and discussions 43

4.1.4 Summary 54

4.2 H passivated n-$BaSi_2$ 55

4.2.1 Experiment 55

4.2.2 Results and discussions 56

4.2.3 Summary 58

4.3 Reference 59

Chapter 5 Detecting H states in $BaSi_2$ by muon spin rotation *61*

5.1 Introduction of muon spin rotation 61

5.2 Experiment 65

5.3 Results and discussions 66

5.4 Summary 69

5.5 Reference 70

Chapter 6 Conclusion and prospects *71*

Acknowledge *73*

Award *75*

List of publications *77*

List of conference (International only) *79*

Chapter 1 Introduction

1.1 Energy consumption and global warming

World energy consumption is the total energy production and spending by the entire human civilization. It involves all energy harnessed from every source and is applied towards humanity's behaviors across every single industrial and technological sector, across every country. Figure 1.1(a) shows energy consumption of some primary countries from 2008 to 2018[1]. The US, Japan, and Germany are developed countries and have already finished industrialization. Thus, the energy consumption is kept at almost a constant value meaning no more excess energy for them to develop. On the other hand, China, the world's largest developing country, consumes energy most and increases every year. By the end of 2018, the energy consumption is approximately 1.5 times larger than the US. Among all kinds of energies, electricity is the most important for daily life because it can be used in many aspects such as, heating and lighting. Therefore, human society cannot work without electricity. Figure 1.1(b) shows the electricity generation of primary countries from 2008 to 2018. The tendency is the same as that in Fig. 1.1(a). China' s electricity generation is increased over twice for the past ten years indicating that electricity is an imperative energy source and a key factor to economic development.

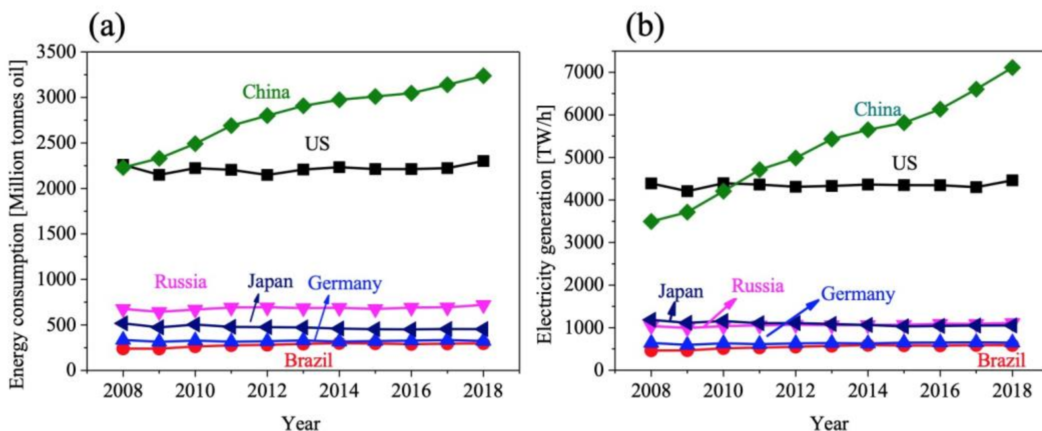

Fig. 1. 1. (a) World's energy consumption (2018 data) [1]. (b) The world electricity generation by year of 2018 [1].

Figure 1.2 shows how the world electricity was generated in 2018[2]. Coal, gas, and oil are used to create two-thirds of electricity in 2018. Burning them emits greenhouse gases, including carbon dioxide (CO_2), sulfur dioxide (SO_2), and methane, affecting the climate markedly. This phenomenon is well-known as the greenhouse effect or Nino phenomenon [3]. Temperature rising is promoted again by the self-reinforcing climate feedback, such as loss of snow cover, increasing water vapor, and melting permafrost. The earth's temperature will not be suitable for human living if we do not control the temperature rising. Figure 1.3(a) is the CO_2 concentration over the last 800,000 years measured from ice cores. It is increased tremendously after the industrial revolution, since, energy started

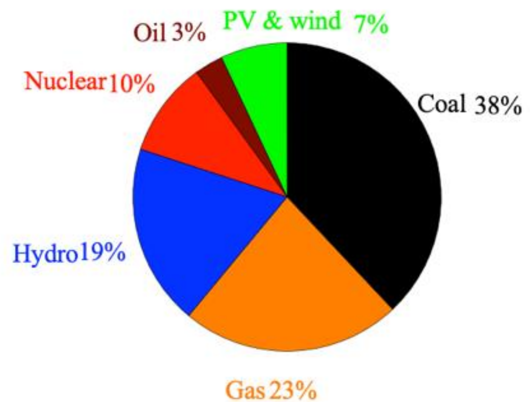

Fig. 1.2. The world electricity generation by sources in 2018 [2].

to be obtained by burning a large amount of coal, gas, and oil. Figure 1.3(b) shows the sea level height within 25 years. It is clear to state that the sea level rises as a function of year, meaning that temperature rising causes ice melting to water and rises the sea level. The sea will submerge cities that are located at seaside. However, these cities are almost developed because sea transport is convenient and brings prosperous economy. To reduce CO_2 emission, we must discover new energy supply methods with a low cost. Thus, renewable energy sources are now in the center of investigation, including wind, bioenergy, geothermal, and photovoltaics.

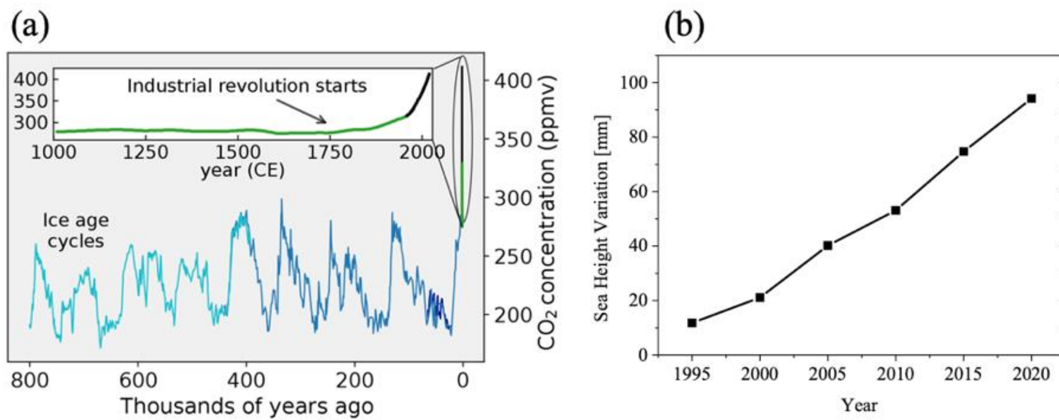

Fig. 1.3. (a) The CO_2 concentration in atmosphere during the last 800 thousand years. It increases tremendously after the industrial revolution [3]. (b) The sea level of past 15 years [4].

1.2 Photovoltaics

Photovoltaics is renewable energy and attracts more and more attention. It converts light into electricity using semiconducting materials. The first solar cell was created by Charles Fritts in 1883, achieved a power conversion efficiency (η) of 1−2% by covering selenium with a thin layer of gold. In 1954, physicists at Bell laboratories discovered that crystalline silicon (c-Si) is more efficient than selenium and fabricated the first practical solar cell with the η of 6% [5]. The first practical application of solar cells was orbiting satellites and spacecraft, but today, the majority of photovoltaic modules are used for grid-connected systems for power generation. The *p-n* or *p-i-n* photodiode is the most basic structure in solar cells. There are four important parameters to describe the solar cell performance, including short-circuit current (I_{SC}), open-circuit voltage (V_{OC}), fill factor (*FF*), and η. Figure 1.4 shows an example of a *p-n* diode, a doping profile, and an energy band diagram. Under the light illumination, in an ideal photodiode, I_{SC} equals the photocurrent (I_L), concluding the drift current (I_{dr}) due to photogenerated carriers within the depletion region and the diffusion current (I_{diff}) outside of the depletion region. The I_{dr} is given by Eq. 1.1, 1.2. *G* is

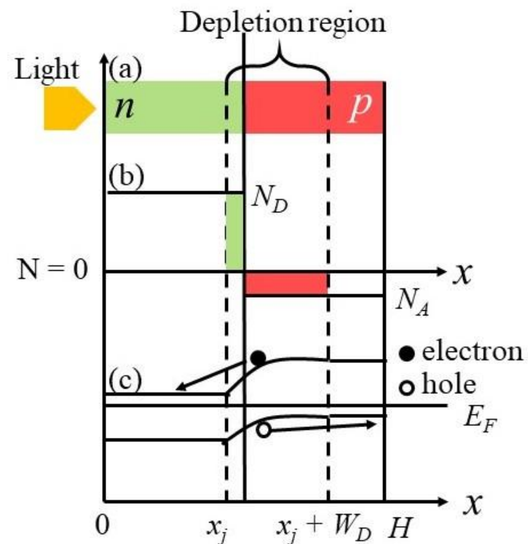

Fig. 1.4. (a) Solar cell dimensions under consideration. (b) Assumed abrupt doping profiles $N_D >> N_A$. (c) Energy band diagram showing moved minority carriers.

the carrier generation rate in the depletion region. R is the reflectance and α is the absorption coefficient. W_D is the depletion width. Φ_0 is the number of incident photons per area per time per unit wavelength.

$$I_{dr} = -q\int_0^{W_D} G(\lambda, x)dx = q\phi_0(1 - R)\exp(-\alpha x_j)[1 - \exp(-\alpha W_D)]. \quad (1.1)$$

$$G(\lambda, x) = \alpha(\lambda)\phi(\lambda)[1 - R(\lambda)]\exp[-\alpha(\lambda)x]. \quad (1.2)$$

The I_{diff} is derived from the diffusion equation and boundary conditions. The final results are shown in Eqs. 1.3 and 1.4 for holes in the n-type (I_p) and electrons in the p-type (I_n) semiconductor. Here, L_p and L_n are the hole and electron diffusion length. D_p and D_n are the hole and electron diffusion coefficient. S_p and S_n are the surface recombination velocity for hole and electron, respectively. These parameters depend on materials and are obtained from experiment.

$$I_p = \left[\frac{q\phi(1 - R)\alpha L_p}{\alpha^2 L_p^2 - 1}\right] \times \left[\frac{\left(\frac{S_p L_p}{D_p} + \alpha L_p - \exp(-\alpha x_j)\left(\frac{S_p L_p}{D_p}\cosh\frac{x_j}{L_p} + \sinh\frac{x_j}{L_p}\right)\right)}{\frac{S_p L_p}{D_p} sin\frac{x_j}{L_p} + \cosh\frac{x_j}{L_p}} - \alpha L_p \exp(-\alpha x_j)\right]. \quad (1.3)$$

$$I_n = \left[\frac{q\phi(1 - R)\alpha L_n}{\alpha^2 L_n^2 - 1}\right] \times \exp[-\alpha x_j + W_D] \times \left\{\alpha L_n - \frac{\frac{S_p L_p}{D_p}\left[\cosh\left(\frac{H'}{L_n}\right) - \exp(-\alpha H') + \sinh\left(\frac{H'}{L_n}\right) + \alpha L_n \exp(-\alpha H')\right]}{\frac{S_n L_n}{D_n} sinh\frac{H'}{L_n} + \cosh\frac{H'}{L_n}}\right\}. \quad (1.4)$$

$$I_{SC} = I_L = I_{diff} + I_{dr} = I_p + I_n + I_{dr}. \quad (1.5)$$

The I_L is the sum of I_{diff}, I_p, and I_n as shown in Eq. 1.5. The current-voltage (I-V) characteristics of the solar cell under illumination is simply a summation of the dark current of the p-n junction and the I_L, which is given by Eq. 1.6. Here, I_S is the saturation current density. We will obtain the V_{OC} by setting $I = 0$ as shown in Eq. 1.7.

$$I = I_L - I_S\left[\exp\left(\frac{qV}{kT} - 1\right)\right]. \quad (1.6)$$

$$I = 0, V_{OC} = \frac{kT}{q}\ln\left(\frac{I_L}{I_s} + 1\right). \quad (1.7)$$

$$FF = \frac{I_m V_m}{I_{SC} V_{OC}}. \quad (1.8)$$

$$\eta = \frac{I_{mp} V_{mp}}{P_{in}} = FF \times \frac{I_{SC} V_{OC}}{P_{in}}. \quad (1.9)$$

Figure 1.5(a) shows the I-V curve of a solar cell under dark and illumination. V_{OC}, I_{SC}, V_{mp}, and I_{mp} are shown. V_{mp} and I_{mp} correspond to the current and voltage for the maximum power output (P_m). The FF is determined by Eq. 1.8, which represents the sharpness of the I-V curve. The maximum FF value is 1 in an ideal case; however, in practice, a general FF value is around 0.8. The η of Eq. 1.9 is the ratio of the maximum power output (P_m) to the incident power (P_{in}) and determined by FF, I_{SC}, V_{OC}, and P_{in}. Therefore, the improvement in FF, I_{SC}, and V_{OC} is the main work in the solar cell investigation. The I_{SC} is increased by a small band gap (E_g) because more electron-hole pairs can be generated, while the V_{OC} is decreased. Consequently, there is an optimum value for E_g to reach the highest η. Figure 1.5(b) shows the Shockley-Queisser (S-Q) limit [6]. The maximum η at E_g = 1.3 eV is approximately 30%. According to Eq. 1.7, V_{OC} is proportional to I_L; thus,

promoting I_L by reducing defects is one of methods to enlarge V_{OC}. Many factors should be considered to affect FF, such as the series resistance (R_S) from ohmic loss in the front surface, the shunt resistance (R_{SH}) from leakage currents, and defects in the depletion region.

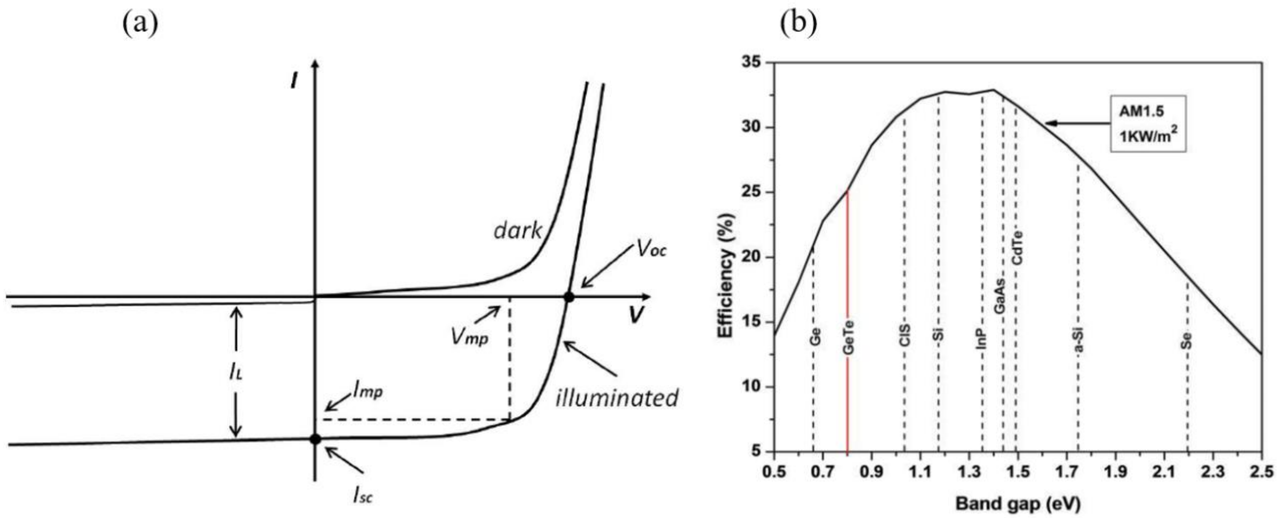

Figure 1.5. (a) The I-V curve of an ideal solar cell. (b) The Shockley-Queisser limit, the theoretical η of various semiconductors with different E_g [6].

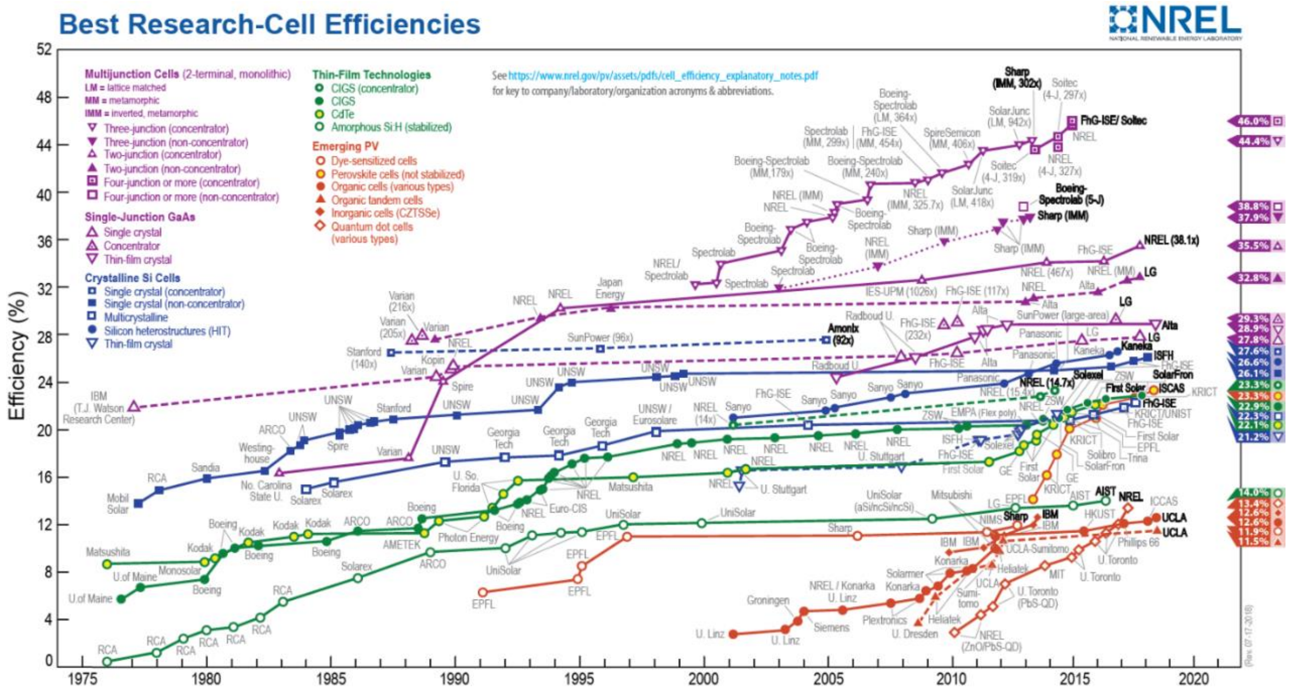

Fig. 1.6. Recent best research-cell efficiencies in the world [7].

1.3 Solar cell materials

Since the first practical solar cell, many semiconducting materials have been found to be suitable for solar cells, such as Si, gallium arsenide (GaAs), copper indium gallium selenide (CIGS), and perovskite. Figure 1.6 shows the best research-cell η's in the world by the year 2020, summarized by National Renewable Energy Laboratory (NREL) [7]. The highest η of single-junction Si and GaAs solar cells are 27.6% and 28.9%,

respectively. According to the S-Q limit, the η approaches their theoretical limit. The thin-film CIGS solar cell achieved the η of 23.3%. The η of the emerging perovskite solar cell increases dramatically from 3.8% to 23.3% within a few years and indicates that it has a great potential to be applied in the next generation. The above four solar cells will be fruitfully discussed in the following parts.

a. Si solar cells

Crystal Si (c-Si) including mono-Si, poly-Si, and amorphous Si (a-Si) are the first practical solar cell materials. The mono-Si with an indirect E_g of 1.12 eV and an α of 10^3 cm^{-1} at 1.5 eV is often fabricated by the Czochralski process, which has a higher η, comparing to poly-Si and a-Si solar cells [8]. At present, the highest η^{real} of Si heterojunction solar cell with the interdigitated back contacts (HJ-IBC) is over 26% by Kaneka Corporation, Japan [9]. Both electrical and optical properties are improved to achieve the world record. Figure 1.7(a) shows the structure of this solar cell. The mono-Si works as an absorber layer, top and bottom surfaces are passivated by a-Si, and the anti-reflection layer (AR) is deposited on the top surface to reduce optical losses. The measured V_{OC}, I_{SC}, and FF is 0.744 V, 42.3 mA/cm^2, 0.838, respectively. Comparing to the higher theoretical η of 29.1%, researchers believe that the short minority carrier lifetime degrades the performance of the solar cell due to the recombination at defects as well as the optical losses at the rear side and the large series resistance. The homojunction and heterojunction mono-Si solar cells with different types of contact have been also studied. Figures 1.7(b) and (c) show Si homojunction solar cells with the passivated emitter and rear cell (PERC) and the IBC. Figure 1.7(d) is the Si heterojunction with the intrinsic thin-layer a-Si solar cell (HIT). The intrinsic high-quality a-Si layers help to reduce defects at the surface of the absorber layer and lead to a low voltage loss [10-12]. The low cost is the most advantage of the poly-Si solar cells because they are made from the molten Si with post-cooling and solidified. However, the η of poly-Si solar cells is lower than that of mono-Si solar cells because they contain more crystal grains [9, 10]. The a-Si consists of short-range disordered Si atoms as well as Si dangling bonds. These dangling bonds have an unpaired electron and work as point defects. To saturate these Si dangling bonds, we usually apply hydrogen (H) passivation to a-Si. A H atom shares one electron to a dangling bond, and forms a stable Si-H bond. This is called hydrogenated a-Si (a-Si:H). The a-Si:H is a direct band semiconductor with an E_g of 1.7 eV. Because of large α, only a few micrometers a-Si is enough to work as the light absorption layer. The a-Si:H was first fabricated on a glass substrate by R. C. Chittick in 1969 using plasma-enhanced chemical vapor deposition (PECVD). A radio-frequency (RF) plasma generator was used to decompose SiH_4 gas [11]. Clarlson and Wronski fabricated the first a-Si:H solar cell with an η of 2.4% in 1976 at RCA laboratory [12]. The low η is primarily due to the high defect concentration of a-Si:H. It also suffers from the light-induced degradation, which is now believed due to Si-H bonds [13]. Now, the highest η of a-Si:H solar cell with the *p-i-n* structure is 10.22%, which is achieved by National Institute of Advanced Industrial Science and Technology (AIST), Japan [14]. This solar cell contains a small amount of metastable defect obtained at a deposition rate of $1 - 3 \times 10^{-2}$ nm/s by triode PEVCD. Researchers also investigate the impact of the deposition rate of the a-Si:H absorber layer on the solar cell performance and its metastability. The deposition rate is varied over the wide range by using diode and triode PECVD processes. The results show that the light-induced degradation does not appear even when a-Si:H is deposited at a very low deposition rate.

b. GaAs solar cell

GaAs is a III-V semiconductor with a zinc blende crystal structure and applied in many fields. It is also a substrate for epitaxial growth of other III-V semiconductors, including indium gallium arsenide (InGaAs) and aluminum gallium arsenide (AlGaAs) [15]. It has a suitable E_g of 1.42 eV; thus, from the viewpoint of the S-Q limit, the η should be larger than the mono-Si solar cells. GaAs is a direct band gap semiconductor with a large α of 2.2×10^7 cm^{-1} at 4.8 eV, only 2 μm-thick GaAs is sufficient to absorb light for the solar cell application. The mobility of electron and hole is 8500 cm^{2}V^{-1}s^{-1} and 400 cm^{2}V^{-1}s^{-1}, respectively. Owing to these

advantages, GaAs is an excellent material for the thin-film solar cells and has already imposed to spacecraft. The first well-known operational usage of GaAs solar cell in spacecraft was Venera 3 mission, launched in 1965. Recently, the triple-junction solar cells based on GaAs with Ge and InGaAs layers are developed, holding a record η of over 32%, it can operate with the light as concentrated as 2000 suns [16]. This solar cell powers Mars exploration rovers Spirit and Opportunity to explore Mar's surface. In 2016, researchers from Korea fabricated a high η GaAs thin-film solar cell on a flexible substrate using a simple and fast epitaxial lift-off (ELO) method that utilizes the stress of a sputtered Cr/Au bilayer [17]. The structure is shown in Fig. 1.8. The η, V_{OC}, I_{SC}, and FF are 22.08%, 0.98 V, 27.06 mA/cm^2, and 0.8335, respectively. It has a wide application comparing to the traditional GaAs single-junction solar cells because of the flexible substate. However, GaAs solar cells has some shortcomings. The most serious problem of GaAs is the use of toxic element As and thus very expensive. Careful attention should be paid when fabrication and encapsulation. The recycling of commercial GaAs solar cells is also required a professional technique.

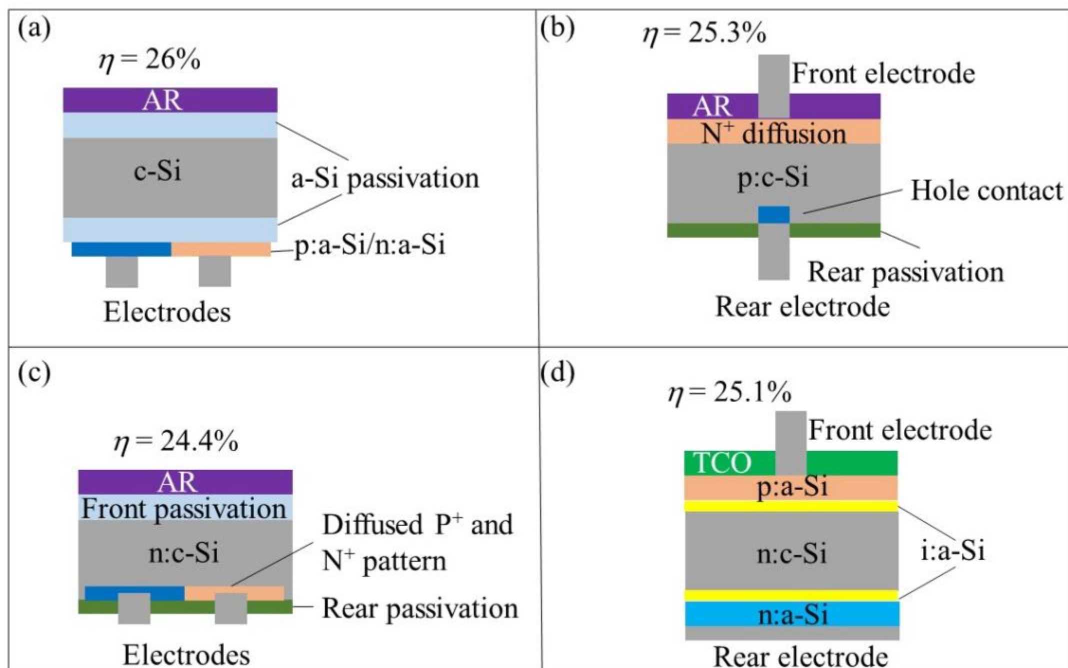

Fig. 1.7. (a) Cross-section schematic image of the HJ-IBC cell. (b) A top rear contacted homojunction solar cell. (c) A homojunction IBS solar cell that has interdigitated P$^+$ and N$^+$ diffused region in the Si substrate directly contacted by hole and electron contacts respectively. (d) HIT solar cell.

Fig. 1.8 Cross-section of single junction GaAs thin film solar cell on a flexible substrate.

c. CIGS solar cell

CIGS is a I-III-VI compound semiconductor material composed of copper, indium, gallium, and selenium with the chalcopyrite crystal structure. The chemical formula is $CuIn_xGa_{(1-x)}Se_2$, where the value of x is varied from 1 ($CuInSe_2$) to 0 ($CuGaSe_2$). The E_g can be changed continuously with x from about 1.0 eV to about 1.7 eV. Thus, the proper E_g for different layers will be achieved by setting the proper x. As CIGS is a direct band gap semiconductor, the α is more than 10^5 cm^{-1} at 1.5 eV or higher photon energies. Therefore, thin-film CIGS solar cell is one of the three mainstream thin-film photovoltaic technologies associated with cadmium telluride (CdTe) and a-Si:H [18, 19]. The fabrication methods of CIGS thin films are vacuum evaporation and sputtering, where Cu, Ga, and In are co-deposited on a substrate at room temperature (RT), then, post-annealing is performed in a Se vapor. Or, four elements of Cu, Ga, In, and Se are co-deposited on a hot substrate. The typical structure of CIGS solar cells is shown in Fig. 1.9. A 1−3 mm thick soda-lime glass is always used as a substrate to increase V_{OC} by passivation of surface and grain boundary defects [20]. The molybdenum (Mo) metal layer is deposited by sputtering, serves as back contact, and reflects unabsorbed light to the CIGS layer. Following the Mo layer, a *p*-type CIGS absorber layer is formed, and a thin *n*-type buffer layer is added on top of the absorber. It is typically a cadmium sulfide (CdS) layer by chemical bath deposition. After that, an intrinsic zinc oxide layer (i-ZnO) is capped with a thicker aluminum (Al)-doped ZnO layer. The i-ZnO layer works as a window layer to prevent the sputtering damage of the Al-doped ZnO layer. The Al-doped ZnO layer works as a transparent conducting oxide to collect electrons. Solar Frontier Corporation has set a new world record of CIGS thin-film solar cell with the η of 23.35% on a 1 cm^2 cell using Cd-free CIS technology. This result is independently verified by AIST in November 2018 and presented at 46th IEEE PVSC at Chicago, June 19th, 2019 [21]. CIGS can also be applied in a tandem solar cell due to its tunable band gap, acting as a top cell in CIGS/c-Si tandem solar cell or bottom cell in perovskite/CIGS tandem solar cell [22]. However, CIGS solar cell has a disadvantage. The In element is a rare element, and it is difficult to apply for global deployment.

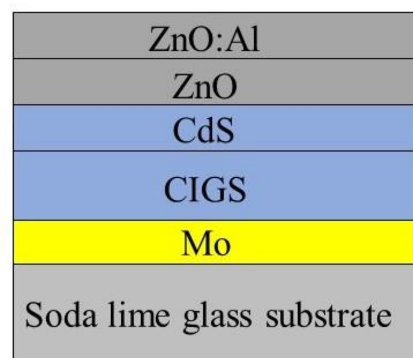

Fig. 1.9 The structure of CIGS solar cell

d. Perovskite solar cells

Perovskite solar cells are the third-generation solar cells and developed at high speed. It is a type of solar cell including a perovskite structure compound, most commonly a hybrid organic-inorganic lead or tin halide-based material, as a light-harvesting active layer [23]. The usual perovskite absorber is methylammonium lead trihalide ($CH_3NH_3PbX_3$). The structure is shown in Fig. 1.10(a). X, including the halogen ion such as iodide (I), bromide (Br), or chloride (Cl), decides the optical E_g between 1.55 and 2.3 eV. The organic ions of CH_3NH_3 and Pb can be changed to Cs and Sn, respectively, and called dye-sensitized solar cell. One of dye-sensitized solar cells where $CsSnI_3$ works as a p-type hole transport layer and absorber are promising low-cost alternatives to the conventional solid-state photovoltaic devices based on materials such as Si and CIGS. However, they suffer from durability problems that result from their use of organic liquid electrolytes containing the I redox couple. The first dye-sensitized solar cell uses the p-type direct band gap semiconductor $CsSnI_3$ for hole conduction instead of a liquid electrolyte. The resulting solid-state dye-sensitized solar cells consist of $CsSnI_{2.95}F_{0.05}$ doped with SnF_2, nanoporous TiO_2, dye N719, and show η of up to 10.2% [24]. Figure 1.10(b) shows the energy level of this solar cell. The photogenerated electron and hole can be separated and arrive at the electrodes without blocking. To fabricate perovskite solar cells, we apply one-step solution, two-step solution, and vapor deposition methods. In the one-step solution processing, the mixed solution of lead halide and organic halide is directly deposited through various coating methods such as spin coating, spraying, blade

coating, and slot-die coating. It is a simple, fast, and inexpensive method but with poor crystal quality involving voids, platelets, and other defects [25]. The two-step solution deposition is discovered in 2015 to avoid voids in the one-step method [26]. First, the lead halide film is deposited on a substrate. Second, the organic halide film is deposited and reacts with the lead halide film. The volume of films is expanded to fill voids during the reaction. Thus, crystal quality becomes better than the one-step deposition. In the vapor deposition, the organic halide vapor is deposited on the lead halide thin film and converted into the perovskite films [27]. This method has a great benefit in the fabrication of multi-stacked thin-film solar cells in a large area. In 2017, during PVSEC-27 (Lake Biwa, Japan), the British research group announced that perovskite could be formed on the silicon substrate. Since then, this new structure attracted more and more attention. In 2018, the fully textured monolithic perovskite/silicon tandem solar cells achieved an η of 25.2% in Switzerland [28]. Figure 1.11 shows the cross-section of this solar cell. The pyramidal texture is used to reflect unabsorbed light to increase I_{SC}. Despite the excellent performance of perovskite solar cells, it degrades within a few hours to days under standard operating conditions and are quite sensitive to humidity because the perovskite salts are partially soluble in water. At the same time, Pb is a toxic element. Encapsulation and recycling are important for this solar cell. The future research of perovskite solar cells will be focused on durability and non-toxic perovskite.

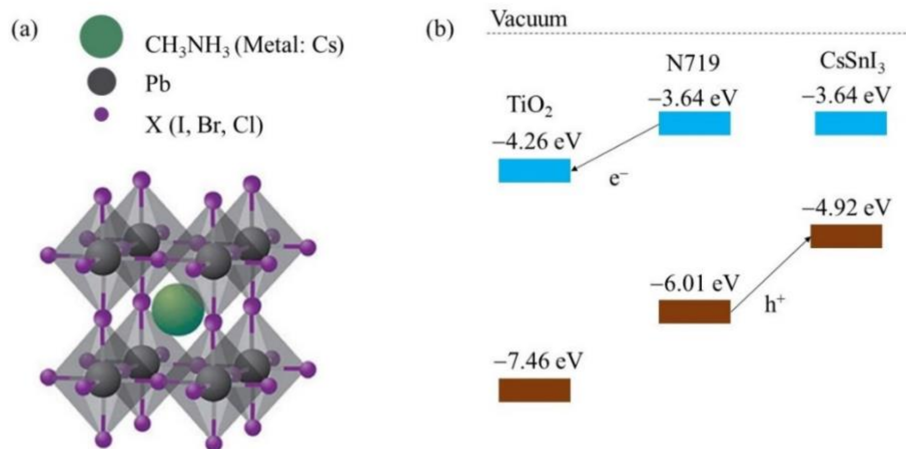

Fig. 1.10 (a) Crystal structure of Perovskite material. (b) Energy level of the first perovskite solar cell [xxx].

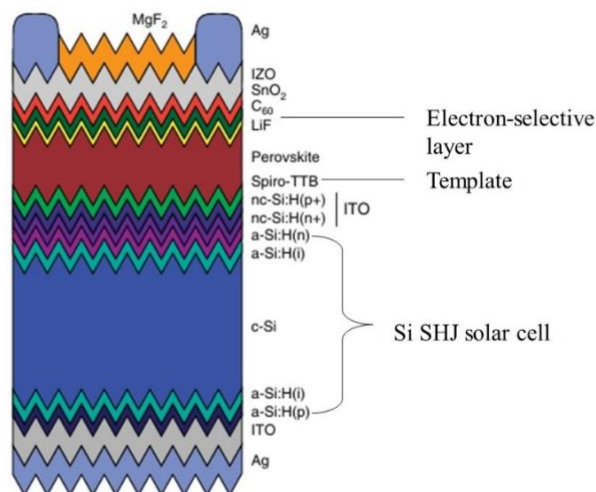

Fig. 1.11 Cross-section of the Si and perovskite tandem solar cell [xxx].

1.4 Reference

1. BP Statistical Review of World Energy 68th edition (2019).
2. World gross electricity production, by source (2018).
3. J. G. J. Olivier and J. A. H. W. Peters, Trends in Global CO_2 and Total Greenhouse Gas Emissions (PBL Netherlands Environmental Assessment Agency, 2019).
4. R. Lindsey, Climate Change: Global Sea Level, (2020) online: https://www.climate.gov/news-features/understanding-climate/climate-change-global-sea-level
5. APS News, American Physical Society **18**, 4 (2009).
6. W. Shockley and H. J. Queisser, J. Appl. Phys. **32**, 510 (1961).
7. M. A. Green *et al.,* Prog. Photovolt: Res. Appl. **28**, 7 (2020).
8. M. A. Green and M. J. Keevers, Prog. Photovolt: Res. Appl. **3**, 189 (1995).
9. K. Yoshikawa *et al.,* Nat. Energy **2**, 17032 (2017).
10. M. A. Green, Sol. Energy Mater. Sol. Cells **143**, 190 (2015).
11. R. C. Chittick, J. Electrochem. Soc. **116**, 77 (1969).
12. D. E. Carlson and C. R. Wronski, Appl. Phys. Lett. **28**, 671 (1976).
13. E. Bhattacharya and A. H. Mahan, Appl. Phys. Lett. **52**, 1587 (1988).
14. T. Matsui *et al.,* Appl. Phys. Lett. **106**, 053901 (2015).
15. J. O. Akinlami and A. O. Ashamu, Chin. J. Semiconductors **34**, 3 (2013).
16. H. L. Cotal et al., 28th IEEE Photovoltaic Specialists Conference, Anchorage, September, 955 (2000).
17. S. Moon *et al.,* Sci. Rep. **6**, 30107 (2016).
18. P. D. Paulson *et al.,* J. Appl. Phys. **94**, 879 (2003).
19. T. Tinoco *et al.,* Phys. Stat. Sol. A **124**, 427 (1991).
20. L. Kronik *et al.,* Adv. Mater. **10**, 1 (1998).
21. M. Nakamura *et al.,* 46th IEEE PVSC, Chicago, IL, June 19, 2019. (also see https://www.solar-frontier.com/eng/news/2019/0117_press.html).
22. T. Todorov *et al.,* Adv. Energy Mater. **5**, 1500799 (2015).
23. J. S. Manser *et al.,* Chem. Rev. **116**, 12956 (2016).
24. I. Chung *et al.,* Nature **485**, 11067 (2012).
25. N. J. Jeon *et al.,* Nat. Mater. **13**, 4014 (2014).
26. H. Zhang *et al.,* Adv. Energy Mater. **5**, 1501354 (2015).
27. Q. Chen *et al.,* J. Am. Chem. Soc. **136**, 622 (2014).
28. F. Sahli *et al.,* Nat. Mater. **17**, 820 (2018).

Chapter 2 Introduction of $BaSi_2$.

2.1 General information of $BaSi_2$

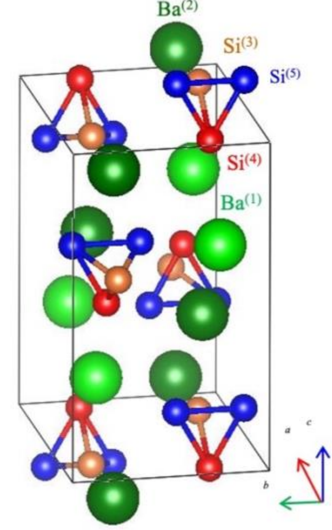

Fig. 2.1. Crystal structure of $BaSi_2$.

Recently, thin-film solar cells have attracted more and more attention thanks to their excellent properties, but the thin-film solar cells such as CIGS or GaAs have rare and/or toxic elements or lead to a high cost and poor long-term stability. Semiconducting barium disilicide ($BaSi_2$) has many advantages for solar cell application. For example, it has a suitable band gap (E_g) of 1.3 eV, a large absorption coefficient (α) of 3×10^4 cm^{-1} at 1.5 eV, an excellent minority carrier lifetime (τ) of 10 μs. It also consists of safe, stable, and earth-abundant elements of Ba and Si. The theoretical conversion efficiency (η) is approximately 25%. Thus, the investigation of $BaSi_2$ is mandatory [1].

$BaSi_2$ has an orthorhombic crystal structure at RT and atmospheric pressure. However, the phase transition occurs at high temperature and pressure [2]. Figure 2.1 shows the unit cell of $BaSi_2$. The lattice constant of *a*, *b*, and *c* is 0.891, 0.672, and 1.153 nm, respectively. There are two crystallographically inequivalent sites for Ba ($Ba^{(1)}$ and $Ba^{(2)}$) and three inequivalent sites for Si ($Si^{(3)}$, $Si^{(4)}$, and $Si^{(5)}$). One unit cell consists of 8 Ba atoms and 16 Si atoms; thus, the stoichiometric description is Ba_8Si_{16}. A unique structure called the Si tetrahedra contains four Si atoms. Four Si atoms connect with each other by sp^3 hybridized orbital to form a Si tetrahedral and leave four dangling bonds of sp^3 orbital to be filled with four electrons donated by two Ba atoms. Therefore, there are strong covalent bonds between the Si atoms via sp^3 hybridized orbitals in addition to the weak ionic bonding between Ba and Si tetrahedral. First-principles calculation by VASP code based on a hybrid nonlocal density-functional theory (DFT) is used to calculate the band structure and the density of state (DOS) of $BaSi_2$ after the structure relaxation [3-7]. Figure 2.2(a) shows the DOS of $BaSi_2$. The Si *p* state appears in the valence band maximum (VBM), while the conduction band minimum (CBM) mainly consists of the Ba *d* state. The E_g is approximately 1.3 eV. Figure 2.2(b) shows the band structure of $BaSi_2$. The CBM is located at *T*(0,1/2,1/2), and the VBM is located at approximately (0,1/3,0) along the Γ−Y (0,1/2,0) direction. Thus, $BaSi_2$ is an indirect band gap semiconductor. However, the second-lowest conduction band is located at (0,1/3,0), which is at the same position as the VBM and only 0.1 eV higher than the CBM. Therefore, a direct transition may occur at approximately (0,1/3,0). Although $BaSi_2$ is an indirect band gap semiconductor, it possesses some properties of a direct band gap semiconductor likes a large α.

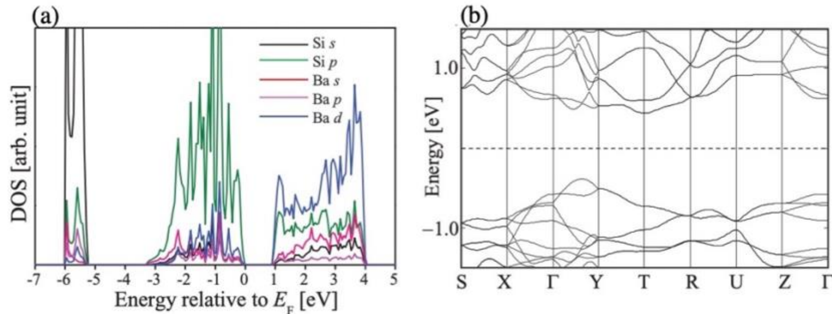

Fig. 2.2. (a)Partial DOS and (b) band structure of $BaSi_2$ [xxx].

2.2 Fabrication methods of $BaSi_2$

The first epitaxial $BaSi_2$ was formed on Si(111) and (001) substrates by Mckee *et al.* in 1993 [8]. Now, three methods have been investigated to form $BaSi_2$ thin films on Si substrates, namely, molecular beam epitaxy (MBE), sputtering, and vacuum evaporation. Substrates are not only Si, but also some materials such as germanium (Ge), glass, and titanium nitride (TiN) [9-11]. However, $BaSi_2$ thin films show the island structure on the Ge substrate, meaning that a large lattice mismatch exists at the heterointerface. Glass and TiN substrates are now under investigation.

The MBE growth procedure for undoped-$BaSi_2$ is shown in Fig. 2.3. First, a clean Si substrate is loaded to the ultra-vacuum chamber and heated at 900°C for 30 min for thermal cleaning. The Si substrate is observed by the reflection high-energy electron diffraction (RHEED) of a 7 × 7 Si surface reconstruction after thermal cleaning. Second, reactive deposition epitaxy (RDE) is applied, where only Ba atoms from the heating Ba source are deposited on the hot Si substrate. Usually, the substrate temperature (T_S) is kept at 500°C. An approximately 5-nm thick $BaSi_2$ template is formed by RDE. This template works as a seed to control $BaSi_2$ crystal quality and orientation in the following growth. Third is the MBE growth, Si atoms from the electron beam (EB) gun, Ba and dopants from heated sources are co-deposited on the Si substrate at T_S = 500–650°C. Generally, the steaky RHEED patterns are observed after RDE and MBE, indicating that the surface of $BaSi_2$ epitaxy layer is smooth. Finally, a 3-nm thick a-Si passivation layer is deposited on the $BaSi_2$ layer at T_S = 180°C to prevent oxidation. Figure 2.4(a) shows the RHEED patterns after RDE and MBE along Si[1−10] where steaky lines indicate the smooth surface of the $BaSi_2$ layer. θ–2θ x-ray diffraction pattern (XRD) with a Cu Kα radiation source is shown in Fig. 2.4(b). There are five peaks implying $BaSi_2$ 200, 400, and 600 reflections and the Si(111) substrate. Thus, the *a*-axis-oriented $BaSi_2$ is formed on the Si substrate. Figure 2.4(c) shows the epitaxial relationship of $BaSi_2$ on Si(111) and (001) substrates. It has a three-fold symmetric domain rotating by 120° around the normal on Si(111), while a twice symmetric domain rotating by 90° on Si(001). These domains are formed randomly on Si substrates. Thus, the MBE-grown $BaSi_2$ is not a single crystal but is a multi-domain epitaxial layer. These results are confirmed by electron backscatter diffraction maps shown in Fig. 2.4(d). Many grain boundaries exist in $BaSi_2$ thin films both on Si(111) and (001) substrates [12].

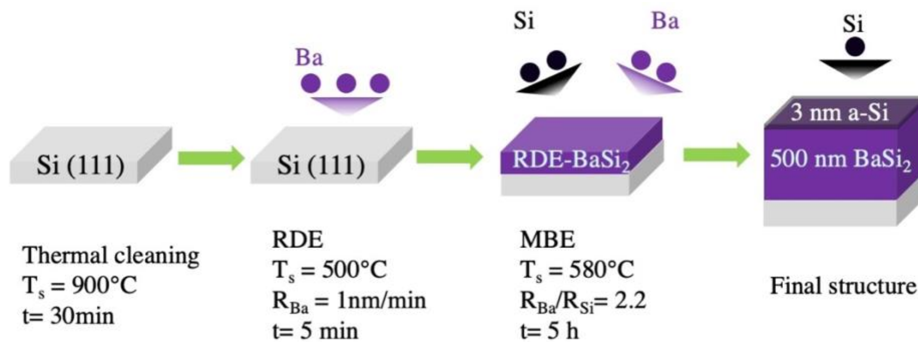

Fig. 2.3. MBE growth of $BaSi_2$ thin film on Si substrate.

The MBE method is a very powerful technique to conduct fundamental experiments and studies of $BaSi_2$, where the expensive and sophisticated instruments are used to generate ultrahigh vacuum and precise deposition rates of Si, Ba, and dopant elements. The growth rate of MBE growth is lower than the other growth methods to achieve high crystal quality. Usually, it takes 5 hours to deposit a 500-nm thick $BaSi_2$ by the MBE method. For the large-area fabrication, the sputtering method is one of the alternative growth methods. Comparing to the MBE method, it only takes 1–2 hours (based on the power and pressure) to deposit the same thickness of the MBE-grown $BaSi_2$. Latiff *et al.*, started the formation of $BaSi_2$ by sputtering in 2013 and

Matsuno, and Nemoto *et al*. established it [13-15]. Figure 2.5 is the sputtering processes. Helicon-wave excited plasma and radio-frequency (RF) plasma are used to sputter the $BaSi_2$ target, a 2-inch diameter polycrystalline fabricated by Tosoh Corporation. The deposition rate of Ba to Si is in excess of Si when only the $BaSi_2$ is sputtered, so extra three plate-like Ba sources are added to achieve the formation of $BaSi_2$ films. Figure 2.6(a) shows the XRD pattern of the sputtered $BaSi_2$, the appearance of $BaSi_2$ 201, 211, 301 reflections indicates that the sputtered $BaSi_2$ is a polycrystalline thin film. The diffraction peaks are much broader than the MBE growth implying poorer crystal quality. Figure 2.6(b) shows the Ba and Si atomic ratios of the sputtered $BaSi_2$. In spite of different values of RF power set on the $BaSi_2$ target (P_{BaSi2}), the atomic ratio is almost the same and closed to 2, demonstrating the stoichiometry can be achieved by the sputtering method. The photoresponsivity spectra are shown in Fig. 2.6(c) at a bias voltage of 0.1 V, which is very sensitive to the P_{BaSi2}, reaching a maximum value of approximately 0.67 AW^{-1} at a wavelength (λ) of 780 nm and P_{BaSi2} at 20 W [16]. These results give us strong evidence that $BaSi_2$ thin films can be formed by the sputtering method which has great potential to apply to solar cells at a low cost.

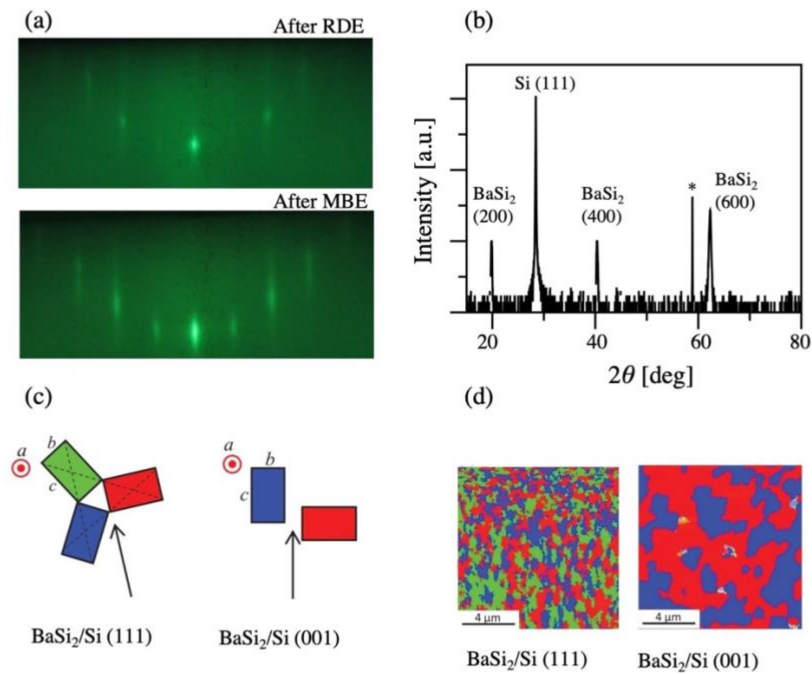

Fig. 2.4. (a) RHEED pattern. (b) θ-2θ XRD pattern. (c) Schematic of epitaxial variants for *a*-axis-oriented $BaSi_2$ films on Si(111) and Si(100). (d) EBSD crystal orientation map [12].

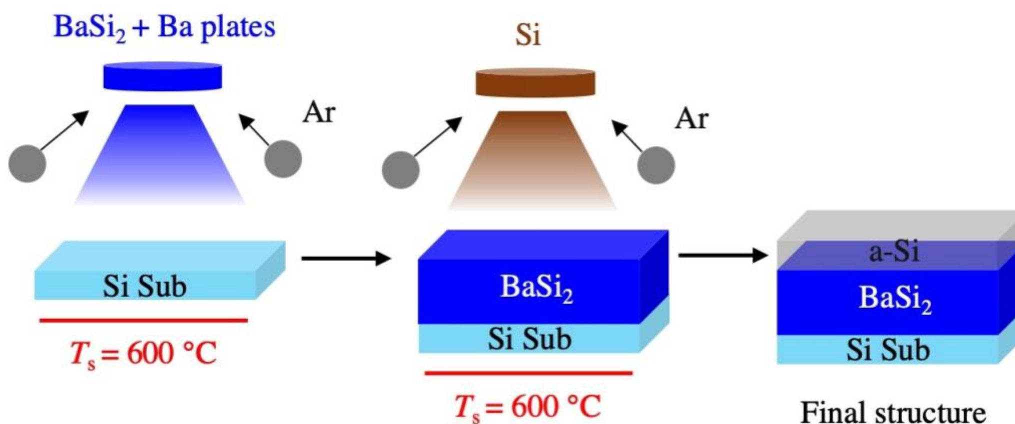

Fig. 2.5. Fabrication of sputtered $BaSi_2$.

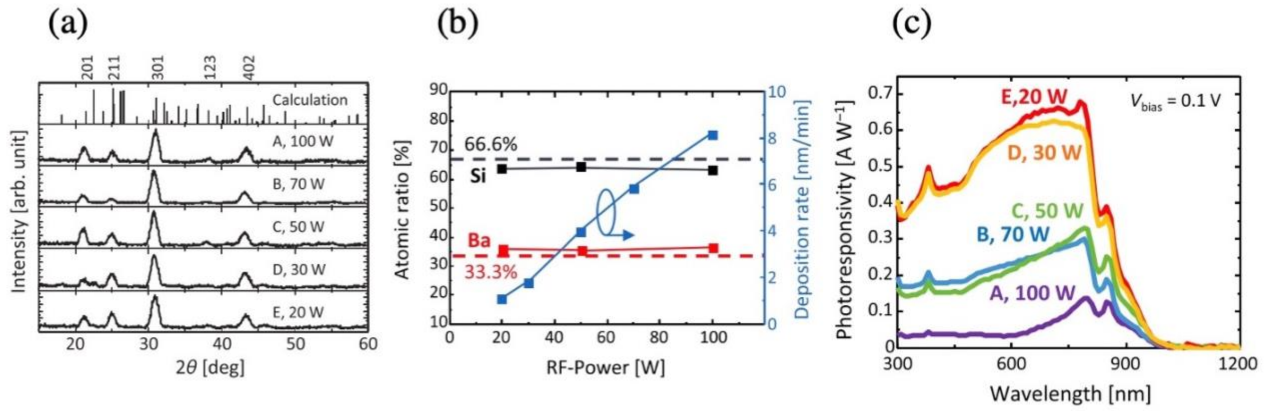

Fig. 2.6. (a) θ-2θ XRD pattern. (b) Ba and Si atomic rate vs RF power by RBS. (c) Photoresponsivity of sputtered $BaSi_2$ thin film under a bias voltage of 0.1 V [14,15].

Vacuum evaporation is another simple method to fabricate $BaSi_2$ thin films, and the growth rate is generally higher than the sputtering method. Figure 2.7 shows the deposition process of a $BaSi_2$ on a Si substrate by the vacuum evaporation of $BaSi_2$ granules. Ba and Si vapor come from heated $BaSi_2$ granules and are deposited on a Si substrate to form the thin-film $BaSi_2$. However, a serious problem exists, in which the vapor pressure of Ba and Si are vastly different. A much higher temperature is required to evaporate Si, usually, over 1000°C, while Ba evaporation takes place at much lower temperatures, only few hundreds °C. In addition, a chemical reaction between the source and holder materials may occur. This would lead to an inhomogeneous vaporization, and contaminated elements are emerged in $BaSi_2$ thin films. Figure 2.8(a) shows the XRD pattern of the vacuum evaporated $BaSi_2$. At substrate temperature over 400°C, the reflections of $BaSi_2$ 301, 211, 402, and 201 are markedly strong and well-matched with the theoretical pattern. This indicates that polycrystalline $BaSi_2$ thin films can be grown by vacuum evaporation. Figure 2.8(b) is the Raman spectra of the evaporated films. The films were deposited at 500 and 600°C. The peak near 475 cm^{-1} originates from the A_g mode of silicon tetrahedral meaning that the films contain the orthorhombic $BaSi_2$ [17].

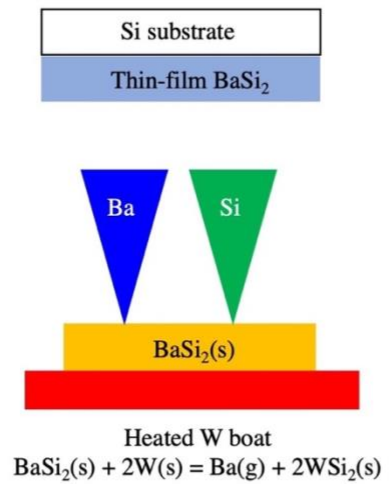

Fig. 2.7. Vacuum evaporation of $BaSi_2$

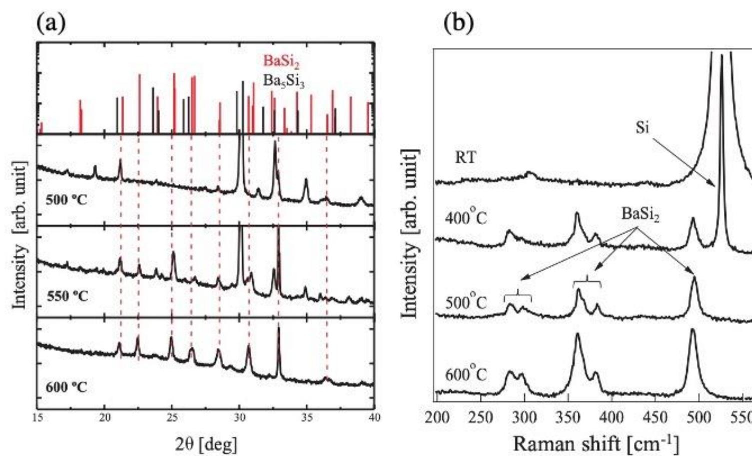

Fig. 2.8. (a) θ-2θXRD pattern of vacuum evaporated $BaSi_2$. (b) Raman spectra of vacuum evaporated $BaSi_2$ [17].

2.3 Optical and electric properties of $BaSi_2$

The α is measured by a 100-nm thick $BaSi_2$ on a 700-nm thick transparent silicon-on-insulator substrate, which ensures high transparent and high quality of $BaSi_2$ layer. The transmission spectra are obtained using a JASCO U-best 570 spectrophotometer at RT. Figure 2.9(a) shows the $BaSi_2$ absorption spectrum. The α is dependent on photon energy and increased from 10^2 cm^{-1} at photon energy of approximate 1.0 eV, reaching 3 × 10^4 cm^{-1} at 1.5 eV, which is 30-40 times larger than that of c-Si [18]. According to the calculation, 95% of photons with $E > 1.5$ eV can be absorbed within a 4-μm thick $BaSi_2$ layer. Figure 2.9(b) is the curve of the relation between $(adh\nu)^{1/2}$ and $h\nu$, for deriving the indirect E_g of 1.34 eV. The E_g can be enlarged when replacing some Ba atoms with Sr to form $Ba_xSr_{1-x}Si_2$. While isoelectric C atoms substitute some Si atoms and increase E_g from 1.3 to 3.0 eV [19, 20].

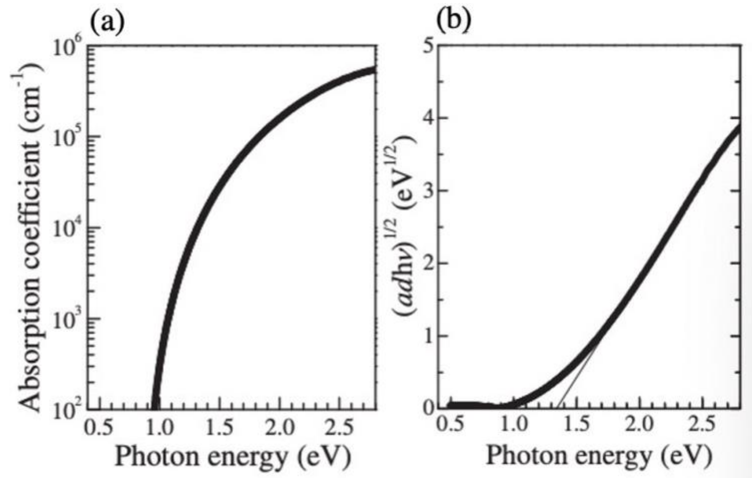

Fig. 2.9. (a) Absorption spectrum. (b) $(\alpha dh\nu)^{1/2}$ versus $h\nu$ plot for $BaSi_2$ epitaxial layers [18].

The properties of minority carrier such as τ and diffusion length (L) are very important because they affect the performance of a solar cell. Thus, it is worthwhile to investigate the τ and L. The τ is measured by the microwave photoconductance decay (μ-PCD) method using a 5-ns pulsed laser with a λ of 349 nm. According to the large α, the laser light is absorbed within 60 nm of the $BaSi_2$ layer. Figure 2.10(a) shows photoconductivity decay curves of the 130-nm-thick $BaSi_2$ film with laser intensities of 1.1 × 10^2 – 1.3 × 10^5 W/cm^2. The estimated areal photon density is 10^{12} – 10^{15} cm^{-2}. Assuming that photogenerated carriers are uniformly distributed over 130-nm thick $BaSi_2$ layer. Thus, the electron-hole pairs concentration is calculated to be 10^{17} – 10^{21} cm^{-3}, which is much larger than the majority carrier concentration in undoped $BaSi_2$. All curves can be divided into three decays. An initial rapid decay is from Auger recombination, because the electron-hole pairs are in a high concentration at the beginning of the measurement. After Auger recombination, an approximately constant decay is due to the Shockley-Read-Hall (SRH) recombination without the trapping effect. Final decay is due to the SRH recombination with carrier trapping effect. Instead of direct recombination, the minority carriers are trapped in localized states so the τ is lengthened. This phenomenon is also observed in crystalline Si [21-23]. The τ is expressed by Eq. 2.1, $\tau_{m,eff}$ is effective lifetime measured by μ-PCD, τ_b is the bulk minority carrier lifetime, and S_0 and S_W are the surface and interface recombination velocities. W is the thickness of sample. The relationship between $1/W$ and $\tau_{m,eff}$ is shown in Fig. 2.10(b), wherein the τ_b is known when $1/W$ equals 0. The τ_b is determined to be 14 μs, demonstrating that the minority carrier lifetime is sufficiently large to reach electrodes before recombination. In addition, the sum of the surface and interface recombination velocities is 8.3 cm/s, which is extremely low and confirms that $BaSi_2$ is a promising material

for solar cell applications [24, 25]. The *L* and grain size of a 300-nm thick $BaSi_2$ on a Si(111) substrate is evaluated by electron-beam-induced current (EBIC) technique and a bright-field (BF) plan-view transmission electron microscopy (TEM). Figure 2.10(c) shows the BF TEM image of $BaSi_2$ on Si(111) and (001). The grain sizes are approximately 0.1-0.3 μm, and 120º and 90º sharp grain boundaries in $BasSi_2$/Si(111) and $BaSi_2$/Si(001) respectively, are presented, tending to align along specific directions. Figure 2.11(a, b) and (c, d) show the secondary-electron and EBIC images of the Al contact with an acceleration voltage of 5 kV, wherein the minority carries penetration depth is shorter than the thickness of $BaSi_2$ layer. The EBIC line-scan data along dotted lines AA' and BB' in Fig. 2.11(c) and (d) are shown in Fig. 2.11(e). Fitting the curve by $\exp(-x/L)$, where x is the distance from Al contact (point A), *L* is estimated to be approximately 10 and 1.5 μm, respectively, on Si(111) and (001) substrates. The grain size is much smaller than the *L*, indicating that the grain boundaries do not works as recombination centers for minority carriers in $BaSi_2$ [26]. The grain boundaries properties are measured by Kevin probe force microscopy (KFM) as shown in Fig 2.12(a, b). According to averaged barrier heights in Fig. 2.12(c, d), the minority carriers are more likely to thermally activate, and the concave band structure at the grain boundaries are supposed to lead to the repulsion of photogenerated holes (n-type $BaSi_2$)[27]. Therefore, from the viewpoints of both the *L* and KFM, we can draw a conclusion that grain boundaries do not affect minority carrier movement on Si(111) substrate.

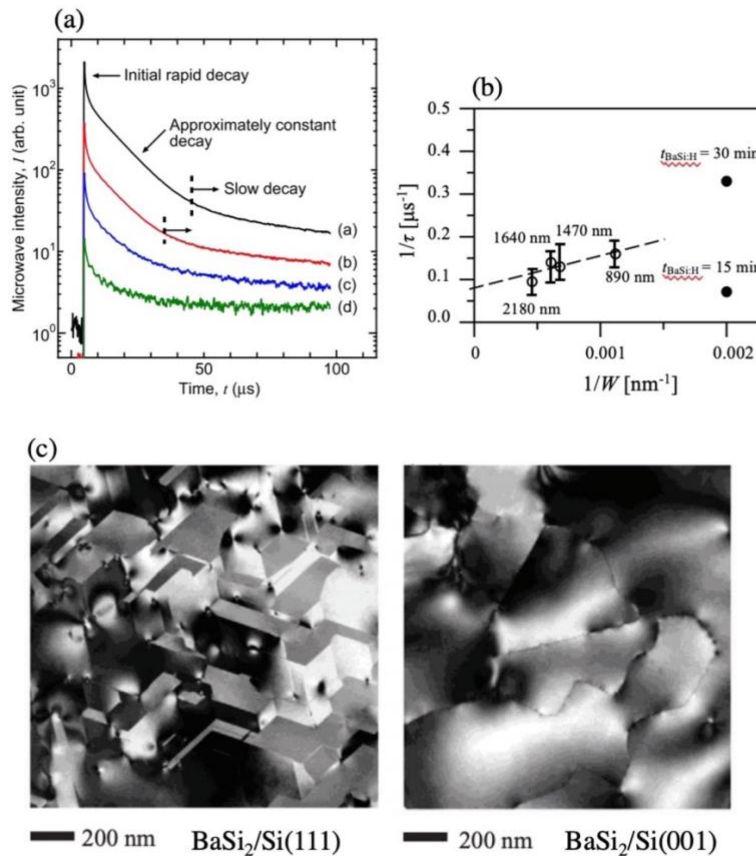

Fig. 2.10. (a) Photoconductivity decay curves of a $BaSi_2$ film with laser intensity of (A) 1.3×10^5, (B) 1.3×10^4, (c) 1.1×10^3, (d) 1.1×10^2 W/cm^2 [24]. (b) Dependence of the inverse of the carrier lifetime on the inverse of $BaSi_2$ layer thickness. (c) Plan-view TEM images of $BaSi_2$ on Si(111) and Si(001).

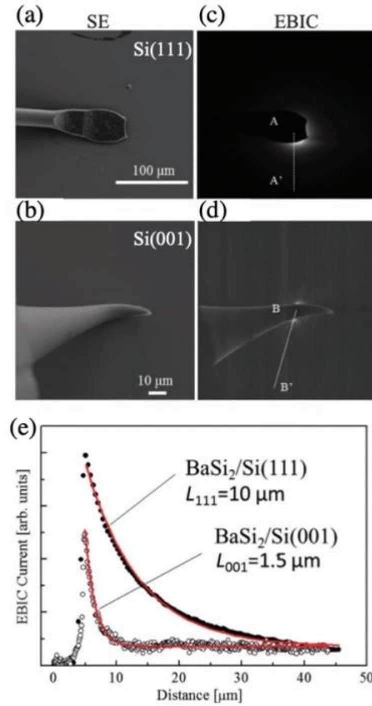

Fig. 2.11 (a, c) SE and EBIC image of $BaSi_2$ on Si(111). (b, d) SE and EBIC image of $BaSi_2$ on Si(001). (e) Experimental and simulated (solid lines) EBIC line-scan profiles along the dotted lines from A'-A in (c) and B'-B in (d) [26].

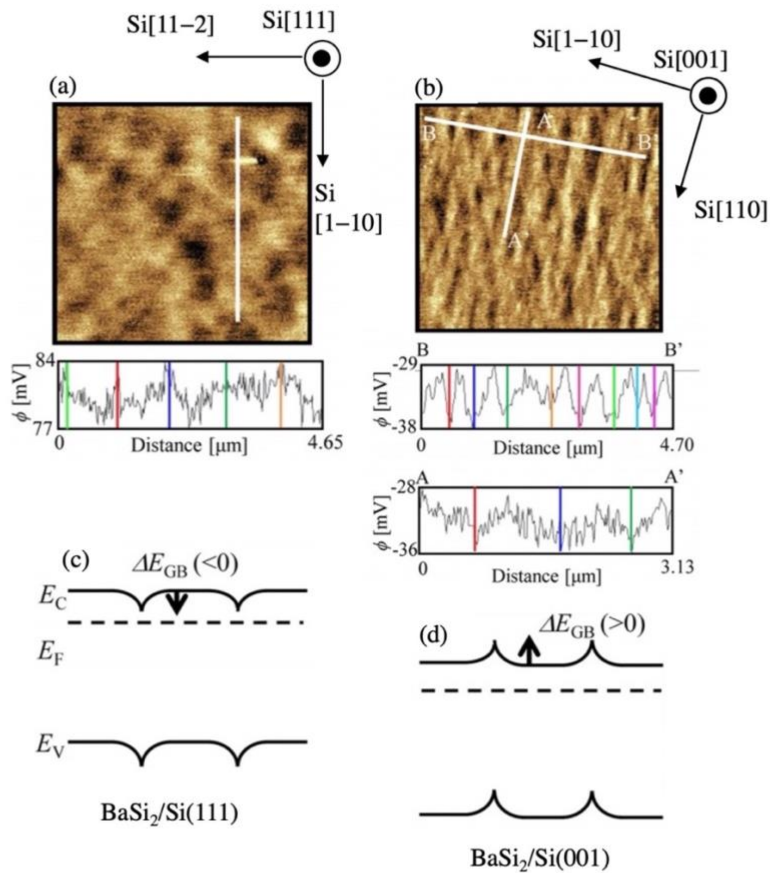

Fig. 2.12. KFM electrostatic potential images for undoped $BaSi_2$ film on Si(111)(a) and Si (001) (b). Band lineup around GBs for $BaSi_2$ on Si (111) (c) and Si(001) (d) [27].

2.4 Dopants

A *pn* junction is the basic structure of a solar cell. Thus, controlling the conductivity of $BaSi_2$ should be studied as the initial step. Usually, we co-deposit Ba, Si, and impurity atoms to form impurity-doped $BaSi_2$ on Si substrate or deposit impurity to $BaSi_2$ layer. Group 13th and 15th elements work as p- and n-type dopants, respectively. The majority carrier concentration is measured by the Hall effect using Van der Pauw method. At present, boron (B) is an excellent element to obtain p-type $BaSi_2$ in the hole concentration of 10^{16} – 10^{20} cm^{-3}, by controlling heating temperature of B source [28-30]. On the other hand, n-type $BaSi_2$ is fabricated using antimony (Sb) dopant, where the electron concentration is in the range of 10^{16} – 10^{20} cm^{-3}. However, the diffusion coefficient of Sb is very large. Thus, the Sb atoms diffuse into other layers easily. This degrades the quality of a *pn* junction and reduces electron concentration of Sb-doped $BaSi_2$ fims[31]. Table 1 summarizes the carrier type and concentration.

2.5 p-$BaSi_2$/n-Si heterojunction solar cell

In 2016, a 20-nm thick B-doped p-$BaSi_2$ on an n-Si substrate capped with a 3-nm thick amorphous Si (a-Si) was investigated. Under the air mass 1.5 (AM 1.5), the η reached 9.9%, the highest ever reported, thanks to the a-Si passivation layer. Figure 2.13(a)(b) show the sample cross-section and the current-voltage (J-V) curve. The short-circuit current density (J_{SC}) and open-circuit voltage (V_{OC}) are improved to 35.2 mA/cm^2 and 0.47 V, respectively, comparing to the sample without the a-Si passivation layer. Figure 2.13(c) shows the quantum efficiency (QE) spectra. The small contribution of $BaSi_2$ layer to external quantum efficiency EQE($BaSi_2$) is approximately 20% in the wavelength of 400–600 nm. Whereas, the large contribution of EQE is from the Si substrate. The small V_{OC} (0.47) is due to a small built-in field of approximately 0.2 V and the defects at the heterointerface. Thus, the photogenerated carriers are not separated effectively by the built-in field but by the large band offset due to the small electron affinity of $BaSi_2$ (3.2 eV) as shown in Fig 2.13(d). To overcome these two disadvantages, we move forward to the $BaSi_2$ homojunction solar cell [39-41].

2.6 n^+-$BaSi_2$/p-$BaSi_2$/p^+-$BaSi_2$ homojunction solar cell

In 2019, Kodama *et al.* fabricated n^+-$BaSi_2$/p-$BaSi_2$/p^+-$BaSi_2$ homojunction diodes on a p^+-Si substrate, and first demonstrated the operation of a $BaSi_2$ homojunction solar cell. The 20-nm-thick n^+-$BaSi_2$ is fabricated by doping Sb to $BaSi_2$. The p^+-Si substrate is used because the large band offset at the p^+-$BaSi_2$/ p^+-Si interface is diminished as shown in Fig. 2.14(a). In the absorption layer of p-$BaSi_2$, the photogenerated carriers (holes) can be transferred from p^+-$BaSi_2$ to p^+-Si thanks to the tunnel junction formation at the interface. However, the photogenerated electrons can also pass through this interface and cause a current leakage. Figure 2.14(b) shows the internal QE (IQE) spectra of homojunction solar cells on p^+-Si substrates, obtained at a bias voltage of 0 V. It is clear to see that a negative value of IQE exists at λ = 800–1000 nm, wherein photons with those wavelengths are absorbed around the interface. Such current leakage is promoted because of the step bunching at the interface, where a number of defects exist [42]. Thus, reducing such leakage current by a heavily doped p^+-Si epitaxial layer on a medium-doped p-Si(111) substrate is required for the formation of a homojunction. Figure 2.14(c) shows the structure of a homojunction solar cell, a 500-nm thick p-$BaSi_2$ works as an absorption layer, where the most electron-hole pairs are generated here. Figure 2.14(d) shows that J-V, V_{OC} and J_{SC} are improved significantly because the implanted p^+-Si/p-Si substrate is used, where, V_{OC} = 0.11 V, J_{SC} = 9.42 mA/cm^2, and η =0.28% [43].

TABLE I Impurity doped $BaSi_2$ and carrier type

Dopant	Type	Concentration [cm^{-3}]	comments	Reference
Undoped	p or n	$10^{15} – 10^{18}$	Dependent on R_{Ba}/R_{Si}	[32]
N	p	$10^{16} – 10^{17}$	Plasma generator	[33]
P	n	$10^{16} – 10^{18}$	PH_3 gas	[34]
As	n	$10^{17} – 10^{18}$	GaAs source, under study	[35, 36]
Sb	n	$10^{16} – 10^{20}$	Large diffusion coefficient	[31]
B	p	$10^{16} – 10^{20}$	Controllable to p^+	[28-30]
Al	p	$10^{16} – 10^{17}$	Easy to oxidize	[37]
Ga	p	10^{15} , 10^{20}	Uncontrollable	[38]
In	p	$10^{16} – 10^{17}$	p^+ can't be achieved	[38]

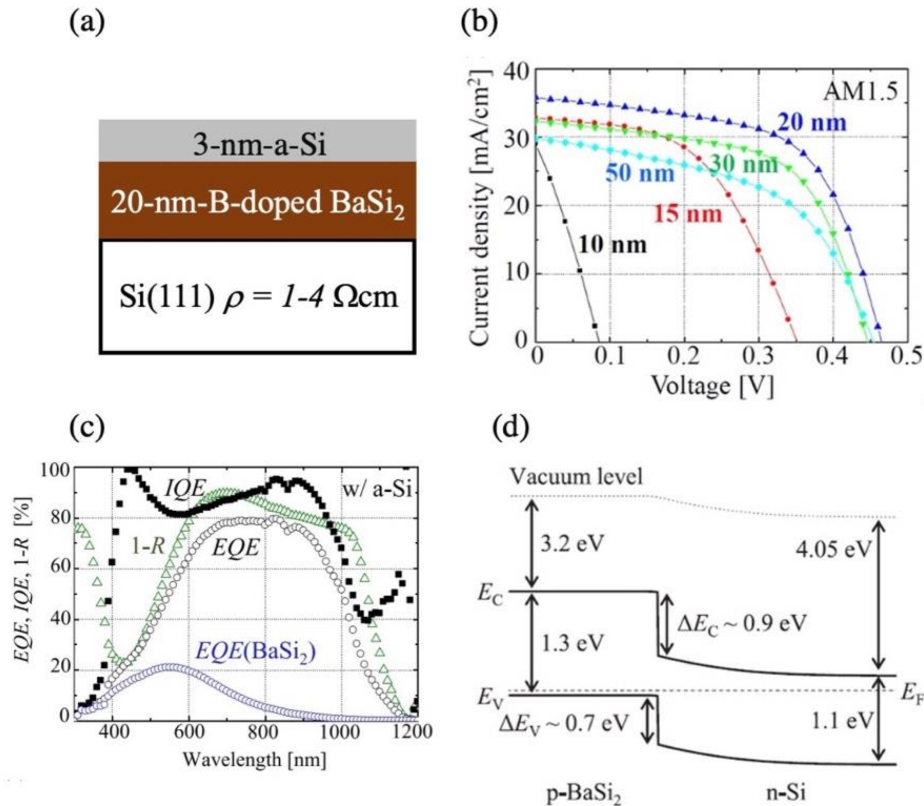

Fig. 2.13. (a) Cross-section of p-$BaSi_2$/n-Si heterojunction solar cell. (b) *J-V* curve of p-$BaSi_2$/n-Si heterojunction solar cell with different thickness of p-$BaSi_2$. (c) QE spectra of 20-nm-thick p-$BaSi_2$/n-Si. (d) Band structure of p-$BaSi_2$/n-Si [40,41].

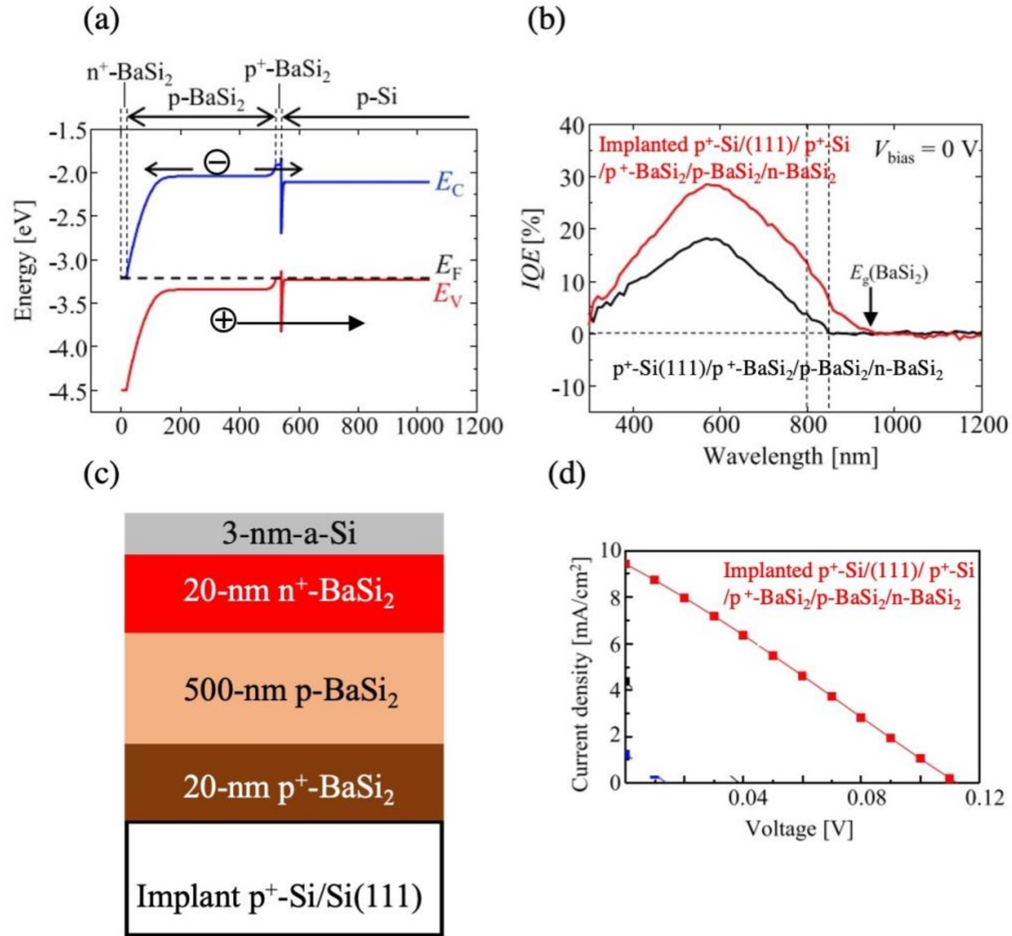

Fig. 2.14. (a) Band structure of $BaSi_2$ homojunction solar cell. (b) IQE spectra of $BaSi_2$ homojunction solar cell. (c) Cross-section of $BaSi_2$ homojunction solar cell. (d) *J-V* curve of $BaSi_2$ homojunction solar cell [43].

2.7 Aim of this work

To achieve a higher η of $BaSi_2$ homojunction solar cell, we must reduce defects in $BaSi_2$ absorption layers and at the heterointerfaces, and keep the number of defects as small as possible. These defects hinder the photogenerated carrier transport and diminish the τ. We have evaluated the defects by both theoretical calculation and experiment. According to first-principles calculation, from the viewpoint of formation energy, Si vacancies (V_{Si}) are most likely to be located in Si(3) site in Fig. 2.1 under both Si-rich or Si-poor growth conditions and generate the localized states within the band gap [44]. The presence of defects in $BaSi_2$ thin films and polycrystalline $BaSi_2$ bulk samples has been measured by deep-level transient spectroscopy (DLTS), Raman spectroscopy, electron paramagnetic resonance (EPR), and photoluminescence (PL) [45-48]. Figure 2.15(a) shows the DLTS profiles of a 500-nm thick undoped n-type $BaSi_2$ film on an n-Si(111) substrate. The rectifying properties of the *J-V* curve were confirmed. An upward facing peak, caused by a minority carrier (holes) trap, was observed at approximately 126 K. The trap level related to this hole trapping is calculated to be approximately 0.27 eV from the VBM, and its density is 1×10^{13} cm^{-3}. This defect is considered to be related to V_{Si} because its density is decreased close to the $BaSi_2$/Si interface. Figure 2.15(b) shows the vibration mode of Si tetrahedra with a V_{Si} at Si(3) site which causes the Raman peak at 477.7 cm^{-1}. This means that ~~by~~ V_{Si} can be detected by Raman spectra using a full width at half maximum. EPR is an effective method to characterize paramagnetic defects with an unpaired electron. Thanks to the applied magnetic field, the electron

energy level is divided and the unpaired electron oscillates between the separated energy level, shifting a g value. The angle dependent EPR spectra measured at 20 K fitted by three Lorentzian derivatives are shown in Fig. 2.15(c). One of these species corresponds to the isotropic line from the substrate (red line) while the two others marked orange and blue are related to the defects in the $BaSi_2$ thin film. Defects 1 and 2 are anisotropic, which are in complete agreement with a defect's origin in the $BaSi_2$ epitaxial film. Figure 2.15(d) shows an example of PL spectra at 8 K of 500-nm thick undoped $BaSi_2$ films with R_{Ba}/R_{Si} = 3.7. The λ of excited laser is 442 nm and the power is 60 mW/cm^2. Peaks from P1 to P4 are clearly fitted by Gaussian peaks, which are located at approximately 0.83, 0.95, 1.03 and 1.12 eV, respectively. Figure 2.15(e) shows the localized states within the band gap from the PL spectra.

As the discussion above, defects in $BaSi_2$ thin film degrade the performance of $BaSi_2$ solar cell. Now, some methods are applied to improve $BaSi_2$ thin film, such as the three-step growth method and post-annealing [49]. Hydrogen (H) passivation is used widely in a-Si or c-Si surface [50, 51]. The Si dangling bonds are terminated by atomic H. Thus, the density of dangling bonds of a-Si or Si surface are reduced significantly. Following this idea, my investigation is applying atomic H to $BaSi_2$ thin films using a plasma generator and characterize their properties. In this thesis, there are three main parts, including H passivated undoped $BaSi_2$ thin film, H passivated B-doped p-$BaSi_2$ films and Sb-doped n-$BaSi_2$ films, and H states and position in H passivated $BaSi_2$ detected by muon spin rotation.

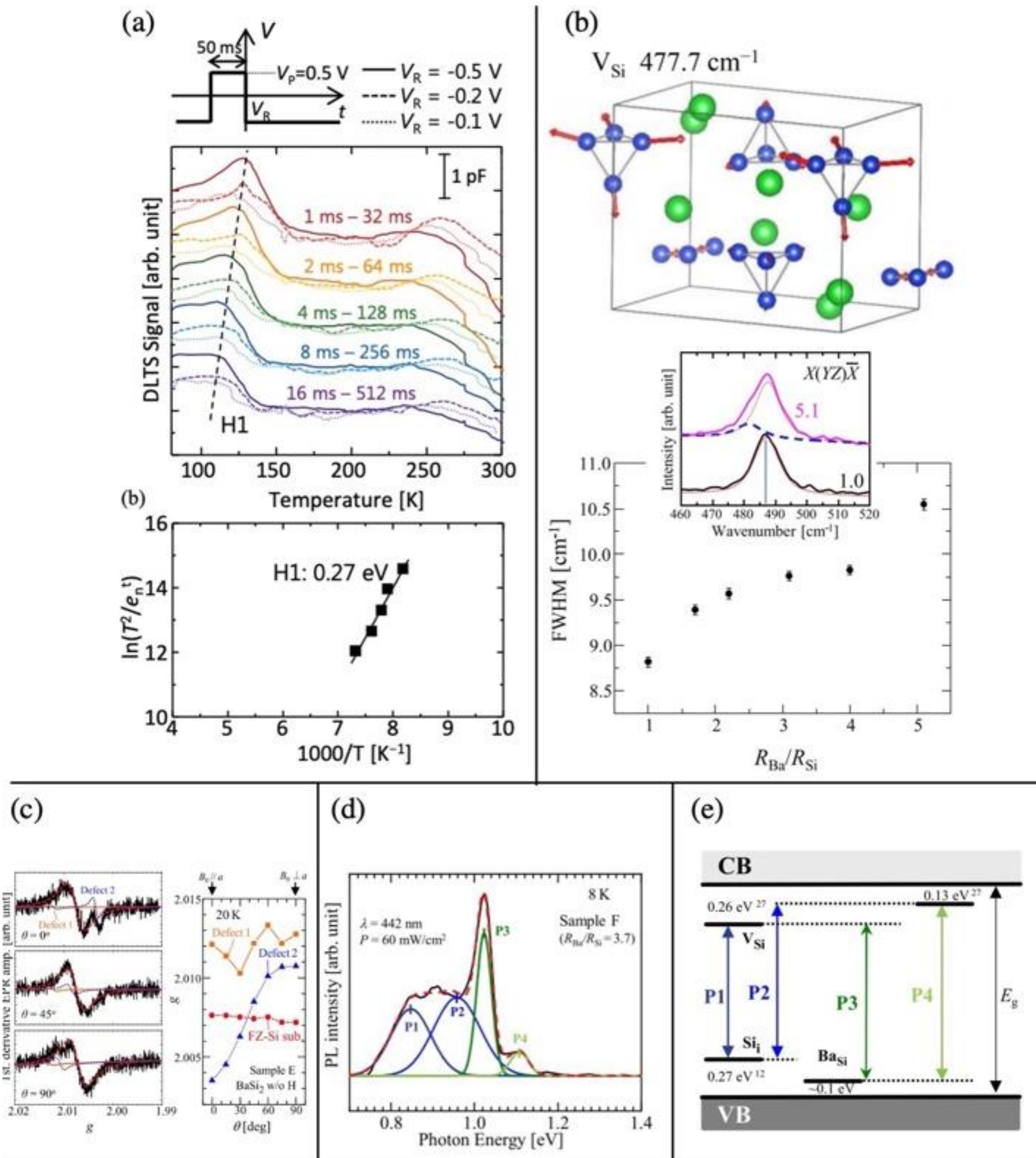

Fig. 2.15. (a) DLTS measurement shows the hole trap state exists below the conduction band minimum of 0.27 eV [45]. (b) Calculated phonon of Si tetrahedron with one V_{Si} [46]. (c) EPR results show two defects in $BaSi_2$ thin film [47]. (d) Measured PL spectra are fitted by four Gaussian peaks [48]. (e) The fitted four Gaussian peaks are corresponding to the four localized states in the band gap of $BaSi_2$ [48].

2.8 Reference

1. T. Suemasu, Jpn. J. Appl. Phys. **54**, 07JA01 (2015).
2. H. K. Janzon *et al.*, Allg. Chem. **372,** 87 (1970).
3. M. Imai and T. Hirano, Phys. Rev. B **58**, 11922 (1998).
4. Y. Imai *et al.,* J. Alloys Compd. **358**, 257 (2003).
5. I. L. Ivanenko *et al.,* Thin Solid Films, **461**, 141 (2004).
6. D. B. Migas *et al.,* Phys. Status Solidi b **244**, 2611 (2007).
7. M. Kumar *et al.,* Appl. Phys. Express **7**, 071203 (2014).
8. R. A. Mackee *et al.*, Appl. Phys. Lett. **63**, 2818 (1993).
9. R. Takabe et al., Jpn. J. Appl. Phys. **56**, 05DB02 (2017).
10. R. Koitabashi *et al.,* "High-photoresponsivity $BaSi_2$ films on glass prepared by radio-frequency sputtering for solar cell applications" submitted.
11. R. Koitabashi *et al.,* Appl. Phys. Express **13**, 075506 (2020).
12. K. Toh, *et al.,* Jpn. J. Appl. Phys. **51**, 095501 (2012).
13. N. A. A. Latiff et al., Phys. Status Solidi C **10**, 1759 (2013).
14. S. Matsuno *et al.,* Appl. Phys. Express **11**, 031302 (2018).
15. T. Nemoto e*t al.,* Jpn. J. Appl. Phys. **59**, SFFA06 (2020).
16. T. Nemoto *et al.,* Appl. Phys. Express **13**, 085511 (2020).
17. M. Somer *et al.,* Z. Allg. Chem. **626**, 2478 (2000).
18. K. Toh *et al.,* Jpn. J. Appl. Phys. **50**, 068001 (2011).
19. K. Morita *et al.,* Thin Solid Films **515**, 8216 (2007).
20. Y. Imai and A. Watanabe, Intermetallics **18**, 1432 (2010).
21. J. A. Hornbeck and J. R. Haynes, Phys Rev. **97**, 311 (1955).
22. D. Macdonald and A. Cuevas, Appl. Phys. Lett. **74**, 1710 (1999).
23. Y. Hu *et al.,* J. Appl. Phys. **111**, 053101 (2012).
24. K. O. Hara *et al.,* J. Appl. Phys. **112**, 083108 (2012).
25. K. O. Hara *et al.,* Appl. Phys. Express **6**, 112302 (2013).
26. M. Baba *et al.,* Jpn. J. Appl. Phys. **112**, 083108 (2014).
27. M. Baba *et al.,* Appl. Phys. Lett. **103**, 142113 (2013).
28. A. Khan *et al.,* Thin Solid Films **552**, 95 (2014).
29. A. Khan *et al.,* Appl. Phys. Lett. **102**, 112107 (2013).
30. A. Khan *et al.,* Appl. Phys. Lett. **104**, 252104 (2014).
31. M. Kobayashi *et al.,* Appl. Phys. Express **1**, 051403 (2008).
32. R. Takabe *et al.,* J. Appl. Phys. **123**, 045703 (2018).
33. Z. Xu *et al.,* J. Cryst. Growth **471**, 37 (2017).
34. R. Takabe *et al.,* Phys. Status Solidi c **10**, 1753 (2013).
35. K. O. Hara *et al.,* Thin Solid Films **567**, 105 (2014).
36. S. Aonuki *et al.,* Jpn. J. Appl. Phys. **59**, SFFA01 (2020).
37. M. Takeishi *et al.,* Phys. Proc. **11**, 27 (2011).
38. M. Kobayashi *et al.,* Thin Solid Films **515**, 8242 (2007).
39. D. Tsukahara *et al.,* Appl. Phys. Lett. **108**, 152101 (2016).
40. S. Yachi *et al.,* Appl. Phys. Lett. **109**, 072103 (2016).
41. S. Yachi *et al.,* Jpn. J. Appl. Phys. **56**, 05DE03 (2017).
42. Y. Homma and N. Aizawa, Phys. Rev. B **62**, 8323 (2000).

43. K. Kodama *et al.,* Appl. Phys. Express **12**, 041005 (2019).
44. M. Kumar *et al.,* J. Mater. Chem. A **5**, 25293 (2017).
45. Y. Yamashita *et al.,* Jpn. J. Appl. Phys. **57**, 075801 (2018).
46. T. Sato *et al.,* J. Appl. Phys. **124**, 025301 (2018).
47. T. Sato *et al.,* Appl. Phys. Express **12**, 061005 (2019).
48. T. Sato *et al.,* Appl. Phys. Express **12**, 111001 (2019).
49. Y. Yamashita *et al.,* J. Appl. Phys. **126**, 215301 (2019).
50. J. L. Benton *et al.,* Appl. Phys. Lett. **36**, 670 (1980).
51. A. Alnuaimi *et al.,* Solar Energy **98**, 236 (2013).

.

Chapter 3 H passivated a-Si layer and undoped $BaSi_2$

3.1 Introduction

In the typical structure of a $BaSi_2$ solar cell, the top layer a-Si that prevents oxidation contains many dangling bonds acting as defects. Moreover, the bond configuration changes abruptly at the $BaSi_2$ surface. According to an analysis of the surface structure of $BaSi_2$ epitaxial layers using coaxial-collision ion scattering spectroscopy [1,2], an a-axis-oriented $BaSi_2$ epitaxial film is terminated by Si tetrahedra. Therefore, surfaces contain a high density of trap states within the band gap [3]. Such high defects degrade the solar cell performance especially in a short λ light region because a large α of $BaSi_2$ causes the light absorbed in the surface region. Thus, surface passivation is very important for $BaSi_2$, defects in both a-Si layer and surface of $BaSi_2$ can be reduced significantly. As mentioned in chapter 2, the defects (V_{Si}) is believed to generate the localized states in the band gap, leading to the degradation of the photogenerated-carriers properties of $BaSi_2$. The defect density is revealed to be in the range of 10^{13} cm^{-3} by DLTS. Therefore, passivation should be applied to reduce defects not only at the surface but also in the bulk region.

H passivation is widely used in semiconductors, such as Si-related materials to keep defects as low as possible. It is also used in state-of-the art heterojunctions with intrinsic thin-layer solar cells (chapter 1, Fig. 1.7(c)). Semiconductor is exposed to for example H-containing plasma during or after the sample fabrication. H atoms diffuse easily due to the light mass and more likely to form complexes with defects in samples. The investigation of H passivated acceptor and donor in c-Si bulk started at 1980's. B atoms act as a shallow acceptor in c-Si and generate p-type conductivity. Pankove *et al.,* are the first to find that the resistivity of B-doped c-Si is increased by sixfold by H incorporation, meaning that negatively charged B atoms change to neutral BH complex and hole concentration is decreased markedly by atomic H [4]. They also provide a model shown in Fig. 3.1(a). The B atom connects with three Si atoms which can be satisfied at any time, the fourth one providing the hole and one electron would occupy at this site from the H atom. These results are confirmed by the infrared spectroscopy and simulation by deuterium [5,6]. In phosphorous (P)-doped c-Si, atomic H makes electron concentration decrease slightly but the mobility increase. This demonstrates that H can passivate donors (P atoms) by associating with them to form neutral complex, rather than by producing spatially unrelated acceptors. Additionally, H diffusion is strongly dependent on donor concentration [7]. According to the calculation, a model likes Fig. 3.1(b) is proposed from the viewpoint of total energy. The P atom breaks its bond with H and leave a distance between P and H atoms. The interaction between P and H is weak but affects a Si-H vibration mode which causes Raman peak shift. Researchers find that the Si-H bond length shrinks by more than 0.01 nm. Therefore, the force, determining the H vibrational frequency is more sensitive to the presence of the P atom than their chemical difference. According to this mode, the calculated Raman shift is very close to the experimentally obtained Raman shift. In summary, the neutral complex exists in H passivated B-doped and P-doped c-Si and make the majority carrier concentration reduce more and less. However, based on the calculation, H and B are more likely to form BH complex in H passivated B-doped c-Si, while the H atom connects with a Si atom in H passivated P-doped c-Si. a-Si is the non-crystalline material which is long-range disordered. Comparing a-Si with the c-Si, a-Si has more defects due to long-range disorder. However, it is low cost in manufactory and can be deposited on flexible substrates such as glass, metal, and plastic. Besides that, the α is larger than that of c-Si. Thus, the thin-film a-Si has been studied for solar cell applications. Atomic H is applied to terminate the dangling bonds in a-Si to reduce defects, which is called hydrogenated a-Si (a-Si:H). The first a-Si:H was fabricated by plasma enhanced chemical vapor deposition (PECVD) [8], where silane gas was used. Now the η of a-Si:H is approximately 14% on a texture substrate

achieved by National Institute of Advanced Industrial Science and Technology (AIST) Japan [9].

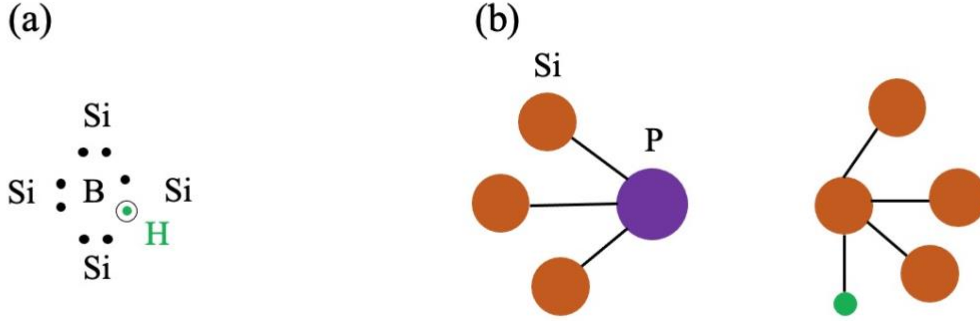

Fig. 3.1. (a) Electron configuration of BH in Si. (b) Electron configuration of PH in Si.

3.2 Experiment

1. Formation and characterization of $BaSi_2$ films capped with a-Si layers.

We used an ion-pumped MBE system equipped with a standard Knudsen cell for Ba, an EB gun for Si, and a radio-frequency (RF) plasma generator for atomic H. First, Ba and Si atoms were co-deposited on a low-ρ Czochralski-grown (CZ) n^+-Si(111) substrate (ρ = 0.01 Ωcm) at T_S = 580 °C to form a $BaSi_2$ epitaxial film with a thickness of approximately 500 nm, followed by a 3-nm-thick a-Si capping layer. We also used the low-ρ CZ n^+-Si(111) substrate for photoresponse measurements to exclude the contribution of photo-generated carriers in the n-Si substrate and form a good electrical contact at the $BaSi_2$/Si heterointerface. Details of samples are summarized in Table II. For samples A-C, we formed a-Si capping layers at a substrate temperature T_S = 180 °C. For samples D-H, a-Si layers are formed at various T_S from 160 to 260 °C, and atomic H is supplied at the same T_S for a duration ($t_{a\text{-}Si:H}$) of 15 min. We set the power of the RF plasma generator at 70 W and the vacuum level at 10^{-3} Pa during atomic H supply. The hydrogen plasma spectrum is measured by a spectrometer (QE Pro; Ocean optics). Raman spectra are measured by Raman spectrometer (JASCO, NRS-5100) using a frequency doubled Nd: YAG laser (532 nm, 5.1 mW). The spectral resolution is not worse than 4.2 cm^{-1}.

2. Formation and characterization of $BaSi_2$ films passivated by atomic H.

We next investigated the effect of atomic H on 500-nm-thick $BaSi_2$ epitaxial films. 500-nm-thick $BaSi_2$ films are grown epitaxially on the low ρ CZ n^+-Si(111) substrate at T_S = 580 ºC, and then atomic H is supplied to the $BaSi_2$ films with different durations ($t_{BaSi:H}$) at T_S = 580 ºC for samples 1-5 and at T_S = 180 ºC for sample 6. A reference sample, a 500-nm-thick $BaSi_2$ epitaxial film grown at T_S = 580 ºC on the low ρ CZ n^+-Si(111) substrate with a pure a-Si capping layer, is also fabricated and subjected to photoresponse measurements. The vacuum level and the RF power of the H plasma generator were set at 10^{-3} Pa and 10 W, respectively, to prevent surface damage. Carrier lifetime τ was measured for samples 7-9 grown on floating-zone (FZ) n-Si(111) substrates with high ρ (> 1000 Ωcm) by a microwave photo-conductivity decay (μ-PCD) measurement system (Kobelco, LTA-1512EP). Sample preparation for photoresponse and μ-PCD measurements is summarized in Table III. We also grew approximately 300-nm-thick $BaSi_2$ films at T_S = 580 ºC with different $t_{BaSi:H}$ = 0, 9, 15, and 30 min for depth profile of H atoms by secondary ion mass spectrometry (SIMS) using 5.0-kV Cs^+ primary ions. Figure 3.2(a) shows the fabrication procedure of a-Si:H on $BaSi_2$ thin film and Fig. 3.2(b) shows the procedure of H passivated $BaSi_2$ thin film.

TABLE II. Structure, substrate temperature (T_S), H supply duration ($t_{a\text{-}Si:H}$) for 3-nm-thick a-Si:H layer. The $BaSi_2$ layers are 500 nm thick and grown at 580 ºC.

Structure	Sample	T_S (ºC)	$t_{a\text{-}Si:H}$ (min)
	A	180	1
	B	180	15
	C	180	30
a-Si:H/$BaSi_2$(500 nm)/n^+-Si	D	160	15
	E	170	15
	F	190	15
	G	210	15
	H	260	15

TABLE III. Structure, H supply duration ($t_{BaSi:H}$), and substrate temperature (T_S) for 500-nm-thick $BaSi_2$ epitaxial layer growth of samples used to measure minority-carrier lifetime. Pure a-Si capping layers (3 nm thick) were deposited at 180 ºC.

Structure	Sample	$t_{BaSi:H}$ (min)	T_S (ºC)
	1	1	
	2	10	
	3	15	580
a-Si/$BaSi_2$:H/n^+-Si	4	20	
	5	30	
	6	15	180
	Reference	0	580
	7	1	
a-Si/$BaSi_2$:H/n-Si	8	15	580
	9	30	

For the photoresponse measurement, 80-nm-thick indium tin oxide (ITO) with a diameter of 1 mm is fabricated by sputtering onto the front sides of the samples and 150-nm-thick Al layers are deposited on their back sides. Photoresponse spectra are collected by a lock-in technique using a 150-W xenon lamp (Bunko Keiki, SM-1700A) and a single monochromator with a focal length of 25 cm (Bunko Keiki, RU-60N). The photoresponsivity R (A/W) for a given wavelength is obtained as follows. The alternating current components J(A/cm^2) caused by chopped light illuminations P (W/cm^2) and 77 Hz are measured on samples under bias voltages between the top and bottom electrodes by a lock-in technique. The R is given by J/P, and is measured from 300 to 1200 nm at an interval of 10 nm. The light intensity of the lamp is calibrated using a pyroelectric sensor (Melles Griot, 13PEM001/J). The crystalline quality of the grown films was characterized by x-ray diffraction (XRD; Rigaku Smart Lab) using a Cu Ka radiation source. The out-of-plane and in-plane XRD measurements reveal the a-, b-, and c-axis lattice constants using the Nelson-Riely relationship [10]. Ge(220) single crystals are set to monochromatize the x-ray beam. All measurements are performed at RT. The calculation is also performed to explain the electric properties of various $BaSi_2$ structure with V_{Si} and different numbers of incorporated H atoms. The full structural optimization and DOS calculations of the $2 \times 3 \times 2$ increased unit cell of $BaSi_2$ with and without H incorporation are performed by the first-principles total energy projector-augmented wave method (VASP code) with a plane-wave basis set [11-13]. The generalized gradient approximation of Perdew-Burke-Ernzerhof is used for the exchange and correlation potentials [14]. Total

energy minimization, via optimization of lattice parameters and relaxation of atomic positions using a conjugate gradient routine, is obtained by calculating the Hellmann-Feynman forces and stress tensor. Pulay corrections are included to compensate for changes of the basis set caused by variation in the shape of the unit cell. We set the energy cutoff at 325 eV. To perform integration over the Brillouin zone, we used a $5 \times 5 \times 5$ mesh of Monkhorst-Pack points, which is found to be sufficient to obtain convergence in the total energy of less than 0.001 eV per unit cell. The atomic relaxation is stopped when forces on the atoms were smaller than 0.05 eV/Å. Total DOS are calculated by the tetrahedron method with Blöchl corrections.

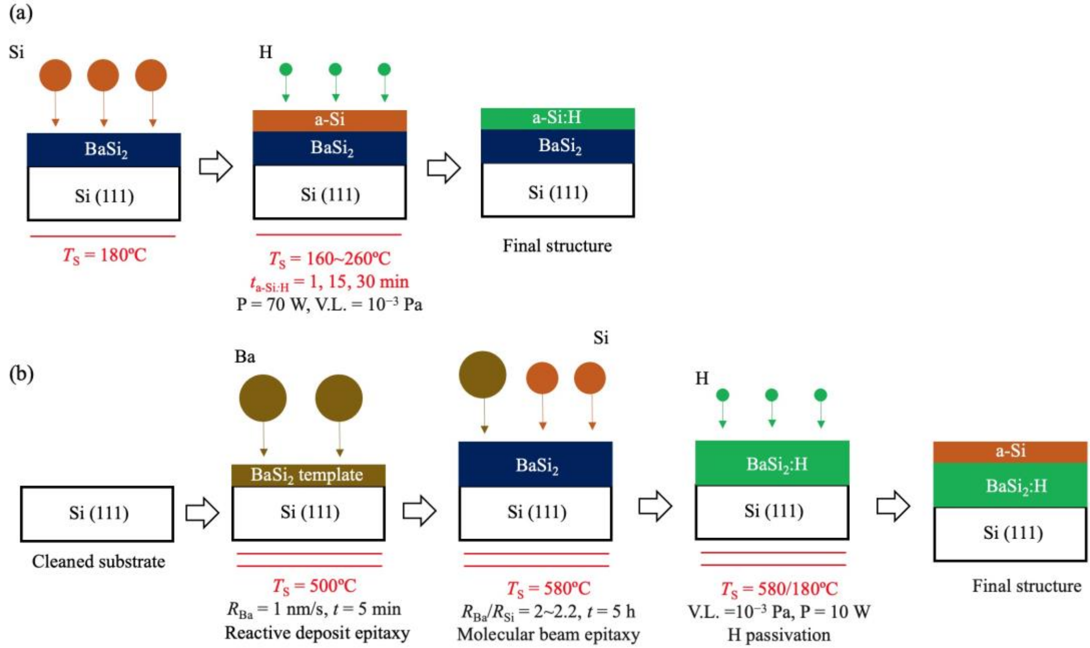

Fig. 3.2. (a) Fabrication procedure of a-Si:H on $BaSi_2$ thin film. (b) Fabrication of $BaSi_2$ thin film and irradiation of atomic H.

3.3 Results and discussion

Figure 3.3(a) shows a representative emission spectrum of H plasma obtained at 70 W. In the hydrogen plasma spectrum, three peaks demoted by E_{32}, E_{42}, and E_{52} correspond to electron transitions from excited states (n = 3, 4, and 5) to the first excited state (n = 2), respectively, belonging to the Balmer series [15]. The Raman spectrum of a-Si:H fabricated on Al layers at T_S = 180 ºC for 3h is shown in Fig. 3. 3(b). Raman peaks due to Si-Si bonds in a-Si such as transverse acoustic (TA) phonon and transverse optical (TO) phonon can be seen at around 180 and 480 cm^{-1}, respectively. In Fig. 3.3(b), no evidence of the peak at 520 cm^{-1} corresponding to TO phonons of c-Si is observed. These Raman peaks confirm that thin film is a-Si layers. Raman peaks corresponding to vibrations of Si-H bonds are observed at around 2,000 cm^{-1}, meaning that Si-H bonds are formed by the irradiation of H. However, the Si-H_2 bonds are not detected in this sample, which are considered to be responsible for light-induced degradation of a-Si solar cells [16]. Therefore, we believe that a-Si:H can be formed by an EB evaporation of Si and a supply of atomic H using an RF plasma gun.

Figure 3.4(a) shows the photoresponse spectra of samples A-C. The a-Si:H layers of those samples are formed at T_S = 180 ºC for $t_{a\text{-}Si:H}$ = 1, 15, 30 min, respectively. Since there is no built-in electric field in the $BaSi_2$ films, a bias voltage of 0.3 V is applied to the ITO electrode with respect to the Al electrode so that the photogenerated electrons are extracted to the front ITO electrode. The photoresponsivity begins to increase at λ shorter than approximately 1000 nm, corresponding to the band gap of $BaSi_2$. The smallest photoresponsivity is obtained for sample A fabricated with the shortest $t_{a\text{-}Si:H}$ of 1 min. The photoresponsivity improves

considerably by increasing $t_{a\text{-}Si:H}$ to 15 min (sample B). The photoresponsivity of sample B exceeded 1.4 A/W at λ = 800 nm. However, a further increase of $t_{a\text{-}Si:H}$ to 30 min (sample C) led to decreased photoresponsivity. We speculate that part of the a-Si capping layer changed to the c-Si phase when $t_{a\text{-}Si:H}$ = 30 min, and thus the passivation effect of the capping layer degraded. Sriraman *et al.* investigated H-induced crystallization of a-Si upon exposure to H through a combination of molecular-dynamics simulations and *in site* attenuated total-reflection Fourier transform infrared spectroscopy [17]. We therefore chose $t_{a\text{-}Si:H}$ = 15 min and optimized T_S between 160 and 260 ºC to prevent crystallization of a-Si by annealing [18,19]. The photoresponse spectra of samples B and D-H formed with $t_{a\text{-}Si:H}$ = 15 min and various T_S are shown in Fig. 3.4(b). The photoresponsivity is the highest for sample B (T_S = 180 ºC) and is lower for sample produced using either higher or lower T_S. These results indicate that the optimal growth conditions of an a-Si:H capping layer are $t_{a\text{-}Si:H}$ = 15 min and T_S = 180 ºC.

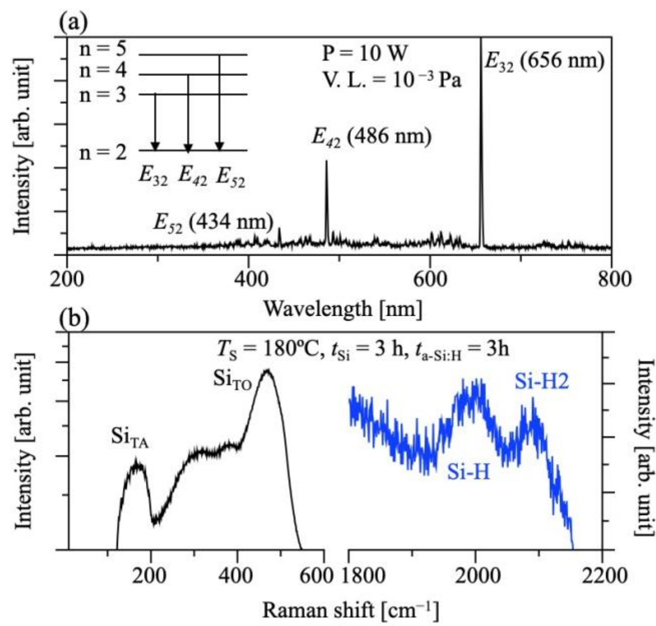

Fig. 3.3. (a) H emission spectra. (b) Raman spectra of a-Si:H

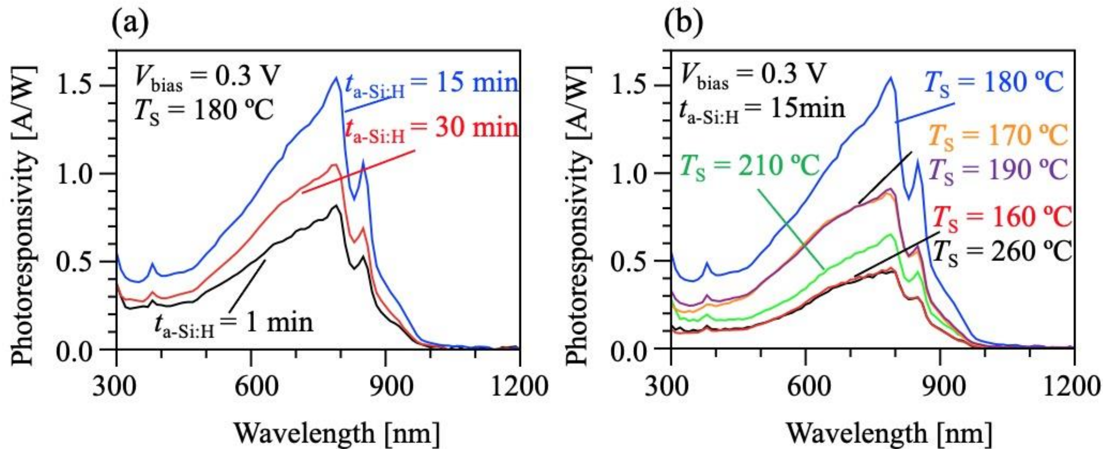

Fig. 3.4. (a) Photoresponsivity spectra of 500-nm-thick $BaSi_2$ layers capped with approximately 3-nm-thick a-Si:H fabricated with various $t_{a\text{-}Si:H}$. (b) Photoresponsivity spectra of 500-nm-thick $BaSi_2$ layers capped with approximately 3-nm-thick a-Si:H fabricated with various T_S.

Figure 3.5 shows the XRD patterns of sample 3 and reference. The $t_{BaSi:H}$ are set at 15 and 0 min, respectively. The diffraction peaks of only *a*-oriented $BaSi_2$ are observed, which are the same between with and without H supply indicating that the H-passivated $BaSi_2$ films are grown epitaxially likes the pure $BaSi_2$ thin film. The lattice parameter of $BaSi_2$ films (a, b, c) in sample 3 are calculated to be 0.893, 0.672 and 1.156 nm, respectively. The difference in lattice parameter between sample 3 and reference sample is within measurement errors. We also compared the crystalline quality of these samples by the full width at half maximum values obtained from an x-ray ω-scan rocking curve using a 600 reflection of $BaSi_2$. They are 0.487° and 0.475°, respectively. On the basis of these results, it is safe to state at least that there is not so much difference in crystalline quality of $BaSi_2$ films between with and without atomic H supply.

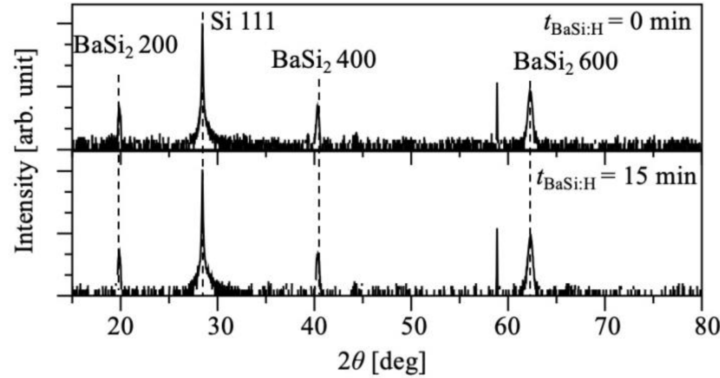

Fig. 3.5 XRD pattern of $BaSi_2$ with/without H passivation

Figure 3.6 shows the photoresponse spectra of samples 1-6 and the reference sample under a bias voltage of 0.3 V. For samples 1-5, H atoms are irradiated on 500-nm-thick $BaSi_2$ films at T_S = 580 ℃ for various $t_{BaSi:H}$ of 1 to 30 min after the growth of $BaSi_2$ films at T_S = 580 ℃. For sample 6, T_S is set at 180 ℃ and $t_{BaSi:H}$ is 15 min. Photoresponsivity increased with $t_{BaSi:H}$ up to 15 min and then decreased as $t_{BaSi:H}$ lengthened further. This behavior is caused by the passivation of defects in $BaSi_2$ by atomic H. The maximum photoresponsivity of about 2.5 A/W at λ = 800 nm is observed for sample 3 ($t_{BaSi:H}$ = 15 min). This value is approximately one order of magnitude higher than that reported previously [20], and much larger than that of sample B. The photoresponsivities of samples 2 ($t_{BaSi:H}$ = 10 min) and 3 ($t_{BaSi:H}$ = 15 min) are almost the same at λ < 500 nm. This behavior is believed to originate from saturation of passivated defects on the top surfaces of these samples. Photons with λ < 500 nm are absorbed in the region close to the surface of the $BaSi_2$ films because of high α of $BaSi_2$. Therefore, the results suggest that the recombination of photogenerated carriers is suppressed in the $BaSi_2$ films, especially in the surface region. Improved photoresponsivity compared with that of the reference sample was distinctly observed at λ > 500 nm for sample 1−3. We suppose that the H atoms might diffuse into deeper regions and passivate the defects in the bulk of $BaSi_2$. The photoresponsivity of the samples decreased

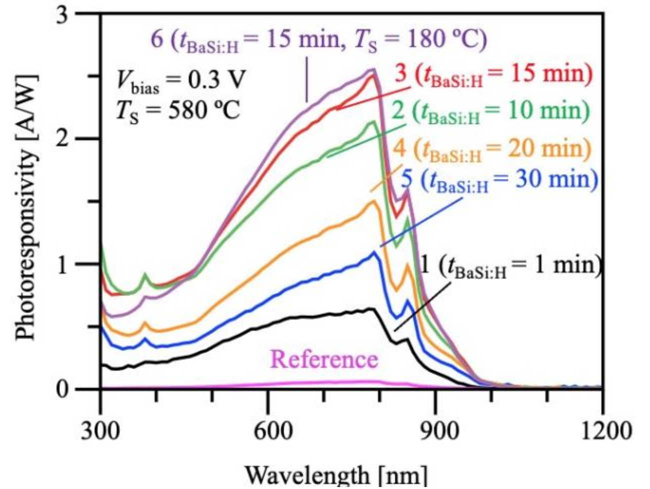

Fig. 3.6. Photoresponsivity spectra of 500-nm-thick $BaSi_2$ layers passivated by atomic H with various values of $t_{BaSi:H}$ in the range of 0−30 min.

markedly when $t_{BaSi:H}$ is longer than 15 min. Comparing the photoresponsivity of sample 6 ($t_{BaSi:H}$ = 15min, T_S = 180 ºC) and sample 3 ($t_{BaSi:H}$ = 15min, T_S = 580 ºC) indicates that the photoresponsivity improvement is independent of T_S . We speculate that H atoms diffuse sufficiently in $BaSi_2$ even at such a low T_S. In monocrystalline Si, the diffusion coefficient of H is large even at low temperatures [21]. These results provide strong evidence that H irradiation is a practical method to passivate defects and thereby enhance the photoresponsivity of $BaSi_2$.

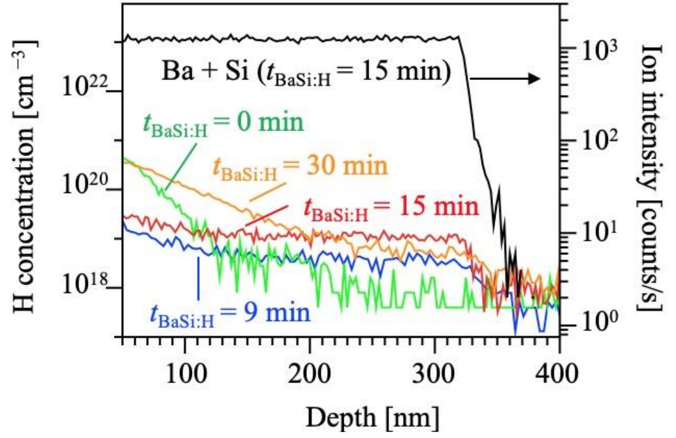

Fig. 3.7. SIMS profile of H passivated $BaSi_2$.

Next, we discuss the SIMS depth profile of H and the secondary ion (Ba + Si) intensities of approximately 300-nm-thick $BaSi_2$ films grown at T_S = 580 ºC with various $t_{BaSi:H}$ in the range of 0–30 min, followed by capping with 3-nm-thick pure a-Si layers at T_S = 580 ºC. As shown in Fig. 3.7, the concentration of H atoms increased gradually with $t_{BaSi:H}$, and is uniformly distributed in the samples with $t_{BaSi:H}$ = 9 and 15 min. In the sample with $t_{BaSi:H}$ = 30 min, however, the H concentration is not uniform. At $t_{BaSi:H}$ = 15 min, the H concentration reaches about 1×10^{19} cm^{-3} at the depths of 20−320 nm from the surface. This H concentration is higher than that of the sample with $t_{BaSi:H}$ = 0 min. This is because H_2 molecules are difficult to evacuate from the ion-pumped MBE chamber. We therefore consider that H_2 molecules might enter $BaSi_2$ films during sample fabrication; however, the defects in $BaSi_2$ are not passivated by H_2, resulting in such a low photoresponsivity.

According to the marked improvement of the photoresponsivity of the atomic H-passivated $BaSi_2$, it is reasonable to consider that τ is improved for this sample. In this work, the photoresponsivity of $BaSi_2$ films is measured using the photoconduction effect. The photoresponsivity is roughly proportional to the ratio of the carrier lifetime to carrier transit time [22]. Thus, we attribute the increase of photoresponsivity to the increase of carrier lifetime and/or the decrease of carrier transit time. To confirm the increase of carrier lifetime, we performed μ-PCD measurements on samples 7−9, whose growth conditions are the same as those used for samples 1, 3, and 5, respectively, except for the Si substrate used. For μ-PCD measurements, we used high-ρ FZ-Si substrates to decrease the microwave intensity reflected from the Si substrate.

Figure 3.8(a) shows the photoconductivity decay curves of samples 7−9 excited by a pulsed laser intensity of 1.3×10^5 W/cm^2. Assuming that the reflectivity of microwaves is proportional to the excess carrier concentration, we can deduce τ from the decay curves. Electron-hole pairs are generated by the 5-ns laser pulse in a spot with a 2-mm diameter at λ = 349 nm (3.55 eV). The photoconductivity decays is measured from the reflectivity microwave with a frequency of 26 GHz. The estimated areal photon density is $1.3 \times 10^5 \times 5 \times 10^{-9}/(1.6 \times 10^{-19} \times 3.55) \approx 1.1 \times 10^{15}$ cm^{-2}. The α at λ = 349 nm is higher than 5×10^5 cm^{-1}, and thus the penetration depth of the laser light is $1/\alpha \times 3 \approx 60$ nm, indicating that most of photons are absorbed in the H-passivated $BaSi_2$ layer. Assuming that photogenerated carriers are diffused and uniformly distributed over the 500-nm-thick H-passivated $BaSi_2$ films, the electron-hole pairs concentration is estimated to be 2.2×10^{19} cm^{-3} on average. Here, we define $t_{1/e}$ as the time when the reflected microwave intensity decreases by exp(−1) of the initial value after the excitation laser is turned off, which is shown in Fig. 3.8(a). $t_{1/e}$ is determined to be approximately 1, 14, and 3 μs for samples 7, 8, and 9, respectively. Note that the measured $t_{1/e}$ depends on the thickness of the $BaSi_2$ film, because excess carriers reaching the surface or interface of the samples recombine with defective states located there. Figure 3.8(b) compares $t_{1/e}$ obtained for samples 8 and 9 in this work as a

function of $BaSi_2$ thickness (W) [23]. In ref. 23, we deduced the τ of $BaSi_2$ films from the slope of the decay curves in the time range after the initial rapid decay. In this sense, the $t_{1/e}$ values are underestimated in this work compared to the previous result in ref. 23. Although the $t_{1/e}$ of sample 7 is out of the range, the effect of atomic H passivation of $BaSi_2$ films on t is verified especially in sample 8.

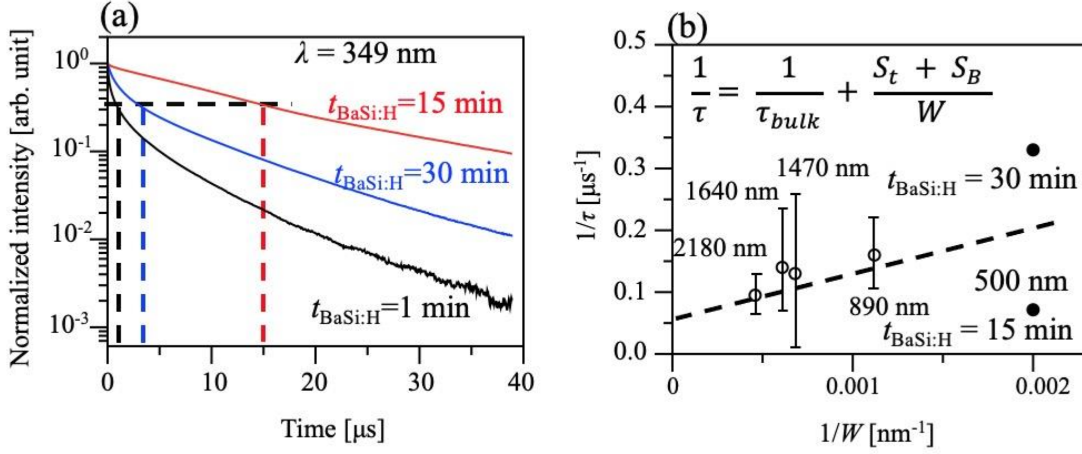

Fig. 3.8. (a) Photoconductivity decay curves of atomic H passivated $BaSi_2$. (b) Comparison of τ obtained for samples as a function of $BaSi_2$ thickness W to those reported previously.

The majority carrier concentrations and Hall mobilities of samples 7-9 are measured at RT using the Van der Pauw method. The concentrations are: sample 7, p-type, $p = 1.1 \times 10^{17}$ cm^{-3}, hole mobility = 25 cm^2/Vs; sample 8, p-type, $p = 1.8 \times 10^{17}$ cm^{-3}, hole mobility = 97 cm^2/Vs; sample 9, n-type, $n = 9 \times 10^{15}$ cm^{-3}, electron mobility = 1240 cm^2/Vs. These results reveal that the type of majority carriers changed from holes to electrons as $t_{BaSi:H}$ is increased from 1 to 30 min.

This is the first time to improve the τ and lead to the photoresponsivity increasing significantly. Thus, it is worthwhile to investigate the τ of the H-passivated $BaSi_2$ by considering various recombination mechanisms. The photoconductivity is defined by

$$\sigma(t) = q[(n + \Delta n(t))\mu_n + (p + \Delta p(t))\mu_p]. \quad (3.1)$$

where q is the elementary charge; $\Delta n(t)$ and $\Delta p(t)$, are the time-dependent nonequilibrium (photo-generated) electron and hole concentration, respectively ($\Delta n(t) = \Delta p(t)$); n and p are the equilibrium electron and hole concentrations, respectively. The decrease of the photoconductivity after the irradiation is stopped is defined by the decrease of the nonequilibrium charge carrier concentrations over time caused by the recombination processes in semiconductors. The $\Delta n(t)$ and $\Delta p(t)$ dependencies can be found from a continuity equation and expressed by

$$\frac{d\Delta n(t)}{dt} = -\sum_{i} R_i , \quad (3.2)$$

where R_i is the i-th mechanism of recombination rate. Actually, at low temperatures likes 10 K, very weak photoluminescence (PL) is observed, but it vanishes at higher temperatures such as 40 K. Thus, we do not consider the radiative recombination process at RT. The Auger processes become the most favorable for highly nonequilibrium carrier concentrations (usually more than 10^{17} cm^{-3}) [24, 25]. In a general case, the following Auger processes occur: (1) direct band to band Auger recombination, (2) phonon-assisted band to band Auger recombination, and (3) Auger capture by various traps. Each of these processes has its own recombination rate. Direct band-to-band Auger recombination has an energy threshold. Generally, this energy threshold is rather

high for indirect-gap semiconductors, which means that this Auger process becomes ineffective. Therefore, this channel of nonradiative recombination can play a substantial role only in narrow-gap ($\leq$ 0.3 eV) and gapless semiconductors. Also, this type of recombination may be important if there are so-called "resonances" in the energy structure of semiconductors caused by the specific features in the energy bands, which are defined by the spin-orbit splitting of the valence band. However, this is not the case of the band structure of $BaSi_2$. So we excluded the direct band-to-band Auger recombination processes from further consideration. The average optical phonon energy is $E_{\text{optical phonon}} = \hbar\omega_{\text{opt}}$, where $\hbar$ is the Planck constant and ω_{opt} is the characteristic frequency of the optical branch of the phonon spectrum (493 cm^{-1} for a Ag mode of $BaSi_2$) [26, 27]. $E_{\text{optical phonon}}$ is about 0.06 eV at RT. The same analyses for acoustic phonons using the appropriate Debye temperature of 260 K [28] gave a value of about 0.02 eV. For the phonon-assisted band-to-band Auger recombination process to occur in $BaSi_2$, which has a band gap of 1.15−1.30 eV, it is necessary to generate or absorb numerous phonons simultaneously. However, such multi-phonon processes are rather rare events [24] and the subsequent probability of recombination via this channel was estimated to be negligible. Thus, we excluded phonon-assisted band-to-band Auger recombination processes from further consideration as well. Therefore, Auger captures by various types of traps are considered to be the main recombination mechanism in $BaSi_2$ films. The recombination is finally described by the well-known and very general bi- and monopolar decay rate equation:

$$\frac{d\Delta n}{dt} = -\left(A_{\text{trap}}N\Delta n^2 + B_{\text{trap}}N\Delta n\right). \tag{3.3}$$

Here, A_{trap} is the coefficient of Auger capture by traps and N is the trap concentration. Because N cannot be directly obtained or estimated from the experimental data, it is treated as a parameter of the model.

$$A_{trap} = \left(\frac{q^2}{4\pi}\right)^2 \frac{m^*}{\hbar^3}\frac{1}{\varepsilon^2}(4\pi R^2)^3, \tag{3.4}$$

where ε is the static dielectric constant (14.6 for $BaSi_2$), m^* is the carrier effective mass (0.41 and 0.53 for electrons and holes in $BaSi_2$, respectively, in units of free electron mass), and R is the radius of the trap. R is usually about 10 nm for shallow levels and < 1nm for deep levels in the band gap region [25]. A_{trap} is 9.879×10^{-28} and 1.3×10^{-27} cm^6/s for electrons and holes, respectively. B_{trap} is the capture coefficient for any potential of the attracting center and any mechanism of energy loss. In particular, for the Coulomb potential and the energy relaxation related to the interaction of carriers with phonons, B_{trap} is defined as

$$B_{trap} = \frac{(2\pi)^{1.5}\hbar^3}{m^{*1.5}(k_{\text{B}}T)^{0.5}}\left[\int_0^\infty \frac{\exp\left(\frac{E}{kT}\right)}{C(E)}dE\right]^{-1}, C(E) = \frac{4m^*(Zq^2)^3}{3\pi El(\varepsilon\hbar)^3}. \tag{3.5}$$

Here, E is the energy, l is the mean free path of carriers, and Zq is charge of the center. Under such assumptions and by solving Eq. (3.3), the nonequilibrium carrier concentration is defined by

$$\Delta n(t) = \frac{B_{\text{trap}}N\Delta n_0\exp\left(-B_{\text{trap}}Nt\right)}{A_{\text{trap}}N\Delta n_0 + B_{\text{trap}}N - A_{\text{trap}}N\Delta n_0\exp\left(-B_{\text{trap}}Nt\right)}. \tag{3.6}$$

Here Δn_0 is the steady-state nonequilibrium electron concentration (2.2×10^{19} cm^{-3}) reaching during irradiation. The B_{trap} values for electrons and holes are calculated by different q due to $t_{\text{BaSi:H}}$.

The experiment results of Fig. 3.9 are fitting by Eq. (3.6), the N is a parameter of the model for the normalized photoconductivity versus time for samples 7-9. N is estimated 6.5×10^{13}, 2.2×10^{12}, and 2.1×10^{13} cm^{-3}. These results are in good agreement with the DLTS results, where the N is evaluated to 10^{13} cm^{-3}.

The photoconductivity drops at the initial stage (from 0 to 5 μs) after the irradiation is stopped. When the

nonequilibrium carrier concentration (photogenerated-carriers) is high, this drop is mainly defined by the Auger recombination by various types of traps. The more pronounced decrease in photoconductivity for the samples with $t_{BaSi:H}$ = 1 and 30 min compared with that for the sample with $t_{BaSi:H}$ = 15 min is caused by the higher trap concentrations. From 5 to 30 μs, the photoconductivity decrease is defined by the simultaneous influences of Auger recombination and phonon-assisted capture of carriers by traps. Thus, the Auger processes initially play a dominant role and then the valuable contribution of the phonon-assisted processes appears over time because of the decrease of the carrier concentration and, as a consequence, the decrease of the rate of the Auger recombination. After 30 μs, the photoconductivity is mainly defined by the phonon-assisted capture of carriers by traps.

We next try to understand the photoresponsivity results from the viewpoint of DOS using the first-principles calculation. Here, *ab initio* modeling of various $BaSi_2$ structures with V_{Si} and incorporated H atoms is performed.

$BaSi_2$ is a simple orthorhombic structure (space group *Pnma*) and has lattice parameters of a = 0.8942 nm, b = 0.6733 nm, and c = 1.1556 nm. In a $BaSi_2$ crystal, 8 Ba and 16 Si atoms are grouped into two and three chemically inequivalent sites, respectively. A structural feature of this crystal structure is the presence of slightly distorted isolated Si_4 tetrahedra that act as anions in the sublattice of Ba atoms, which can be viewed as cations, indicating that the mostly ionic nature of the chemical bonding in a $BaSi_2$ crystal, although covalent bonding prevails within Si_4 tetrahedra.

$BaSi_2$ thin films contain grain boundaries, which can be considered as a primary site of H incorporation. An *ab initio* study of $BaSi_2$ monocrystalline thin films with different orientations indicates the presence of some surface-localized states within the band gap when Si_4 tetrahedra are present on the surface, whereas Ba surface termination resulted in lower surface energies and the absence of surface-localized states [3]. In addition, both Ba and Si vacancies are not excluded on the surface, providing there is enough room for H to saturate dangling bonds. Unfortunately, it is not yet possible to model real grain boundaries because of their numerous structural variants. However, $BaSi_2$ grains are rather larger (0.2 μm on average) with respect to the grain boundary area and we can consider that the bulk of $BaSi_2$ to absorb most of H. In bulk $BaSi_2$, H can occupy a V_{Si} or enter an interstice. In the former case, three H atoms are necessary to formally saturate all dangling bonds in the tetrahedra with one Si atom removed. Moreover, an enlarged unit cell is necessary for simulations to prevent a sizable defect-defect interaction since even in our enlarged unit cell, the defect concentration is larger than 10^{20} cm^{-3}.

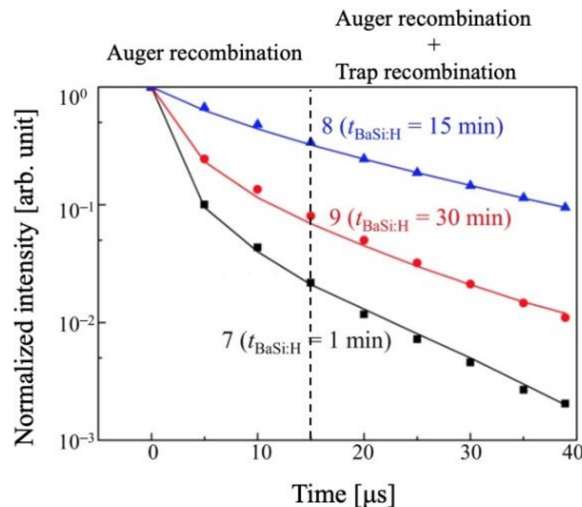

Fig. 3.9. Normalized photoconductivity of $BaSi_2$ versus time.

The relaxed structure of $BaSi_2$ is very similar to the experimental ones. Any structural variant of $BaSi_2$ with V_{Si} and/or with H incorporation do not show significant changes in the lattice parameters in accordance with the XRD results. However, we find that valuable changes in a Si_4 tetrahedron with V_{Si}: the Si-Si interatomic distances get shorter (0.233−0.239 nm to be compared to 0.241−0.245 nm for the ordinary Si_4 tetrahedron). Such distortion could be viewed to be local because it does not affect atomic positions of the other atoms. Additionally, since there is enough space to use several H atoms to saturate dangling bonds in the case of V_{Si}, H incorporation causes again local distortion. The corresponding calculated DOS of $BaSi_2$ with one V_{Si} along with the cases of incorporation of one, two, and three H atoms to passivate dangling bonds in a tetrahedra are shown in Fig. 3.10. There is no sizable change in the E_g value, in the structure of the valence and conduction bands as well as in the character of the states which define different hybridizations of bonding states in the valence band and antibonding states in the conduction band with respect to the ideal $BaSi_2$ structure. Usually the appearance of point defects in an ideal structure provides additional energy levels in the gap region associated with these defects. And in its turn, they could lead to the drastic changes in the transport properties as well as in some dynamical characteristics of relaxation processes of the system under consideration. In the case of $BaSi_2$ with V_{Si}, it is evident that the V_{Si} causes a localized state consisting of two energy bands to appear close to the middle of the band gap region. This localized state is half filled, which originates from *p* states of Si atoms belonging to the tetrahedron with the removed Si atom and act as a trap. One H atom can saturate only one dangling bond of the Si atom in the tetrahedron with the V_{Si}. In this case, there is one half-filled energy band in the localized state, which leads to a decrease of the trap concentration because the intensity is reduced. If two H atoms saturate dangling bonds, the completely filled localized state (consisting of one energy band, which is characterized by *p* states of the one remaining Si atom with a dangling bond) shifts towards the top of the valence band and acts as a deep donor level. Incorporation of a third H provides complete termination of all dangling bonds and lead to degenerate semiconductor properties because the Fermi level is in the conduction band, equivalent to the scenario if one electron is added to the system. We also investigate two distinct variants in the case of an interstitial H atom in the $BaSi_2$ unit cell, as shown in Fig. 3.11. The first one is very similar to the case of three H atoms and V_{Si} with degenerate semiconducting properties. It corresponds to the case when the first neighbor of H is a Ba atom. The second one occurs if the first neighbor of H is a Si atom and suggests formation of a trap in the middle of the gap because it has a half-filled localized state originating from H *s*, Si *p* and Ba *d* states.

It should be stressed that all the studied structures can statistically occur in the systems under consideration. Therefore, the structure of the sample without H passivation and $t_{BaSi:H}$ = 1 min can be characterized mainly by the presence of the case represented in Fig. 3.10(a) and (b), respectively. These situations lead to a high trap concentration and photoresponsivity is low. As the H concentration is increased, which is corresponding to $t_{BaSi:H}$ = 15 min, the situation may be defined mainly by Fig. 3.10(c). The localized states are filled by electrons, and thus they are inactivated. Finally, when the H concentration is maximal, like in the sample fabricated with $t_{BaSi:H}$ = 30 min, the structure is characterized by the cases represented in Fig. 3.10(d) and Fig. 3.11. Three H atoms completely passivate all dangling bonds of the V_{Si} and an ideal $BaSi_2$ crystal with one H in an interstice, respectively. On one hand, the maximum H concentration leads to the change of major charge carrier, and on the other hand, to an increase of the trap concentration. Unfortunately, the experimentally determined trap concentration value of about 10^{13} cm^{-3} cannot be treated directly by *ab initio* calculations because of the serious limitations on the size of the considered systems. In the enlarged unit cell, we use for calculations the minimal defect concentration which cannot be less than 10^{20} cm^{-3}, indicating that it is impossible to completely attenuate the defect-defect interaction. As a result, localized bands with very low dispersion appear in the energy gap region due to interaction of Si atoms with dangling bonds in a tetrahedron with V_{Si}. However, in the direct

space, everything is localized within the area of a tetrahedron with V_{Si}, indicating that our *ab initio* analysis is correct and can only help one to understand qualitatively the influence of H incorporation into $BaSi_2$ on its properties. Fig. 3.12−14 show the crystal structures of one H, two H, and three H in $2 \times 3 \times 2$ increased unit cell of $BaSi_2$ with a V_{Si}. In each case, several models are proposed from the viewpoint of the formation energy.

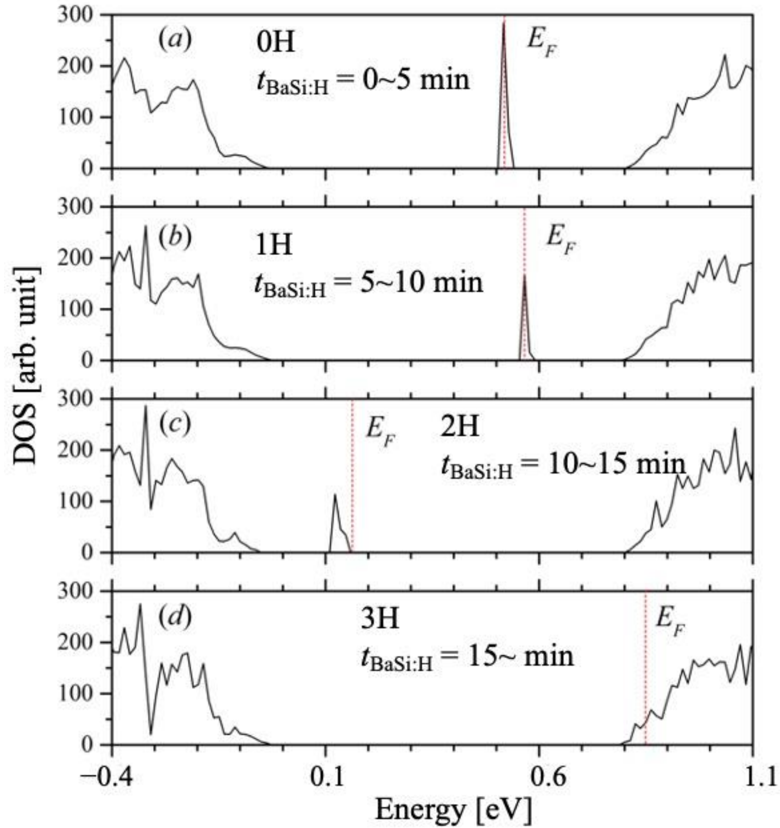

Fig. 3.10. Total density of states of enlarged $BaSi_2$ unit cells with (a) one V_{Si}, (b) one H atom in a V_{Si}, (c) two H atoms in a V_{Si}, and (d) three H atoms in a V_{Si}. The vertical dashed line indicates the Fermi level.

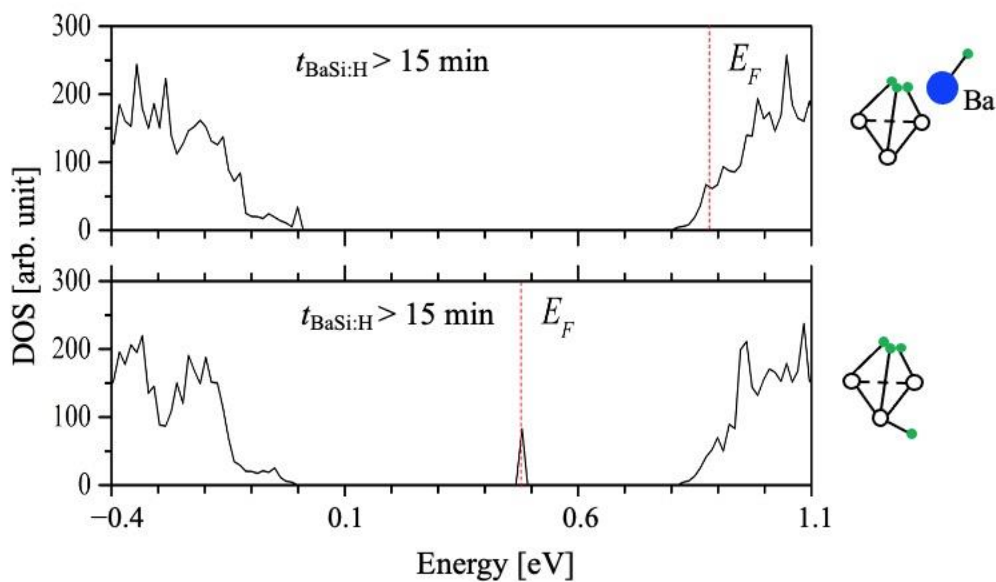

Fig. 3.11. Total density of states of an enlarged $BaSi_2$ unit cells with one H in different interstitial positions.

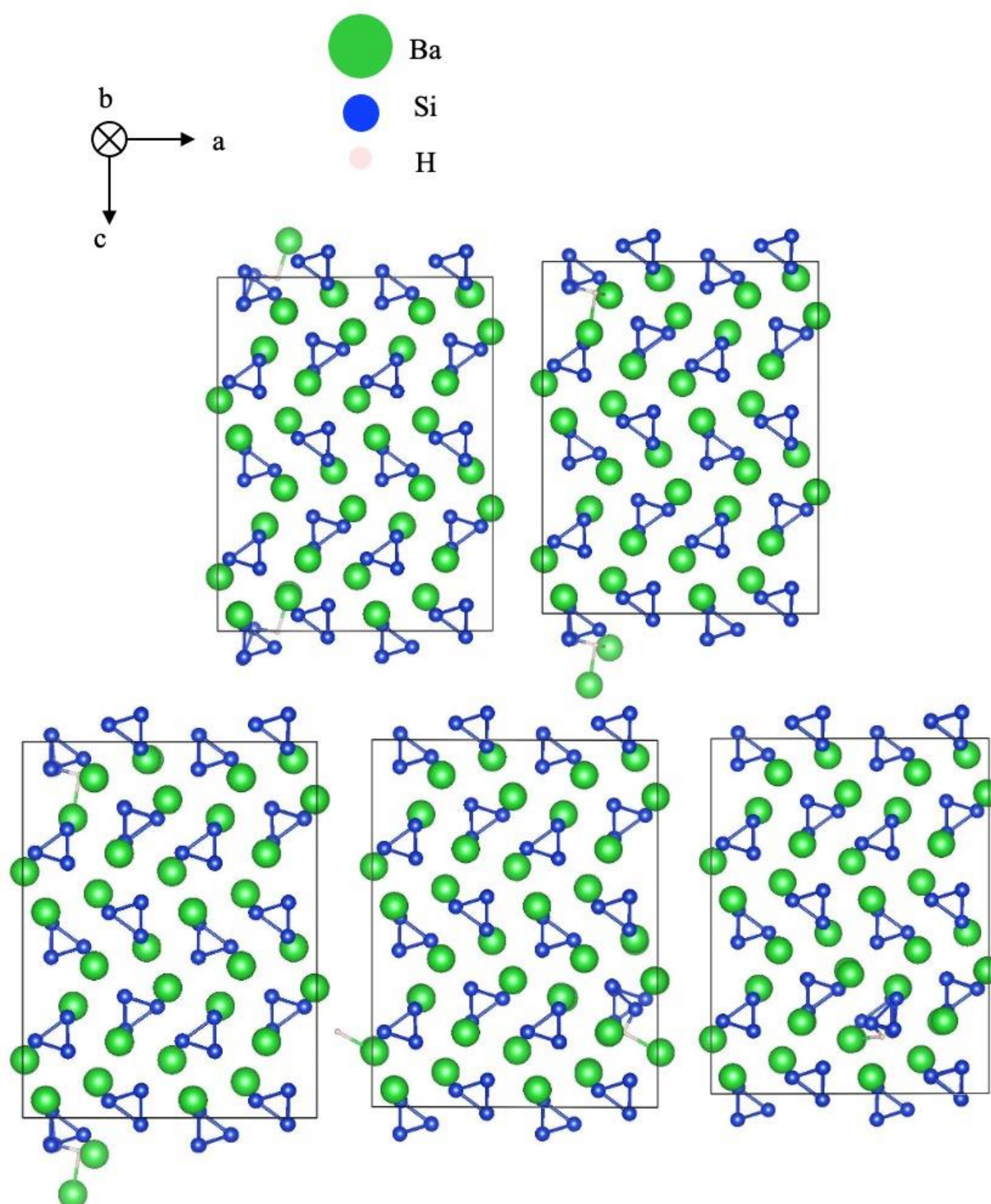

Fig. 3.12. Five models of one H in $BaSi_2$ with a V_{Si}.

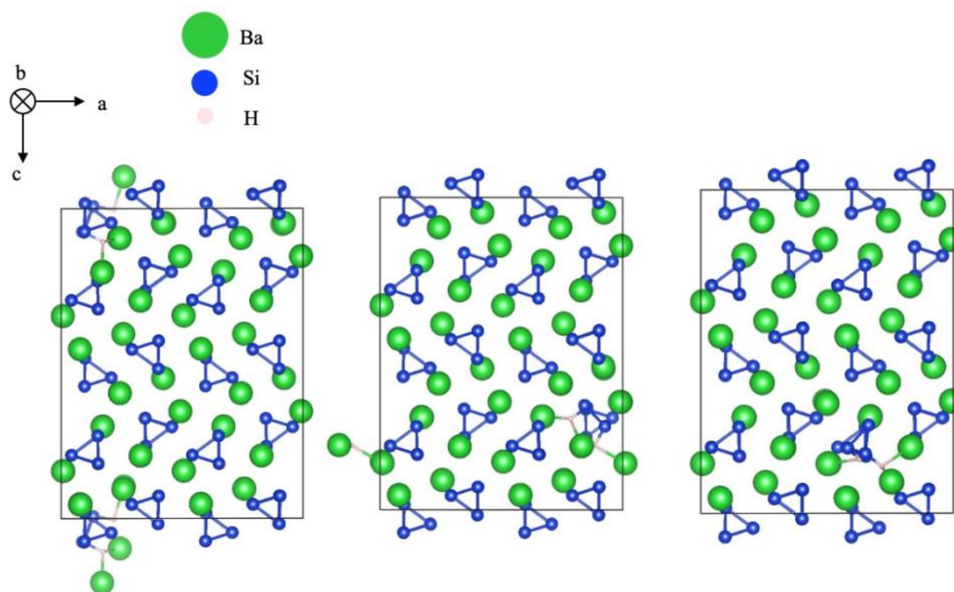

Fig. 3.13. Three models of two H in $BaSi_2$ with a V_{Si}.

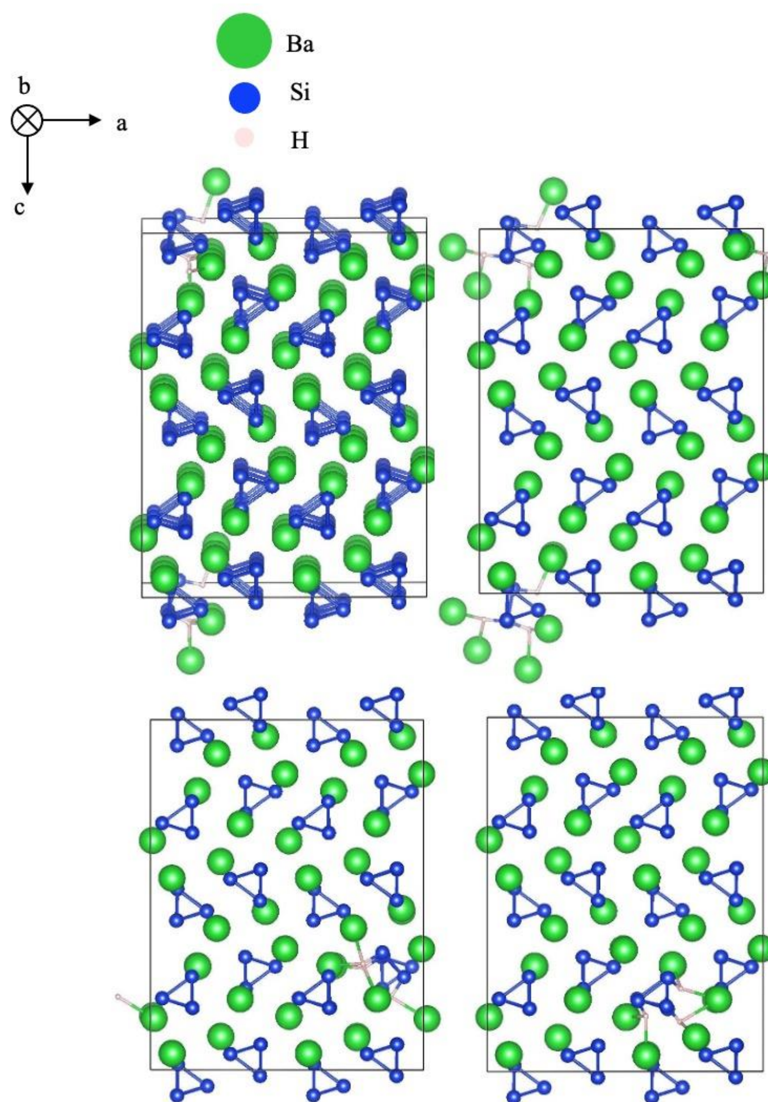

Fig. 3.14. Four models of three H in $BaSi_2$ with a V_{Si}.

3.4 Summary

First, we confirmed the optimal growth conditions of an a-Si:H passivation layer on $BaSi_2$. Based on the photoresponse spectra, $t_{a\text{-}Si:H}$ of 15 min and T_S of 180 ºC are found to be optimal. The results also indicated that the properties of a-Si:H are sensitive to the growth conditions. This is the first time for $BaSi_2$ films to be passivated using atomic H, and we obtained the highest photoresponsivity ever reported for $BaSi_2$. H atoms are considered to occupy V_{Si} and passivate point defects in $BaSi_2$. Our μ-PCD measurements confirmed that τ of $BaSi_2$ films is lengthened following H passivation. To explain this result, we employ various trap-related recombination mechanisms. In the initial stage, after the irradiation is stopped, the Auger recombination plays an important role and then the contribution of the phonon-assisted processes become more pronounced over time because of the decreases of the photogenerated carrier concentration and rate of Auger processes. The trap concentration is effectively reduced to 2.2×10^{12} cm^{-3} in the samples fabricated with $t_{BaSi:H} = 15$ min. This value is reduced by a factor of 30 comparing to that without H passivation. The trap concentration reduction is once again evaluated by the first-principle calculation, where the localized states are inactivated by H irradiation of 15 min.

3.5 Reference

1. S. Okasaka *et al.,* Surf. Sci. **635**, 115 (2015).
2. O. Kubo *et al.,* Jpn. J. Appl. Phys. **55**, 08NB11 (2016).
3. D. B. Migas *et al.,* Jpn. J. Appl. Phys. **56**, 05DA03 (2017).
4. J. I. Pankove *et al.,* Phys. Rev. Lett. **51**, 2224 (1983).
5. N. M. Johnson, Phys. Rev. B **31**, 5525 (R) (1985).
6. M. Stavola et al., Appl. Phys. Lett. **50**, 1086 (1987).
7. N. M. Johnson *et al.,* Phys. Rev. Lett. **56**, 769 (1986).
8. R. C. Chittick *et al.,* J. Electrochem. Soc. **116**, 77 (1969).
9. H. Sai *et al.,* Appl. Phys. Lett. **109**, 183506 (2016).
10. J. B. Nelson and D. P. Riley, Proc. Phys. Soc. **57**, 160 (1945).
11. G. Kresse and J. Hafner, Phys. Rev. B **49**, 14251 (1994).
12. G. Kresse and J. Furthmuller, Phys. Rev. B **54**, 11169 (1996).
13. G. Kresse and D. Joubert, Phys. Rev. B **59**, 1758 (1999).
14. J. P. Perdew *et al.,* Phys. Rev. Lett. **77**, 3865 (1996).
15. P. J. Mohr *et al.,* Rev. Mod. Phys. **84,** 1527 (2012).
16. N. Nakamura *et al.,* Jpn. J. Appl. Phys. **28**, 1762 (1989).
17. S. Sriaman *et al.,* Nature **418**, 62 (2002).
18. H. Fujiwara and M. Kondo, Appl. Phys. Lett. **90**, 013503 (2007).
19. H. J. Lin and S. H. Chen, Opt. Mater. Express **3**, 1215 (2013).
20. Z. Xu *et al.,* AIP Adv. **8**, 055306 (2018).
21. A. Hara, Jpn. J. Appl. Phys. **46**, 962 (2007).
22. S. M. Sze, *Physics of Semiconductor Devices*, 2nd ed. (Wiley, New York, 1981).
23. K. O. Hara *et al.,* Appl. Phys. Express **6**, 112302 (2013).
24. V. N. Abakumov, *et al.,* Nonradiative recombination of semiconductors, North Holland, 1991.
25. B.K. Ridley, Quantum Processes in Semiconductors, Clarendon Press, Oxford, 1982.
26. H. Peng *et al.,* Phys. Lett. A **374**, 3797 (2010).
27. H. Hoshida, *et al.,* Defect and Diffusion Forum **386**, 43 (2018).
28. K. Hashimoto *et al.,* J. Appl. Phys. **102**, 063703 (2007).

Chapter 4 H passivated p-$BaSi_2$, n-$BaSi_2$, and p-$BaSi_2$/n-Si heterojunction solar cells

4.1 H passivation p-$BaSi_2$

4.1.1 Introduction

In chapter 3, the photoresponsivity is improved significantly, and minority-carrier properties are upgraded as well because atomic H makes the localized states inactive. The basic structure of a solar cell is a *pn* junction; thus, passivation of impurity-doped p- or n-$BaSi_2$ films is of particular importance. Boron (B) is used as a p-type dopant for $BaSi_2$. B-doped p-$BaSi_2$ layers are grown by MBE on Si(111) substrates. The hole concentration is affected by T_S and the B crucible temperature (T_B) and varied from 10^{16} to 10^{18} cm^{-3} [1]. Recently, we found that lightly-B doped $BaSi_2$ films are more promising as a light absorbing layer than undoped one from the viewpoint of photoresponsivity [2]. On the other hand, antimony (Sb)-doped $BaSi_2$ is n-$BaSi_2$. The electron concentration can be controlled from 10^{16} to 10^{20} cm^{-3} by changing T_S [3]. Furthermore, Sb-doped $BaSi_2$ is more suitable to make electrical contacts to Al electrodes comparing to B-doped $BaSi_2$, because of a smaller contact resistance [4]. In this chapter, we first investigate the effect of atomic H passivation on the photoresponse properties of lightly and heavily B-doped p-$BaSi_2$ films by both experiment and theoretically calculation. Next, we discuss the effect of atomic H on the performance of B-doped p-$BaSi_2$/n-Si solar cells. Finally, the H passivated Sb-doped $BaSi_2$ is fabricated and characterized.

4.1.2 Experiment

1. Formation of atomic H-passivated p-$BaSi_2$ and p-$BaSi_2$/n-Si solar cells

Fabrication and subsequent H passivation of B-doped $BaSi_2$ films are accomplished using an ion-pumped MBE system equipped with standard Knudsen cells (K-cells) for Ba and B, and an EB gun for Si, and an RF plasma generator for atomic H. First, Ba, Si and B atoms are co-deposited on a low-ρ Cz n^+-Si(111) substrate at T_S = 600 ℃ to form an approximately 500-nm-thick B-doped $BaSi_2$ thin film. The T_B was set at 1100 ℃ and 1230 ℃ for lightly and heavily B doping, respectively, wherein the respective hole concentration are $p = 7 \times 10^{16}$ or 3×10^{18} cm^{-3} at RT. Hereafter, we refer to these as “lightly B-doped” and “heavily B-doped” samples, respectively. Second, the atomic H is supplied to the samples via a plasma generator for various values of $t_{BaSi:H}$ at T_S = 600 ℃. During an atomic H supply, the vacuum level is maintained at 10^{-3} Pa, the plasma power is set at 10 W, and the H concentration is around 10^{19} cm^{-3}. Finally, a 3-nm-thick a-Si layer is deposited as a capping layer. The samples are grown on the low-ρ substrates and high-ρ substrates for photoresponsivity measurements and μ-PCD measurements or Hall measurements by the van der Pauw method, respectively. Details of samples are summarized in Table IV. To study the effect of H passivation on the performance of B-doped p-$BaSi_2$/n-Si heterojunction solar cells, we formed 20-nm-thick B-doped p-$BaSi_2$ layers on medium-ρ n-Si(111) substrate (ρ = 1−4 Ωcm) at T_S = 600 ℃ and T_B = 1230 ℃. Then, atomic H is supplied for $t_{BaSi:H}$ = 14 or 32 s, followed by a 3-nm-thick a-Si capping layer, sample details are also shown in Table IV. Figure 4.1 shows fabrication procedure.

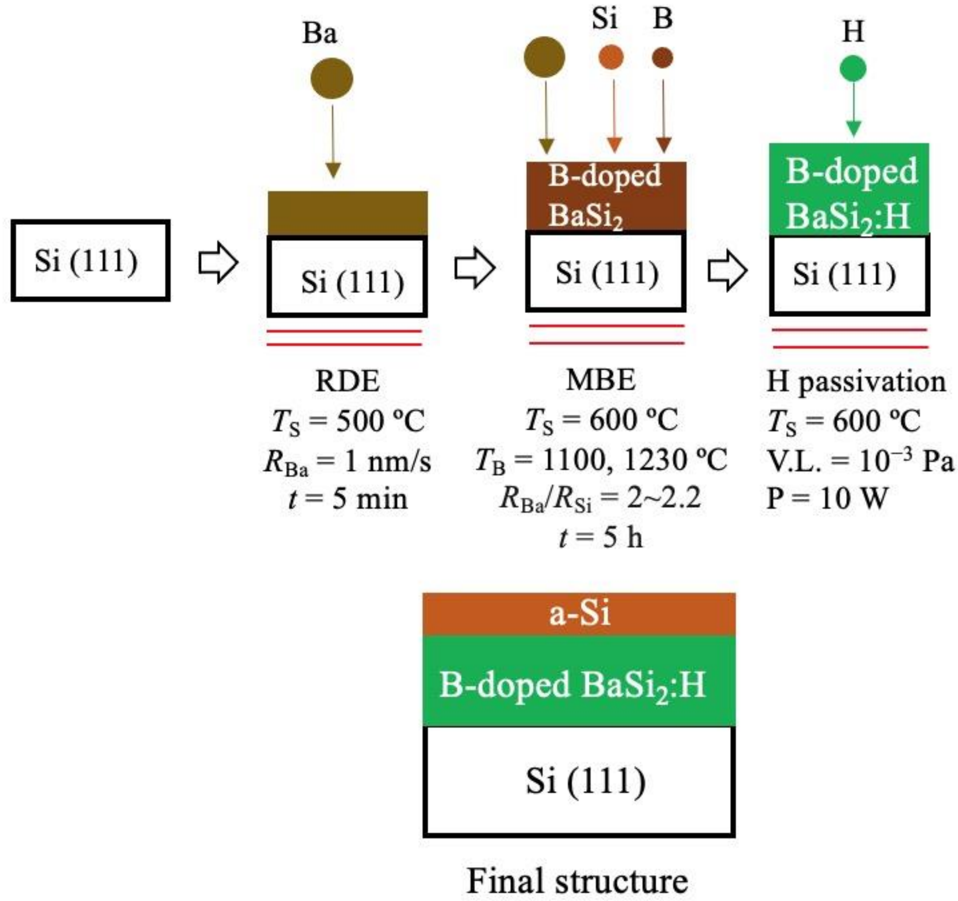

Fig. 4.1. Fabrication of H passivated B-doped $BaSi_2$.

For measurements of photoresponse and the *J*-*V* curves under AM 1.5 illumination, 80-nm-thick indium tin oxide (ITO) electrodes (1 mm diameter) are fabricated on the front surface of the samples and 150-nm-thick Al is deposited on the back surface of samples. Photoresponse spectra are measured by the same instruments as shown in chapter 3. The photoconduction is used to measure the photoresponsivity of $BaSi_2$ films. A bias voltage of 0.3 V is applied to the front ITO electrode with respect to the Al electrode to extract photogenerated electrons to the front ITO electrode. This represents a "forward" bias voltage for the p-$BaSi_2$/n-Si diodes. Although such forward bias voltages to pn diodes usually reduce photoresponsivity, there is no difference in photoresponsivity between both the forward and reverse bias voltage because the diodes do not display rectifying properties according to the *J*-*V* characteristics. The PL measurements are carried out at 8 K with an excitation laser wavelength of 442 nm and detected by a liquid nitrogen-cooled InP/InGaAs photomultiplier (Hamamatsu Photonics R5509-72, Japan) and amplified by a lock-in technique. Samples are excited from the $BaSi_2$ side. The τ is measured using a μ-PCD system (Kobelco, LTA-1512EP, Japan), while the DLTS measurement is carried out in the temperature range of 80−300 K using a 1MHz capacitance versus voltage (C-V) meter (HP 4280A.) The rate window is varied between 1 and 512 ms.

2. Calculation details

We also apply the same first-principles calculation method as mentioned in chapter 3 to estimate the influence of B doping and H incorporation on the electronic properties of $BaSi_2$, which is also used for full structural optimization. The energy cutoff is set at 400 eV.

TABLE IV. Structure, substrate, growth temperature (T_S), H supply duration ($t_{BaSi:H}$), and B crucible temperature (T_B) for the p-$BaSi_2$/n-Si solar cells.

Structure	Sample	T_S (ºC)	$t_{BaSi:H}$ (min)	T_B (ºC)
	reference	580	15	0
a-Si/B-doped $BaSi_2$:H/n^+-Si	1	600	0	1100
	2		5	
	3		10	
	4		15	
	5		0	1230
	6		1	
	7		5	
a-Si/B-doped $BaSi_2$:H/n-Si	8	600	0	1100
	9		5	
	10		10	
a-Si/B-doped $BaSi_2$:H (20nm)/n-Si	11	600	0	1230
	12		14	
	13		30	

4.1.3 Results and discussions

Figure 4.2(a) shows the photoresponse spectra of lightly B-doped p-$BaSi_2$ films from samples 1−4, where $t_{BaSi:H}$ is varied in the range of 0−15 min. As a reference, we introduce the spectrum of the highest photoresponsivity of undoped $BaSi_2$ films ($t_{BaSi:H}$ = 15 min). The photoresponsivity increased at $\lambda < 1000$ nm, corresponding to the E_g of $BaSi_2$. The photoresponsivity is proportional to the ratio of the τ to the carrier transit time. The photoresponsivity is used to represent the defect density because it affects the τ markedly. The smallest photoresponsivity is from sample 1, which is prepared without H passivation. The photoresponsivity of samples 2 and sample 3 increased significantly more than that of sample 1, and reached a maximum value of 4 A/W at $\lambda = 800$ nm. This is almost twice the highest value for reference sample which is the H passivated undoped $BaSi_2$. Comparing the photoresponse spectrum of sample 3 to that of sample 2, the photoresponsivity of sample 3 is smaller at shorter wavelengths at $\lambda < 500$ nm. This behavior is interpreted to originate from the surface damage induced by atomic H. We posit that the energetic H atoms from the plasma generator hitting the sample surface generated defects in the surface regions. These defects caused the photogenerated electrons to be more likely to recombine before being extracted to the ITO electrodes. The photoresponsivity of sample 4 exhibits further degradation, indicating that both the bulk and surface regions acquired defects. In the bulk region, the superabundant H atoms generate additional defects other than V_{Si} and the same phenomenon is previously reported in c-Si and undoped $BaSi_2$[5, 6]. Figure 4.2(b) shows the photoresponse spectra of heavily B-doped p-$BaSi_2$ films from samples 5−7, where $t_{BaSi:H}$ is varied in the range of 0−5 min. In contrast with samples 1−4, the photoresponsivity exhibits degradation with increasing $t_{BaSi:H}$, showing that H passivation is not suitable to improve the photoresponsivity of heavily B-doped $BaSi_2$ films. Note that the photoresponsivity of heavily B-doped $BaSi_2$ in sample 5 is higher than lightly B-doped $BaSi_2$ films in sample 1, meaning that the lightly B-doped $BaSi_2$ films contain more defects than heavily B-doped ones. Furthermore, we speculate that the excess B atoms may occupy the V_{Si} in heavily B-doped $BaSi_2$, which reduce or passivate V_{Si}. When atomic H is irradiated later to the heavily B-doped $BaSi_2$, there is less V_{Si} for H atoms occupation. Thus,

atomic H, itself, introduces defects and leads the degradation of photoresponsivity. This situation is similar to the case of the H passivated lightly B-doped $BaSi_2$ when $t_{BaSi:H}$ = 15 min, or the H passivated undoped $BaSi_2$ when $t_{BaSi:H}$ = 30 min.

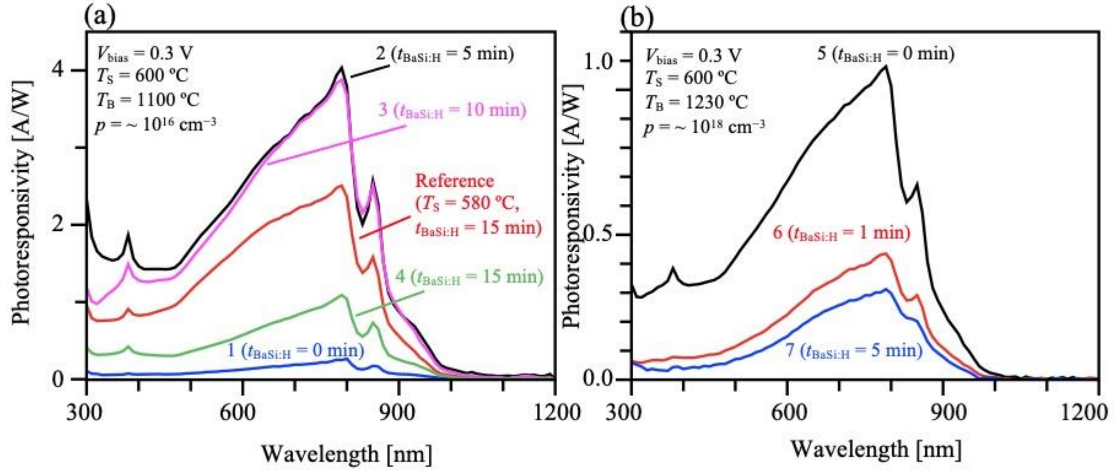

Fig. 4.2. (a) Photoresponsivity spectra of 500-nm-thick lightly B-doped $BaSi_2$ layers passivated by atomic H with various values of $t_{BaSi:H}$ in the range of 0−15 min. (b) heavily B-doped $BaSi_2$ layer passivated by atomic H with various values of $t_{BaSi:H}$ in the range of 0−5 min

The photoresponsivity spectra are largely affected by defects or localized states within the band gap of H passivated B-doped $BaSi_2$. Therefore, investigation of PL spectra is mandatory. The PL intensity is proportional to the ratio of the radiative recombination rate of photogenerated carriers to their total recombination rate. The PL offers a nondestructive and sensitive tool for defect studies in solar cell materials such as Si [7-9], Cu(In,Ga)Se_2. [10-12], III-V semiconductors [13, 14], CdTe [15, 16] and perovskites [17], and they provide information on the presence of localized states within the band gap. The PL spectra are measured at 8 K for lightly B-doped p-$BaSi_2$ films for samples 1, 2, and 4, as shown in Figs. 4.3(a)-(c), respectively. The results for heavily B-doped p-$BaSi_2$ films from samples 5 and 7 are in Figs. 4.3(d) and (e), respectively. As shown in Figs. 4.3(a) and (d), without H treatment, the lightly-B doped sample 1 has a much smaller PL intensity than the heavily B-doped sample 5. Comparing the photoresponsivity of sample 1 to that of sample 5, we can draw a conclusion that the nonradiative recombination rate due to defects is much higher in sample 1than in sample 5. This is because B atoms are expected to fill V_{Si} in $BaSi_2$ films, more V_{Si} might be passivated in sample 5. In samples 2 and 4, the measured spectra are well reproduced by three Gaussian curves with peaks located at P2, P3, and P4. In sample 4, the contribution of P2, which is associated with levels deeper than those responsible for P3 and P4, becomes dominant. From the viewpoint of the Shockley-Read-Hall recombination model [18], deeper levels such as these promote the recombination of photogenerated carriers. In this regard, the degradation of photoresponsivity in sample 4 compared with sample 2 is consistent with the PL results. Figures 4.3(d) and (e) show the PL spectra of heavily B-doped p-$BaSi_2$ films of samples 5 and 7, respectively. We note that P1, which is associated with deeper levels, is necessary to reproduce the measured PL spectra of sample 5 but not for sample 7. This deeper level promotes the photogenerated carriers recombination and reduces photoresponsivity tremendously. However the measured photoresponsivity in Fig. 4.2(b) has the opposite results where the photoresponsivity of sample 7 is much lower than that of sample 5. Thus, we have to speculate that nonradiative recombination processes, which cannot be detected via PL measurements, occur in the heavily B-doped p-$BaSi_2$ films with increasing $t_{BaSi:H}$.

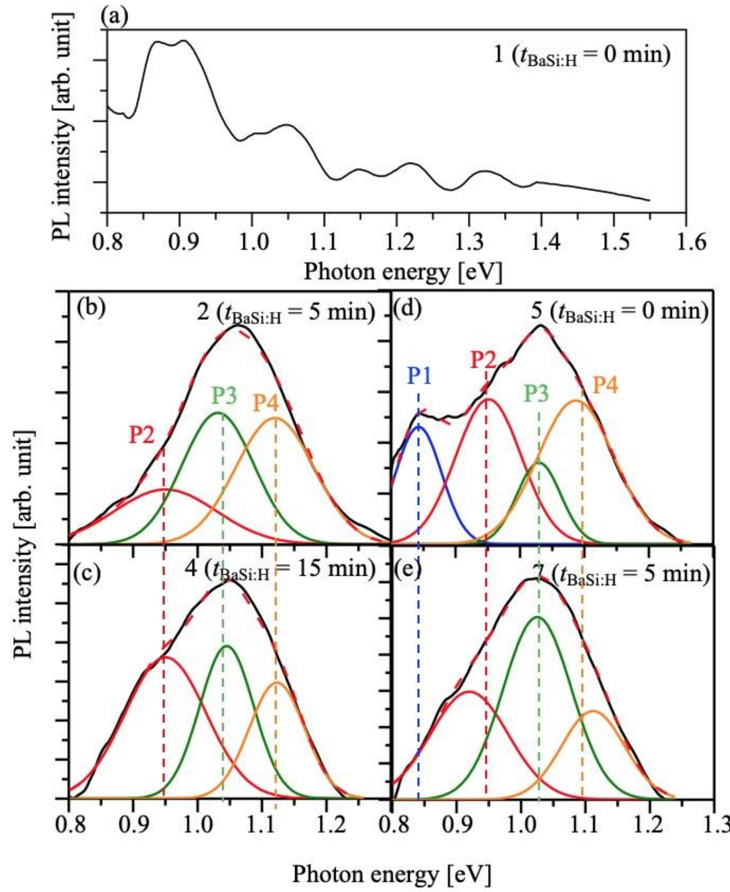

Fig. 4.3. PL spectra measured at 8 K for samples (a) 1, (b) 2, (c) 4, (d) 5, and (e) 7, fitted using Gaussian curves.

Figures 4.4(a) and (b) show the RT dependence of hole concentration and the hole mobility on $t_{BaSi:H}$ for the lightly and heavily B-doped p-$BaSi_2$ films, respectively. Due to B-H bond configuration, the hole concentration might be changed. In Fig. 4(a), the hole concentration of lightly B-doped p-$BaSi_2$ films is slightly increased from 7×10^{16} to 1×10^{17} cm^{-3} when $t_{BaSi:H}$ is lengthened from 0 to 10 min, and the mobility correspondingly decreased from 80 to 76 cm^2/Vs. A similar trend is observed in heavily B-doped p-$BaSi_2$, wherein the hole concentration slightly increased from 3×10^{18} to 7×10^{18} cm^{-3}, when $t_{BaSi:H}$ is lengthened from 0 to 5 min, and mobility decreased from 41 to 23 cm^2/Vs. The details of hole concentration variation is discussed by the calculation in the following part.

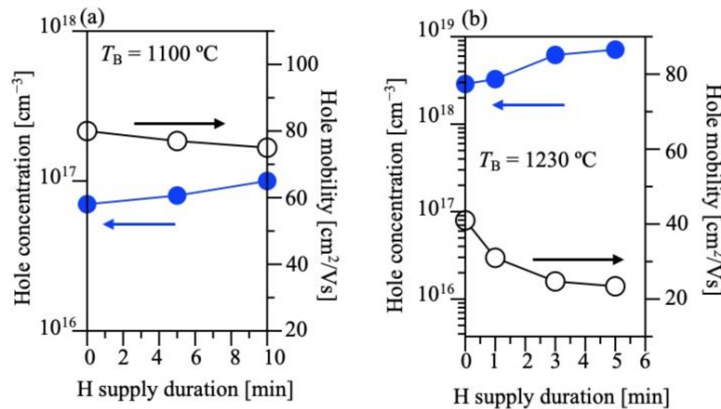

Fig. 4.4. Carrier concentration and mobility in H passivated (a) lightly B-doped $BaSi_2$ and (b) heavily B-doped $BaSi_2$, as function of $t_{BaSi:H}$.

We next study the τ of H passivated lightly B-doped $BaSi_2$ by the same μ-PCD system which was mentioned in chapter 3. The enhanced photoresponsivity is attributed to an increase in τ and/or a decrease in the carrier transit time. Hall measurement reveals that the mobility of H passivated lightly B-doped $BaSi_2$ does not exhibit a large change with increased $t_{BaSi:H}$. Therefore, an increase in τ is anticipated. Figure 4.5(a) shows the normalized photoconductance decay curves of samples 8−10 excited by a 5 ns pulsed laser intensity at λ = 349 nm. The laser light is absorbed within 60 nm from the top surface. The τ is calculated to be 0.13, 1.2, and 0.4 μs for samples 8-10, respectively. The τ is nine times larger than that of sample 8, signifying that the H passivation significantly improves the minority-carrier properties. We therefore assert that the increase in τ is the reason for the distinct photoresponsivity improvement in samples 2 and 3 in Fig. 4.2(a). Figure 4.5(b) shows the photoconductance decay curves of samples 8 and 10 where the λ of laser is 909 nm. Because of the much smaller α at λ = 909 nm than that at λ = 349 nm, most of the photons at this λ are absorbed in much deeper regions like in the c-Si substrate. The electron concentration in the n-Si substrate is approximate 10^{13} cm^{-3}. Unexpectedly, the τ of the Si substrate, which is governed by carrier recombination mainly at the $BaSi_2$/Si interface and Si back surface, improved from 12 μs in sample 8 to 25 μs in sample 10. This provides supporting evidence that atomic H-passivated defects are around the $BaSi_2$/Si interface. The detailed theoretical calculation is carried out to fit the τ of Fig. 4.5(a). The same model in chapter 3 is used to fit the experimental results showing in Fig. 4.6. Here, Auger recombination and phonon-assisted capture of carriers by traps are considered, which is described by Eq. (3) in chapter 3. The only free parameter of this model is the trap concentration. From the best fit of experimental data, the obtained trap concentration is found to be 7.5×10^{14}, 4.5×10^{13}, and 1.5×10^{14} cm^{-3} for the samples with $t_{BaSi:H}$ = 0, 5, and 10 min in lightly B-doped $BaSi_2$, respectively. The more pronounced decrease in photoconductivity for the samples with $t_{BaSi:H}$ = 0 and 10 min compared with the sample with $t_{BaSi:H}$ = 5 min is caused by the higher trap concentrations. It is interesting to compare the τ of H passivated undoped $BaSi_2$ with that of B-doped p-$BaSi_2$, where we have qualitatively the same situation for the photoconductance decay curve behavior of the $BaSi_2$ samples with $t_{BaSi:H}$ = 1, 15, and 30 min. Furthermore, the values of trap concentration are 6.5×10^{13}, 2.2×10^{12}, and 2.1×10^{13} cm^{-3}, respectively, and it is assumed that the trap centers could be associated with V_{Si} complexes only. It should be noted here that for lightly B-doped $BaSi_2$ films, the appropriate trap concentration is about one order of magnitude greater than those for the undoped $BaSi_2$. Accounting to the fact that the concentration of V_{Si} complexes does not exceed a value on the order of 10^{13} cm^{-3}, it can be expected that other types of defects contribute to the high concentration of trap centers. Analyzing the hole mobility versus temperature in B-doped $BaSi_2$ [19], it is shown that the presence of a high concentration of neutral defects is mainly from interstitial B atoms and is a characteristic feature of the studied samples. Thus, we assume that such B interstitial atoms and H interstitial atoms are associated with the trap centers in B-doped $BaSi_2$.

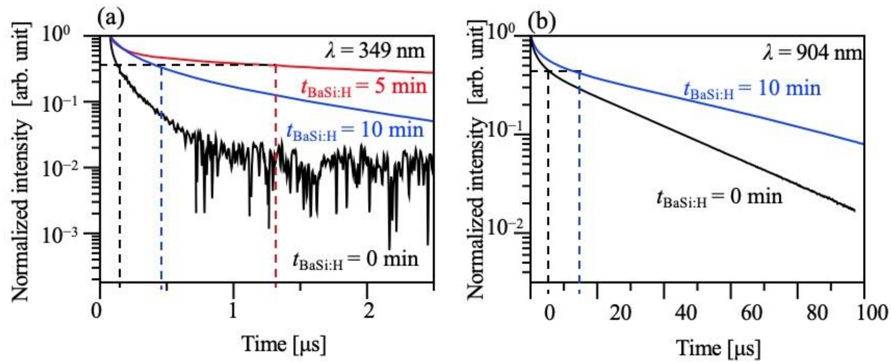

Fig. 4.5. Photoconductance decay curves of atomic H passivated lightly B-doped $BaSi_2$ with different $t_{BaSi:H}$ with laser wavelength of (a) 349 nm and (b) 904 nm.

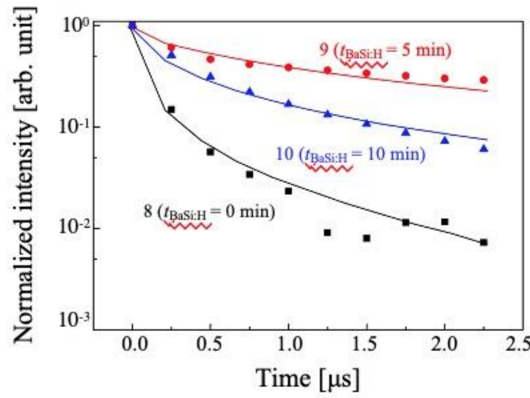

Fig. 4.6. Normalized photoconductivity of samples B-doped $BaSi_2$ versus time t after excitation was discontinued.

To get more insight into defect levels with and without H treatment, we next performed *ab initio* modeling of various B-doped $BaSi_2$ structures with possible incorporated H atoms. In B-doped p-$BaSi_2$, there are two different sites for B atoms including the interstitial and substitutional sites, which are considered to co-exist in the B-doped $BaSi_2$. When a B atom is a substitutional impurity, degenerate p-type semiconductor properties occur regardless of the nonequivalent Si(3)-Si(5) positions occupied by a B atom. This happens because the Fermi level crosses some bands at the top of the valence band, and a B atom has three valence electrons while a Si atom has four, leading to a lower number of valence electrons in the system. As a consequence, this leads to a shift of Fermi level to lower energies. Figures 4.7(a)-(c) shows the DOS of B occupying Si(3)-Si(5) sites. As the B concentration is so high in the calculation, which is more than 10^{20} cm^{-3}, the "degenerated" p-type forms. However, if a H atom is directly bonded to a B atom at a substitutional site or bonded to any Si in the tetrahedron with a B atom, the Fermi level shifts to the gap, indicating that the semiconducting properties are no longer degenerated as shown in Figs. 4.7(a')-(c'), with no states in the band gap region. Here, a H atom acts as a donor to provide one electron to a tetrahedron with a B atom. This is the reason of the same DOS and is independent of the Si-H or B-H bonds. In the case of a B atom acting as an interstitial impurity, we find that three possible sites that differ in the number of the first nearest neighbors to the B atom and their corresponding interatomic distances as shown in Fig. 4.8. For the first site as shown in Fig. 4.8(a), one partly occupied localized state and one filled localized state in the band gap region are present in the corresponding DOS. For the second site as shown in Fig. 4.8(b), one half filled localized state and one empty localized state can be observed in the band gap region. Finally, for the third site as shown in Fig. 4.8(c), degenerate n-semiconductor properties occur. When H is directly bonded to a B atom in any interstitial site, one filled localized state appears in the band gap. This means that the localized states are occupied by electron and thus inactivated. The minority carrier or photogenerated carrier properties are no longer affected by these localized states. Therefore, one H atom make the localized states inactive.

Next, we consider the two H atoms in both B interstitial and substitutional sites. When two H atoms are connected to a tetrahedron with a B atom, the localized state is clearly seen below the bottom of the conduction band as shown in Fig. 4.9(a). For two interstitial H atoms are shown in Figs. 4.9(b)-(d). The partly occupied states are evident and can serve as traps. It should be noted here that it is not necessary for all H atoms to be directly connected to an interstitial B atom, because, H atoms can form bonds with Si atoms in a tetrahedron close to the interstitial impurity without qualitative changes in the sharp of the DOS with respect to the cases when only B-H bonds are present. Now, we consider to link the structural changes and electric properties of light B-doped p-$BaSi_2$. The structure of sample 1 without H treatment, which contains states in the band gap

according to our photoresponse and PL measurement, can be characterized by the cases represented in Figs. 4.7(a)-(c) and Figs. 4.8(a)-(c), which also causes a relatively high trap concentration. As the incorporated H concentration is increased, the structure of sample 2 fabricated with $t_{BaSi:H} = 5$ min may be defined mainly by the cases represented in Figs. 4.7(a')-(c') and Figs. 4.8(a')-(c'). This, in turn, leads to a maximal passivation of lightly B-doped $BaSi_2$ and a considerable decrease in the trap concentration because of the appearance of completely filled states that can no longer be viewed as traps. It should be noted that only one H atom is needed to make the localized states inactive in lightly B-doped p-$BaSi_2$, in contrast to the presence of two H atoms for undoped $BaSi_2$. Finally, when the H concentration is further increased, as for sample 4 fabricated with $t_{BaSi:H} =$ 15 min, the structure is characterized by the cases represented in Fig. 4.9, where two H atoms increase the trap concentration. In addition, the excess of H atoms also gives rise to the localized states in the band gap region. This phenomenon will be discussed in the next chapter. Thus, H incorporation up to a certain concentration more efficiently neutralizes traps caused by B atoms.

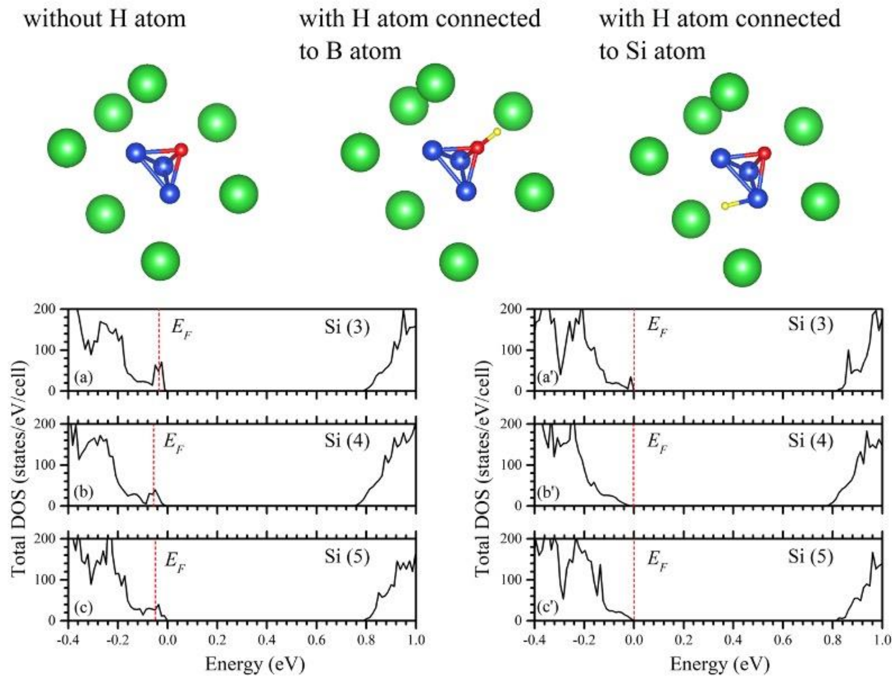

Fig. 4.7. Total density of states of $BaSi_2$ doped with B as a substitutional impurity in different Si site (a-c) without and (a'-c') with H incorporation.

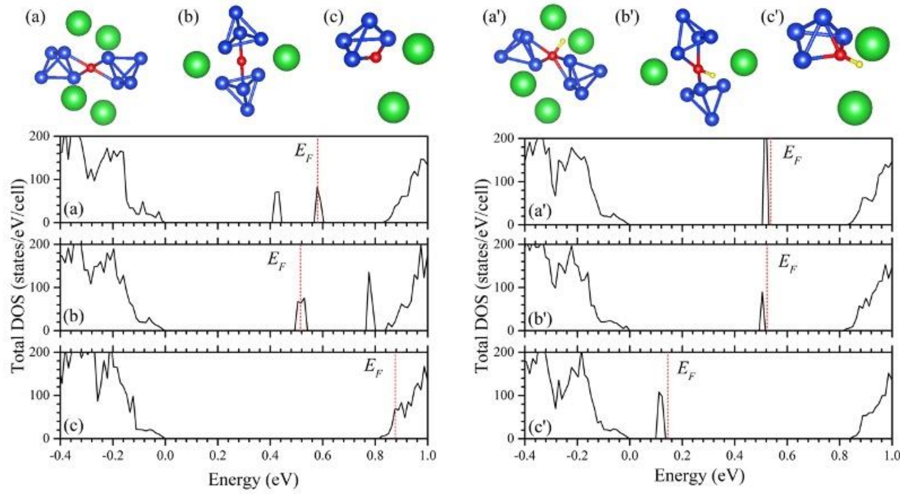

Fig. 4.8. Total density of states of $BaSi_2$ doped with B as a interstitial impurity in different site (a-c) without and (a'-c') with H incorporation.

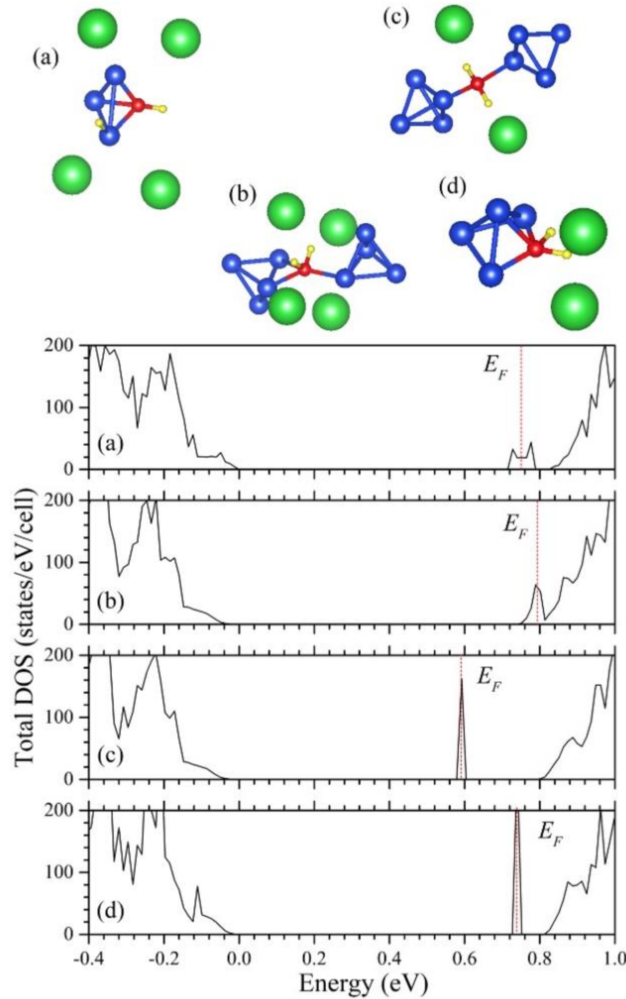

Fig. 4.9. Total density of states of $BaSi_2$ doped with B (a) as a substitutional impurity with two H atoms bonded to a tetrahedron with the B atom and (b)-(d) as an interstitial impurity with two H atoms bonded to the B atom.

Finally, the H passivated heavily B-doped $BaSi_2$ is calculated. In the case of lightly B-doped $BaSi_2$ samples with a trap concentration of about 10^{14} cm^{-3}, the theoretical calculation could reasonably well explain

experimentally observed trends in simulations, which could not be less than 10^{20} cm^{-3}. Therefore, to explain the photoresponsivity reduction in the H passivated heavily B-doped $BaSi_2$, the other structural models are required involving the presence of a direct B-B bonding and/or two B atoms connect to the same Si tetrahedron. Surprisingly, a comparison of the total energy of cases with two interstitial B atoms directly bonded to each other or to the same Si tetrahedron indicated not only comparable values but even lower ones compared with the cases when two interstitial B atoms are far apart in the enlarged unit cell. Here, the excess B atoms lead to the formation of more complex defects: one B atom moves toward a neighboring Si tetrahedron and acts as a bridging atom between two Si atoms from different tetrahedra causing one Si-Si bond to be broken in the neighboring tetrahedra. Two models are shown in Fig. 4.10(a) and Fig. 4.11(a). As a results, a lot of localized states appear in the band gap region according to the corresponding DOS. One additional H atom increases the trap concentration if two interstitial B atoms are directly bonded which is shown in Fig. 4.10(b), regardless of Si-H or B-H bond formation, except for the case when the bridge configuration is broken by H atoms and n-type degenerate properties occur without states in the E_g, which is shown in Fig. 4.10(c). For the case of Fig. 4.11(a), one H atom is not capable of neutralizing multiple states in the band gap region, which are shown in Fig. 4.11(b)-(e). After that, we have also check the cases with one substitutional and one interstitial B atoms located in/at the same Si tetrahedron. In terms of formation energy, all such cases are energetically preferable with respect to the ones with two interstitial B atoms. In addition, the presence of B-B bonding is also found to be energetically favorable in any defect configuration. If two B atoms including one substitutional and one interstitial are connected to each other which is shown in Fig. 4.12(a), no states are observed in the band gap region. If one H atom is added in this model, H provides a half-occupied state (Fig. 4.12(b)) or generates n-type degenerated semiconductor (Fig. 4.12(c)). To this end, the key issue of the heavily B-doped $BaSi_2$ samples is the appearance of the complex defect with two B atoms where in the most cases an addition of one H atom increases the trap concentration and, as a consequence, affects the photoresponsivity. We cannot exclude the possibility that a sizable amount of H atoms eventually neutralize these defects. However, considering that H atoms also act as interstitial defects, such huge amount of H could worsen the situation. In the enlarged unit cell used for calculations herein, only one type of defects can be treated at once because of serious limitations on the size of the considered systems. However, localized states with very low dispersion appear in the band gap region, indicating that the defect-defect interaction is sizably attenuated. At the same time, in the direct space, everything is localized within the area of a defect. The latter fact in addition to the obtained n-type degenerate semiconducting properties does not mean that a change in conductivity because in real B-doped $BaSi_2$ samples always various types of defects occur and the properties on the whole are defined by the defects with the largest concentrations. Since our heavily B-doped $BaSi_2$ samples do not show changes in the conductivity type, we can conclude that the defects responsible for n-type degenerate semiconducting properties do not dominate.

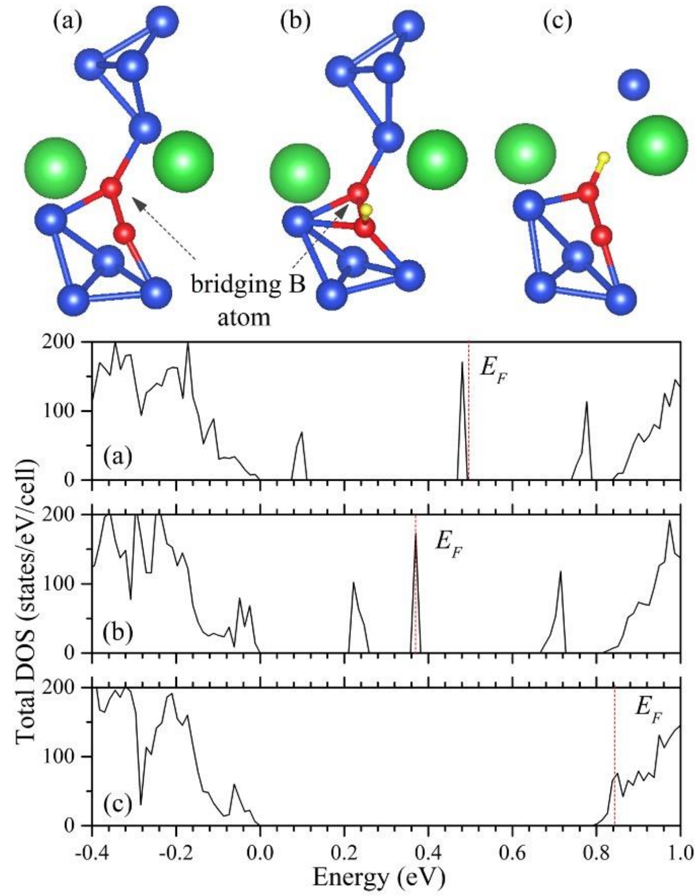

Fig. 10. Total density of states of $BaSi_2$ doped with two interstitial B connected to each other (a) without H passivation and (b)-(c) with H passivation.

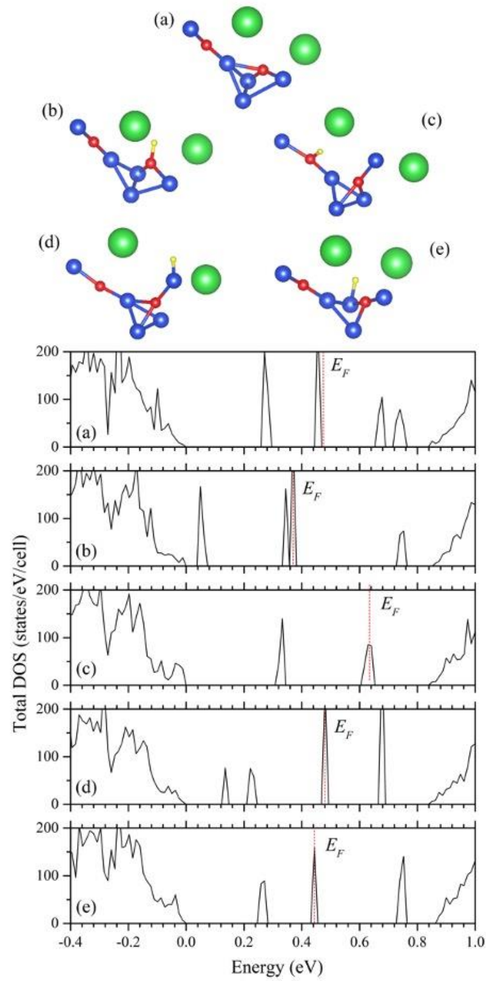

Fig. 11. Total density of states of $BaSi_2$ doped with two interstitial B connected to the Si tetrahedron (a) without H passivation and (b)-(e) with H passivation.

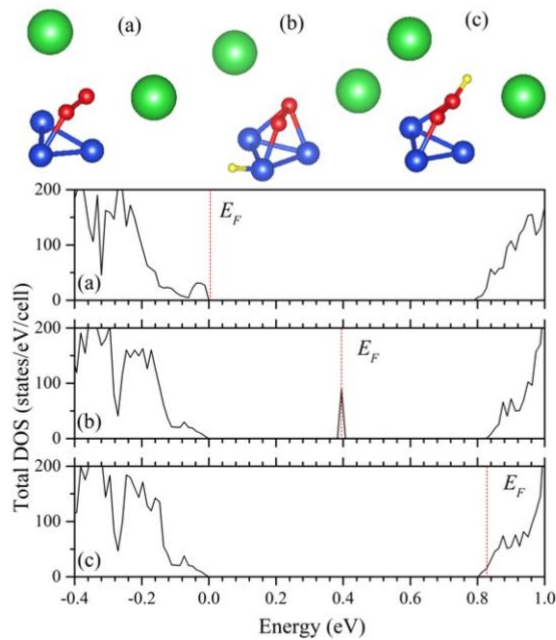

Fig. 12. Total density of states of $BaSi_2$ doped with two B substitutional and interstitial atoms connected to each other (a) without H passivation and (b)-(c) with H passivation.

Because heavily B-doped p-$BaSi_2$ films are used in the p-$BaSi_2$/n-Si solar cells, we shorten the $t_{BaSi:H}$ from the optimum value for the lightly-B doped $BaSi_2$ films for the following reasons. As shown in Fig. 4.2(b) and the above discussions, the atomic H supply decreases the photoresponsivity of heavily B-doped p-$BaSi_2$ films. However, atomic H may passivate defects around the $BaSi_2$/Si interface from the result shown in Fig. 4.5(b). We, therefore, adopted $t_{BaSi:H}$ as 0, 14, and 30 s. Figure 4.13(a) shows the *J-V* curves of these solar cells under AM 1.5 illumination. The short-circuit current density (J_{SC}), open circuit voltage (V_{OC}), fill factor (FF) and η, all improved after H passivation. To accurately determine the reverse saturation current density (J_0), the series resistance (R_S), and the shunt resistance (R_{SH}), we adopted a technique described by Sites and Mauk [20]. Using the photodiode equation, the relationship between R_S and R_{SH} can be given as

$$\frac{dV}{dJ} = SR_s + \frac{\gamma k_B T}{q}\left[\frac{1 - (SR_{SH})^{-1} - \frac{dV}{dJ}}{J + J_{SC} - (SR_{SH})^{-1}V}\right]. \quad (4.1)$$

Where S is the area of the electrode, γ is the ideality factor, k_B is the Boltzmann constant, T is the absolute temperature, and q is the elemental charge. The solar cell parameters obtained are summarized in Table V. The η improved from 2.59% in sample 11 to a stable value of 6.2% in samples 12 and 13, showing that the η almost leveled off. Thus, further increasing $t_{BaSi:H}$ might degrade the solar cell performance. J_0 can be used as a measure to represent the quality of the p-$BaSi_2$/n-Si heterointerface, where a lower J_0 value indicates increased quality. The J_0 values of samples 12 and 13 are more than three orders of magnitude lower than that of sample 11. In other words, the defects around the heterointerface decrease markedly with H passivation. This results shows even though no defect passivation is expected in the bulk region of the heavily B-doped $BaSi_2$ films on H treatment, improvements could be observed for the solar cell performance due to interface passivation. While the obtained η is not higher than the highest reported values, the effects of atomic H passivation are clearly demonstrated. Other factors, such as growth chamber conditions, that can degrade η require further investigation.

TABLE V. Solar cell parameters of samples 11−13. Short-circuit density (J_{SC}), open-voltage (V_{OC}), fill factor (FF), conversion efficiency (η), series resistance (R_S), shunt resistance (R_{SH}), and reverse current density (J_0) are all summarized.

Sample	J_{SC} (mA/cm^2)	V_{OC} (V)	FF	η (%)	R_S (Ω)	R_{SH} (kΩ)	J_0 (mA/cm^2)
11	22	0.28	0.44	2.59	127	5.2	6.24×10^{-4}
12	27	0.40	0.63	6.20	92	22.3	4.42×10^{-7}
13	27	0.40	0.64	6.19	76	19.8	1.31×10^{-7}

To study the defect densities and their levels in p-$BaSi_2$/n-Si heterointerface, we performed DLTS measurements on samples 11 and 12 [21]. Figure 4.13(b) shows a schematic diagram of the DLTS procedure, where a forward filling pulse voltage (V_P) disturbs the steady-state reverse-bias condition. This causes the electric field in the depletion region to decrease, thereby recharging the defect levels. When the voltage returns to its steady-state value, the defect levels begin to discharge by emitting trapped carries by thermal emission, and the resultant time evolution of the capacitance change ΔC is measured for various rate windows. Here, V_P is set at 0.5 V, the pulse width (t_{PW}) at 50 ms, and the reverse bias voltage (V_R) at −0.1 V and −0.5 V. Because of a large difference in carrier concentration between p-$BaSi_2$ ($p > 10^{18}$ cm^{-3}) and n-Si (n » 10^{15} cm^{-3}), the depletion region stretched toward the n-Si side. Therefore, defects in the n-Si side are detected. Figure 4.13(c) shows the DLTS profiles obtained for samples 11 and 12. A dip caused by a majority carrier (electron) trap is observed at around 100 K in sample 11. On increasing the magnitude of V_R from 0.1 to 0.5 V, the signal

intensity decreased. This indicates that the defects are present around the p-$BaSi_2$/n-Si interface. From the Arrhenius plot shown in Fig. 4.13(d), the electron trap level is calculated to be approximately 0.22 eV from the conduction band minimum, and the defect density is 1×10^{14} cm^{-3}. In contrast, no distinct peak is observed in sample 12, demonstrating that the defects in sample 11 are passivated by atomic H. The DLTS results are consistent with the improvement of the *J-V* curve shown in Fig. 4.13(a). Because of the significant reduction of interface defects, J_0 values of samples 12 and 13 are approximately three orders of magnitude lower than that of sample 11. These DLTS results provide direct evidence that H irradiation is an effective means to improve solar cell performance by reducing interface defects. This discovery can be used in the near future to passivate interface defects in $BaSi_2$ homojunction solar cells.

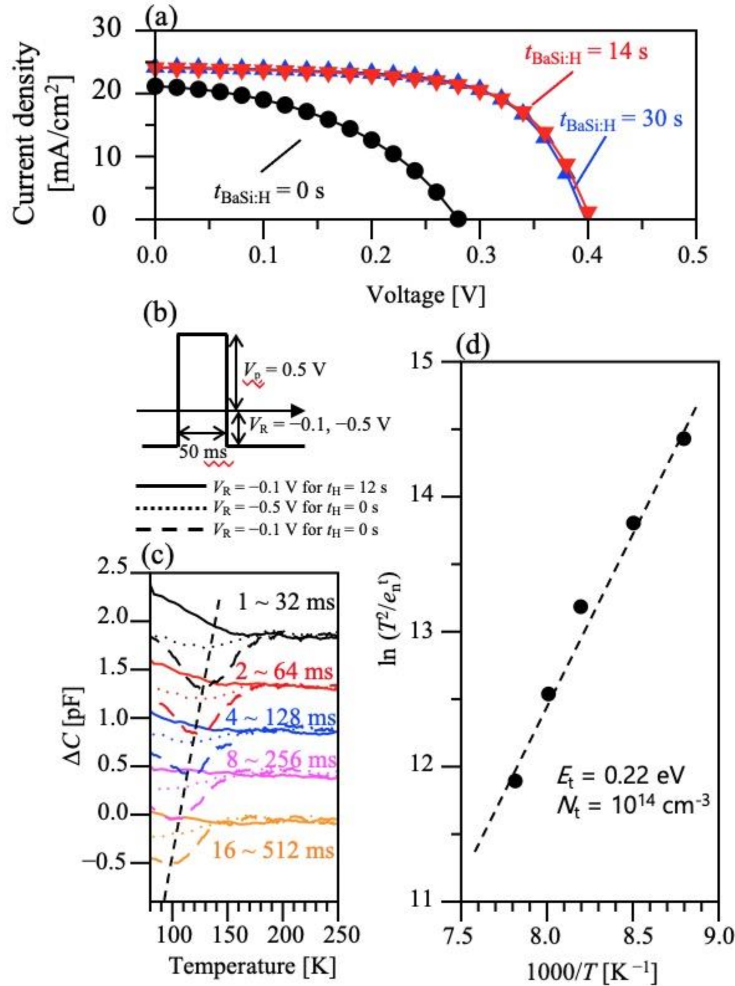

Fig. 4.13. (a) *J-V* curve of B-doped p-$BaSi_2$/n-Si solar cells without/with H passivation. (b) Schematic diagram of the DLTS procedure. (c) DLTS profiles of samples 11 and 12 at $V_P = 0.5$ V, t_{pw} =50 ms, and $V_R = -0.1$ V and −0.5 V. The rate window was varied as 1−32, 2−62, 4−128, 8−256, and 16−512 ms. (d) Arrhenius plot for the electron trap level.

4.1.4 Summary

This investigation clearly shows that in general the photoresponsivity of B-doped $BaSi_2$ can be significantly improved via H incorporation. An atomic H supply for $t_{BaSi:H}$ = 5−10 min for lightly B-doped p-$BaSi_2$ films could enhance the photoresponsivity by up to an order of magnitude, while this is not the case for heavily B-doped p-$BaSi_2$ films. The enhancement is caused by the increase in the minority-carrier lifetime, as measured

by μ-PCD. However, further atomic H supply (> 15 min) leads to significant degradation of photoresponsivity. An analysis of the experimental data shows that the overall photoresponsivity and minority-carrier lifetime behavior could be explained in terms of various Auger processes. From the theoretical analysis, it could be concluded that (i) the trap concentration of lightly B-doped $BaSi_2$ is about one order of magnitude higher than that for the undoped $BaSi_2$ samples, which is in good agreement with the experimentally estimated value; (ii) the trap centers, should be associated with interstitial B atoms; (iii) for the lightly B-doped $BaSi_2$, a lower amount of H is needed to passivate these centers, compared with undoped $BaSi_2$; and (iv) the trap concentration of heavily B-doped $BaSi_2$ is in the order of 10^{15} cm^{-3} or even higher, with interstitial B atoms tending to cluster. To understand this degradation, *ab initio* modeling is performed for various B-doped $BaSi_2$ structures with incorporated H atoms; the results indicated that a delicate balance exists between H as saturation species to eliminate trap states in the band gap region originating from an interstitial B impurity and H works as an interstitial itself in $BaSi_2$ that leads to trap formation. We also investigated the effect of atomic H incorporation on their performance of B-doped p-$BaSi_2$/n-Si heterojunction solar cells, where an atomic H supply significantly decreased the reverse saturation current density and improved the conversion efficiency up to 6.2%. The reduction of defect density via atomic H supply is demonstrated via DLTS measurements.

4.2 H passivated n-$BaSi_2$

4.2.1 Experiment

1. Formation of atomic H-passivated Sb-doped n-$BaSi_2$

We use an ion-pumped MBE system equipped with standard K-cells for Ba and Sb, and an EB gun for Si, and a RF plasma generator for atomic H. First, Ba, Si and Sb atoms are co-deposited on a medium-ρ Cz p-Si(111) substrate (ρ = 1−4 Ωcm) at T_S = 525 ℃ to form an approximately 300-nm-thick Sb-doped $BaSi_2$ thin film. The crucible temperature of Sb was T_{Sb} = 300 ℃ wherein the electron concentration is $n = 5.4 \times 10^{19}$ cm^{-3}at RT. In general, only 20-nm-thick Sb-doped $BaSi_2$ works as an n-type layer in $BaSi_2$ homojunction solar cell because Sb is very easy to diffuse into the Si substrate or other $BaSi_2$ layer [22]. Thus, it is very important to study the electron concentration variation of H passivated Sb-doped $BaSi_2$, instead of obtaining a high photoresponsivity of H passivated Sb-doped $BaSi_2$. Second, the atomic H is supplied to the samples via an RF plasma generator for various values of $t_{BaSi:H}$ at T_S = 525 ℃. During the atomic H supply, the vacuum level is maintained at 10^{-3} Pa, the plasma power is set at 10 W. Finally, 3-nm-thick a-Si is deposited as a capping layer. The samples are also grown on high-ρ p-Si substrates for Hall measurements by the van der Pauw method. Figure 4.14 shows the fabrication procedure.

The photoresponse spectra and the *J*-*V* curves under AM 1.5 illumination are measured. For this purpose, 80-nm-thick indium tin oxide (ITO) electrodes (1 mm diameter) are fabricated on the front surface of the samples and 150-nm-thick Al is deposit on the back surface of samples. Because of p-Si substrate, there is a built-in field at the interface of Sb-doped $BaSi_2$/p-Si and the diodes display rectifying properties according to the dark *J*-*V* characteristics Thus, the bias voltage is set at 0 V.

2. Calculation details

We apply the self-consistent field (SCF) method to optimize the structure and calculate DOS of unit cell of Sb-doped $BaSi_2$ with and without H incorporation by quantum espresso (QE) code [23, 24]. The generalized gradient approximation of Perdew-Burke-Ernzerhof is used for the exchange and correlation potentials. The cut-off energy of the plane-wave basis sets is 40 Ry. For *k* points in the Brillouin zone, a $3 \times 4 \times 2$ Monkhorst-pack mesh is used for a perfect crystal. The estimated energy error in SCF is less than 10^{-8} a.u. Relaxation is performed until the total energy changed by less than 10^{-5} a.u., and the components of forces are smaller than 10^{-5} a.u. during geometry optimization.

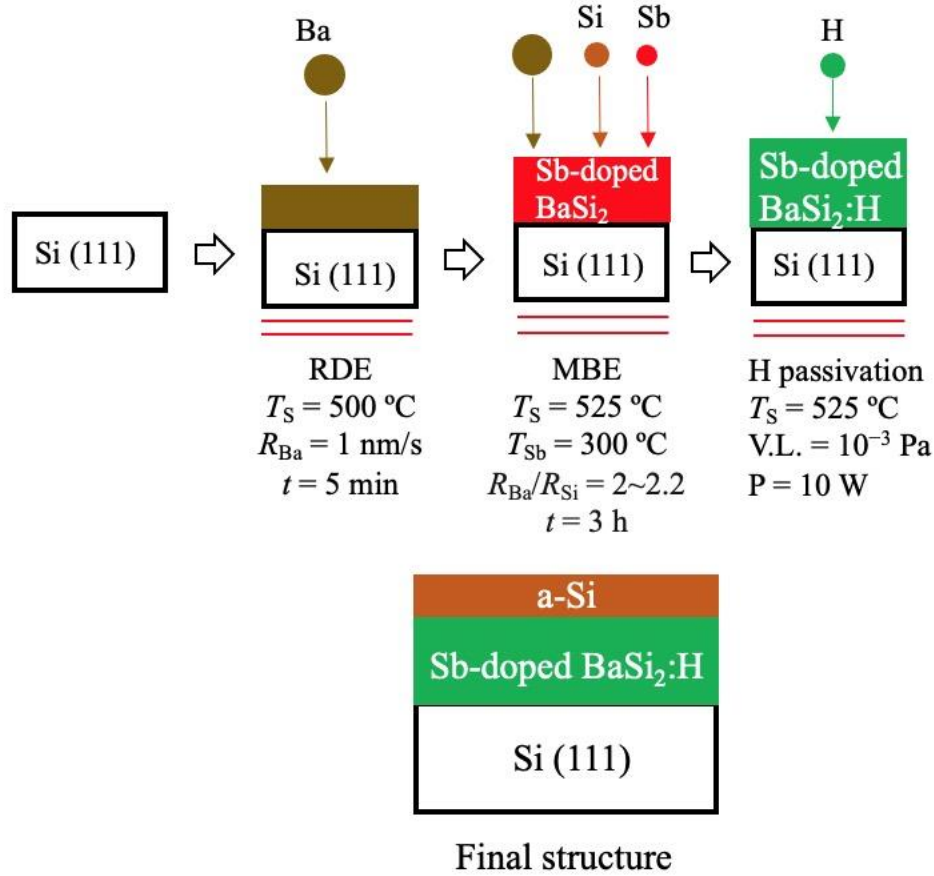

Fig. 4.14. Fabrication of H passivated Sb-doped n-$BaSi_2$.

4.2.2 Results and discussions

Figure 4.15 shows the $t_{BaSi:H}$ dependences of electron concentration and mobility of H passivated Sb-doped $BaSi_2$. The electron concentration of as-grown sample is 5.4 × 10^{19} cm^{-3}, and the mobility is 6700 cm^2/Vs. When we irradiate atomic H to Sb-doped $BaSi_2$, the electron concentration is reduced by three orders of magnitude down to approximate 10^{16} cm^{-3}, and keeps this value for further increase of $t_{BaSi:H}$, while the mobility is increased. However, the measured mobilities of electron in these samples are incredibly high in spite of various scattering mechanisms [19]. Therefore the further investigation on the measured high mobility is necessary. We also calculate DOS of H passivated Sb-doped $BaSi_2$. Figure 4.16(a) shows Sb-doped $BaSi_2$ without H incorporation. Sb atom is located at a Si(3) sites [25]. The Fermi level is in the conduction band indicating that Sb-doped $BaSi_2$ is n^+-type semiconductor. Please note that in the model of calculation one Sb atom exists in the unit cell, meaning the state of quite heavy doping. This is the reason why the degenerated n-type $BaSi_2$ forms. Three valance electrons from an Sb atom form covalent bonds with three Si atoms in a Si tetrahedron, one electron from the Sb atom and one electron from a Ba atom form a lone pair electron. This is an ionic bonding between positively charged Ba atoms and negatively charged Si tetrahedral. One remaining electron of the Sb atom works as a majority carrier (conductive electrons). When we add one atomic H to Sb-doped $BaSi_2$, as shown in Fig. 4.16(b), the H atom attaches one Si atom in the Si tetrahedron. The Fermi level goes to lower energy and electron concentration is reduced. This is because the one remaining electron is terminated by one electron from the H atom and is similar to the intrinsic semiconductor. If two H atoms, the second H atom links with other Si atom in Si tetrahedron. The localized states appeared in the band gap region and degrade the minority carrier properties meaning that the excess H atom introduces trap centers.

Figure 4.17(a) shows the *J*-*V* curves of samples with $t_{BaSi:H}$ of 1, 3 and 5 min under AM 1.5 illumination.

The electron concentration is in the range of 10^{16} cm^{-3}. The J_{SC}, V_{OC}, and η, all improved with $t_{BaSi:H}$ enlarging, although the η is low. Other parameters such as R_S, R_{SH}, FF, J_0 are fitted by Eq. (4.1) and summarized in Table VI. The J_0 is much larger than that of p-$BaSi_2$/n-Si heterojunctions, meaning that the more defects exist at the heterointerface of n-$BaSi_2$/p-Si. With H passivation, the J_0 is decreased because H atoms diffuse and passivate the defects at the interface, which is similar to the case of p-$BaSi_2$/n-Si. The highest η is approximately 0.3% from sample D with $t_{BaSi:H}$ = 5 min. This value is much lower than H passivated B-doped $BaSi_2$/n-Si heterojunction solar cell due to several reasons. First, the electron concentration is reduced markedly by H passivation, in other words, the sharp pn junction cannot be formed. Second, according to the previous experiment, the trap centers are generated by excess H atoms. Third, the band offsets located at the heterointerface of n-$BaSi_2$/p-Si substrate because of a small electron affinity of $BaSi_2$ (3.2 eV) prevent the minority carrier transport [26]. Fourth, the thickness of Sb-doped n-$BaSi_2$ layer is around 300 nm, such thick n-$BaSi_2$ has a poor crystal quality and once again obstructs the minority-carrier transport. Figure 4.17(b) shows the photoresponsivity of these sample. All photoresponsivity starts to increase at the λ ~ 1200 nm. With increasing $t_{BaSi:H}$, the photoresponsivity between the λ of 800 and 1000 nm is increased, indicating that the defects at interface are reduced, matching the reduction of J_0. However, the photoresponsivity at λ < 800 nm is approximately zero, demonstrating that Sb-doped $BaSi_2$ layers do not make any contribution to the photogenerated current. Therefore, we can state that the η improvement is due to the defect reduction at the interface.

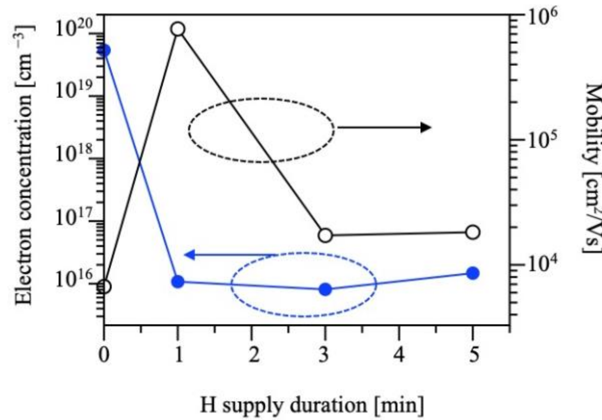

Fig. 4.15. Carrier concentration and mobility in H passivated Sb-doped n-$BaSi_2$.

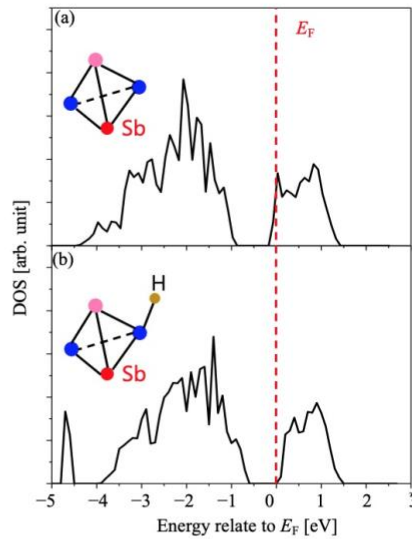

Fig. 4.16. Total density of states of $BaSi_2$ doped with Sb as a substitutional impurity in Si(3) site without H (a)

and with H (b).

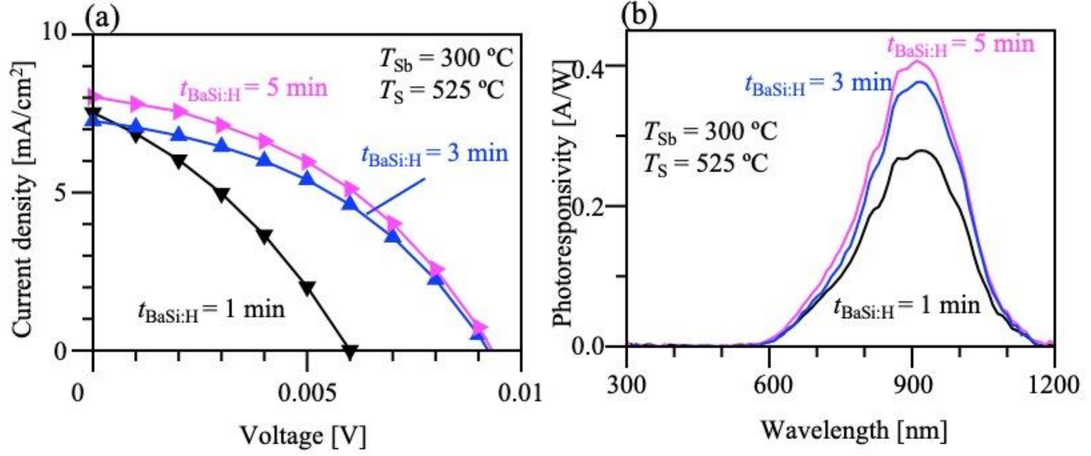

Fig. 4.17. (a) *J-V* curve of H passivated Sb-doped n-$BaSi_2$/p-Si under AM 1.5 illumination. (b) Photoresponsivity spectra of H passivated Sb-doped n-$BaSi_2$/p-Si without a bias voltage.

TABLE VI. Solar cell parameters of Sb-doped n-$BaSi_2$/p-Si with H passivation. Short-circuit density (J_{SC}), open-voltage (V_{OC}), fill factor (*FF*), conversion efficiency (η), series resistance (R_S), shunt resistance (R_{SH}), and reverse current density (J_0) are all summarized.

$t_{BaSi:H}$ (min)	J_{SC} (mA/cm^2)	V_{OC} (V)	*FF*	η (%)	R_S (Ω)	R_{SH} (kΩ)	J_0 (mA/cm^2)
1	7.52	0.06	0.33	0.14	161.7	4.5	0.019
3	7.26	0.09	0.41	0.27	99.6	14.1	0.016
5	8.03	0.09	0.41	0.3	99.6	10.7	0.022

4.2.3 Summary

The electron concentration of Sb-doped n-$BaSi_2$ is decreased by H passivation, which is not suitable to be n-type layer in $BaSi_2$ homojunction solar cells. Furthermore, the excess H atoms generate the localized states in the band gap region, and degrade the minority carrier properties. Therefore, we believe that H passivation has the negative effect on Sb-doped n-$BaSi_2$. In the next step of fabrication $BaSi_2$ homojunction solar cell, the Sb-doped n-$BaSi_2$ should be deposited after the H passivation.

4.3 Reference

1. M. A. Khan *et al.,* Appl. Phys. Lett. **104**, 252104 (2014).
2. S. Sugiyama *et al.,* Jpn. J. Appl. Phys. **59**, SFFA04 (2020).
3. M. Kobayashi *et al.,* Appl. Phys. Express **1**, 051403 (2008).
4. K. Kodama *et al.,* Jpn. J. Appl. Phys. **57**, 031202 (2018).
5. D. Chen *et al.,* Sol. Energy Mater. Sol. C. **185**, 174 (2018).
6. Z. Xu *et al.,* Phys. Rev. Mater. **3**, 065403 (2019).
7. M. Tajima, J. Cryst. Growth **103**, 1 (1990).
8. E. C. Lightowlers and V. Higgs, Phys. Status Solidi A **138**, 665 (1993).
9. M. Tajima *et al.,* J. Appl. Phys. **111**, 113523 (2012).
10. S. Shirakata and T. Nakada, Thin Solid Films **515**, 6151 (2007).
11. J. K. Larsen *et al.,* J. Appl. Phys. **118**, 035307 (2015).
12. P. M. P. Salome *et al.,* IEEE J. Photovoltaics **7**, 670 (2017).
13. A. Le Beris *et al.,* Energy Environ. Sci. **5**, 6225 (2012).
14. J. K. Katahara and H. W. Hillhouse, J. Appl. Phys. **116**, 173504 (2014).
15. T. Okamoto *et al.,* Jpn. J. Appl. Phys. **37**, 3894 (1998).
16. D. P. Halliday *et al.,* J. Cryst. Growth **186**, 543 (1998).
17. I. L. Braly, *et al.,* Nat. Photonics **12**, 355 (2018).
18. W. Shockley and W. T. Read, Jr. Phys, Rev. **87**, 835 (1952).
19. T. Deng *et al.,* Thin Solid Films **661**, 7 (2018).
20. J. R Sites and P. H. Mauk, Sol. Cells **27**, 411 (1989).
21. D. V. Lang, J. Appl. Phys. **45**, 3023 (1974).
22. N. Zhang *et al.,* Jpn. J. Appl. Phys. **52**, 04ER02 (2014).
23. P. Giannozzi *et al.,* J. Phys.:Condens. Matter **21**, 395502 (2009).
24. P. Giannozzi *et al.,* J. Phys.:Condens. Matter **29**, 465901 (2017).
25. D. Tsukahara *et al.,* J. Appl. Phys. **116**, 123709 (2014).
26. T. Deng *et al*., Sol. Energy Mater. Sol. C. **205**, 110244 (2020).

Chapter 5 Detecting H states in $BaSi_2$ by muon spin rotation

5.1 Introduction of muon spin rotation

Muon (μ^+) is an elementary particle similar to a proton with an electric charge of e^+, and a spin of 1/2, but with a much lighter mass. Table VII compares a μ^+ to a proton. The μ^+ is an unstable subatomic particle with a mean lifetime of 2.2 μs, much longer than many other sub atoms. It is first discovered in cosmic rays by Anderson and Neddermeyer and is first artificially produced at Berkeley in 1948 [1, 2]. Now, there are only four institutions that can produce μ^+ beam: 1. The CMMS continuous source at TRIUMF in Vancouver, Canada; 2. The SμS continuous source at the Paul Scherrer Institution (PSI) in Villigen, Switzerland; 3. The ISIS neutron and muon source and RIKEN-RAL pulsed sources at the Rutherford Appleton Laboratory in Chilton, United Kingdom; 4. The Japan Proton acceleration Research Complex (J-PARC) facility in Tokai, Japan, where a new pulsed source is being built to replace that at KEK in Tsukuba, Japan. In this chapter, we use the facility in J-PACR, Japan to perform muon spin rotation (MuSR).

TABLE VII. Properties of muon and proton

	Muon	Proton
Mass (m_e)	206.7683	1836.15
Spin	0.5	0.5
Gyromagnetic ratio (γ)	8.5×10^8	2.7×10^8
Lifetime [μs]	2.19709	stable

Fig. 5.1. Aerial view of J-PACR at Tokai mura.

Some amount of μ^+ exit in nature, where protons come from the universe collide with a nucleus composing the air, and then pions (π^+) and other secondary particles are generated. These π^+ decay into μ^+ and electrons. The flux of μ^+ in nature is 1/100 cm^2/s. In other words, one muon passes through your palm every second. However, the natural μ^+ has a high and widely distributed energy, and is not suitable to perform experiments due to the large noise. Therefore, it is necessary to produce μ^+ artificially. At present, μ^+ is mainly generated by the accelerator, but a small amount of μ^+ is from the nuclear power station. It has a high yield of

approximately 10^7 cm^2/s and can be controlled to stop in a small sample, such as metal or semiconductor bulk. The artificial μ^+ are created using the same method of particle collision as well. Figure 5.1 shows the μ^+ facility in J-PARC. There are three accelerators including two synchrotrons and one linac to accelerate protons, then, the high speed protons hit the graphite target. After the hitting, the π^+ appear and decay to the μ^+ and neutrino. In J-PARC, the energy of accelerated proton is 3.0 GeV and can produce the flux of μ^+ at 4×10^8 cm^{-2}/s. Figure 5.2(a) shows the high energy photon hits carbon to generate pion. Figure. 5.2(b) shows the decay of π^+, wherein the spin of π^+ is 0, and the neutrino spin is left-handed in order to keep the angular momentum conservation. On the other hand, the μ^+ is right-handed and polarized. After 2.2 μs of the μ^+ lifetime, the μ^+ decay into a positron (e^+), which is emitted along the μ^+ spin direction. According to parity violation in weak decay [3], decayed positron angular distribution is dependent on μ^+ spin. By detecting emitted positrons, we know the spin direction of μ^+. Figure. 5.3 shows the MuSR instrument in J-PARC. A forward counter (N_F) and a backward counter (N_B) are used to detect emitted positrons in the forward and backward directions, which are expressed by Eq. 5.1. P is the μ^+ spin polarization. θ is the angle between μ^+ moving direction and electron detector. τ is μ^+ lifetime of 2.2 μs. To obtain P, we apply Eq. 5.2, where P can be evaluated by counting emitted positrons from the forward and backward detectors. Usually, in J-PARC, θ = 50º; therefore, the maximum value of P is 21%. Two kinds of magnetic field (B) in perpendicular or parallel can be applied to initial μ^+ polarization which are TF and LF mode, respectively.

$$N(e^+) = N_0\left(1 + \frac{1}{3} \times P \times cos\theta\right)\exp\frac{-t}{\tau}. \qquad (5.1)$$

$$\frac{[N_F(e^+) - N_B(e^+)]}{[N_F(e^+) + N_B(e^+)]} = \frac{1 \times P \times cos50°}{3} < 21\%. \qquad (5.2)$$

H is a ubiquitous impurity which exists widely in semiconductors. It has a great effect on the properties of semiconductors. However, H is not easy to detect its position, concentration, or energy level in the band gap region, because the mass of H is light. In chapter 3, we have measured the H concentration by SIMS. The H concentration at the surface is very high probably caused by the contamination by air or during the fabrication. Other information, such as the H role in photoresponsivity improvement, cannot be obtained by SIMS. MuSR is one of the possible methods to simulate H behavior and acquire more H information in semiconductors. In MuSR measurement, a positively charged spin-polarized μ^+ is first implanted into the semiconductor. Then, the μ^+ binds an electron to form a muonium (μ^+e^-); therefore, the local electronic structure of μ^+ is virtually equivalent to that of H after a small correction due to a difference in the reduced mass. Table VIII shows the comparison between H and μ^+e^-.The spin motion of μ^+ is significantly affected by the captured electron or even the neighboring nucleus in the material, and gradually decays. The decay of the μ^+ into a e^+ occurs after a mean lifetime of approximately 2.2 μs, and the emitted e^+ provides information on the spin direction of the parent μ^+. Figure 5.4 shows the μ^+ experiment in MuSR. MuSR has been applied to evaluate H in many semiconductors. For example, it reveals that H atoms behave as shallow donors in GaN. Moreover, the position of μ^+ is estimated at either the anti-bond center or bond-center of nitrogen using the hyperfine constant of μ^+e^-[4, 5]. These results explain why high hole concentrations are difficult to achieve in Mg-doped GaN. This is because H is one of the most common impurities in semiconductors and affects the conductivity type of GaN. The shallow donor μ^+e^- is also measured in II-VI semiconductor such as CdS, CdSe, CdTe, and ZnO. In these cases, the shallow μ^+e^- is attributed to μ^+e^- being bound to the anion of the II-VI compound and be located at the anti-bond site or close to it in the bond direction [6]. The H atoms are more likely to be located at the bond-center site in both Si and Ge, which are revealed by MuSR measurement [7].

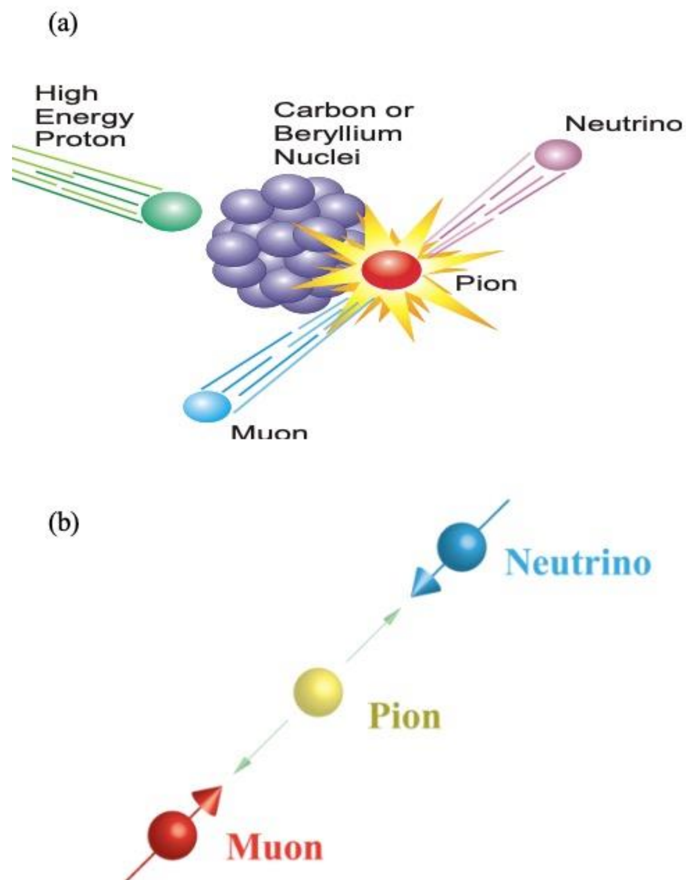

Fig. 5.2. (a) Generation of pion particle. (b) Pion particle decays to muon.

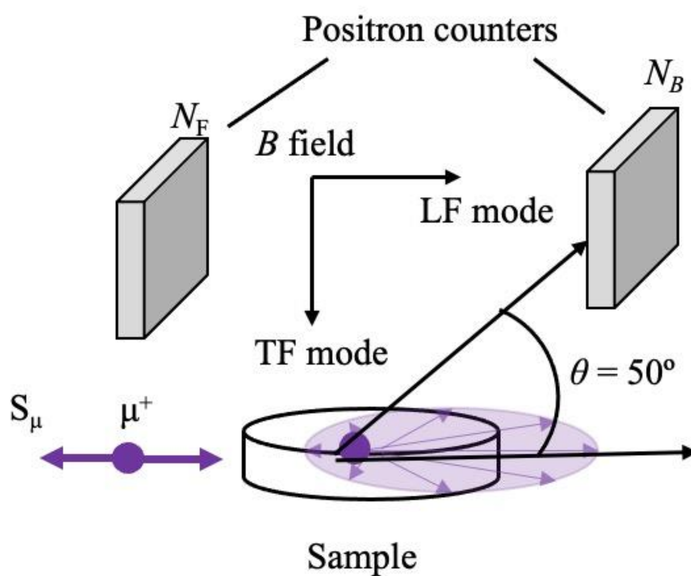

Fig. 5.3. MuSR measurement facility in J-PARC.

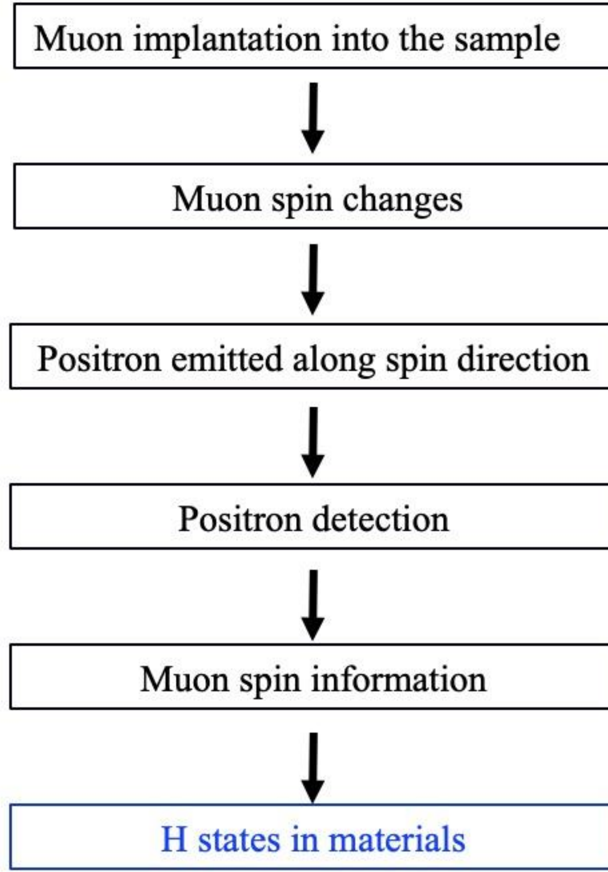

Fig. 5.4. Procedure of MuSR experiment.

TABLE VIII. Properties of muonium and hydrogen

	Muonium	Hydrogen
Reduced electron mass (m_e)	0.995187	0.999456
Ground state radius [Å]	0.531	0.529
Ground state energy [eV]	–13.5403	–13.5984
Hyperfine Freq. [GHz]	4.46	1.42

We next introduce the theoretical expression of MuSR spectroscopy. A spin-polarized μ^+ beam enters to a material, some μ^+ form μ^+e^- and some remain unchanged. The fraction of the remained μ^+ is largely dependent on materials. For example, almost all μ^+ remain in metals because the bonds between the host material nuclear and its electron is strong, while, in the semiconductor, the inserted μ^+ is more likely to bond a valance electron and form a μ^+e^-. In a μ^+e^-, the spin magnetic moments of the μ^+ and electron interact with each other via the hyperfine interaction, and they themselves, both interact with B via Zeeman effect. μ^+e^- may also have additional experience so called a nuclear hyperfine interaction with neighboring host nuclei with spin. However, in general, this interaction is much smaller than that of μ^+ and electron, which can be ignored. All these interaction can affect the μ^+ spin polarization, which, consists of a sum of undamped oscillating components. Using the theory of quantum mechanics, the spin Hamiltonian operator of μ^+e^- can be expressed by

$$\hat{H} = \omega_e \widehat{S_Z} - \omega_p \widehat{I_z} + \omega_0 \hat{S}\hat{I}. \quad (5.3)$$

Here, we assume that the B is applied along the z axis for a simple case. $\hat{H}$ is the Hamiltonian operator, ω_0

is the hyperfine frequency, $\widehat{S_Z}$ and $\widehat{I_Z}$ are the electron and μ^+ spin operators, respectively. ω_e and ω_p are the precession frequencies of isolated electron and μ^+, respectively, and expressed by

$$\omega_p = 2\pi \times 135.53 \times B. \quad (5.4)$$

$$\omega_e = 2\pi \times 28024.21 \times B. \quad (5.5)$$

Then, the spin Hamiltonian operator can be applied to a basis set of product spin functions including $|\alpha\alpha\rangle$, $|\alpha\beta\rangle$, $|\beta\alpha\rangle$, $|\beta\beta\rangle$. Here, α (β) means spin up (spin down). The first and second letter in the state describe the muon spin and electron spin, respectively.

$$E_1 = 1/2(\omega_e - \omega_\mu + 1/2\omega_0) \text{ for } |\alpha\alpha\rangle. \quad (5.6)$$

$$E_2 = 1/2[(\omega_e + \omega_\mu)2 + \omega_0]1/2 - 1/4\omega_0 \text{ for } c|\alpha\beta\rangle + s|\beta\alpha\rangle. \quad (5.7)$$

$$E_3 = -1/2[(\omega_e + \omega_\mu)2 + \omega_0]1/2 - 1/4\omega_0 \text{ for } c|\beta\alpha\rangle - s|\alpha\beta\rangle. \quad (5.8)$$

$$E_4 = -1/2(\omega_e - \omega_\mu - 1/2\omega_0) \text{ for } |\beta\beta\rangle. \quad (5.9)$$

According to Eqs. 5.6 to Eq. 5.9, the Breit-Rabi diagram is shown in Fig. 5.5. We can obtain the hyperfine frequency between two states and reproduce it by the first-principles calculations, then, the exact muon or H position will be known. In this chapter, the hyperfine frequency is originated from oscillation between $|2\rangle$ and $|4\rangle$.

In chapters 3 and 4, the significant improvement of photoresponsivity of H passivated undoped and B-doped $BaSi_2$ are explained from the viewpoint of minority carrier properties. However, the effect of H is still unclear. Thus, in this chapter, we will apply MuSR to $BaSi_2$. This is first time to investigate H states in $BaSi_2$ using MuSR. We report on the observation of the paramagnetic μ^+e^- spectrum in $BaSi_2$. The calculated μ^+e^- state has a hyperfine parameter equivalent to a magnetic field of 8.8 mT. Furthermore, the energy level within the band gap region of this muonium is estimated to be approximately 31 meV below the conduction band minimum of $BaSi_2$, as determined from the measured activation energy for thermal ionization.

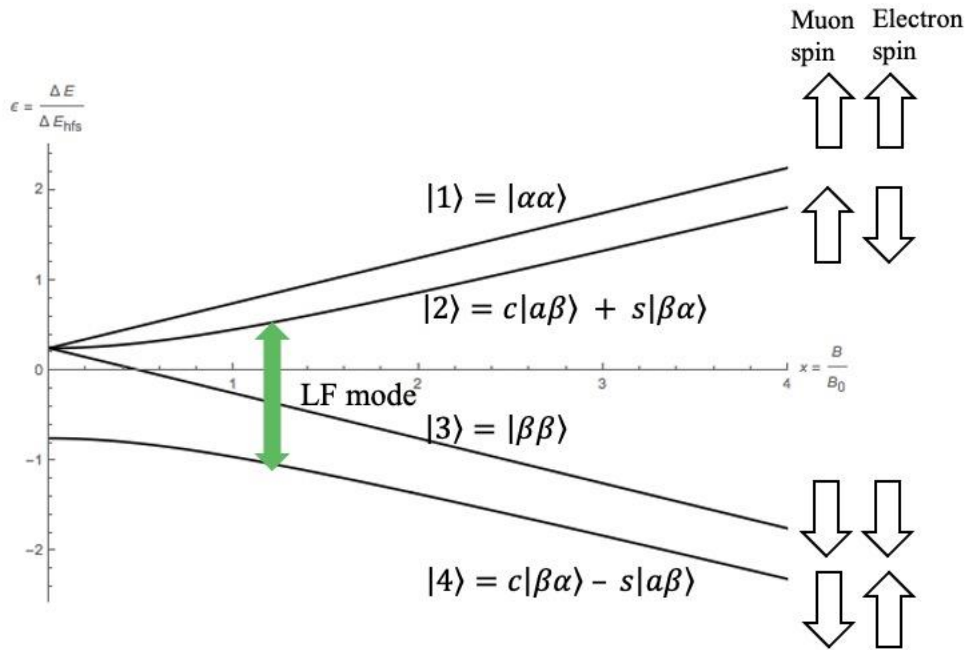

Fig. 5.5. Breit-Rabi diagram.

5.2 Experiment

We fabricate 500-nm-thick $BaSi_2$ epitaxial films on a low-ρ n^+-Si(111) substrate by co-depositing Ba and Si atoms via MBE method. The 500-nm-thick $BaSi_2$ films are irradiated by atomic H produced by an RF plasma generator for various $t_{BaSi:H}$ from 0 to 30 min at T_S =580 ºC. The vacuum level and power of the plasma

generator are kept at 10^{-3} Pa and 10 W, respectively. Finally, a 3-nm-thick a-Si is deposited at T_S = 180 ºC as a surface passivation layer. PL measurements are carried out at 8 K by exciting the samples from the $BaSi_2$ side. The instrument of PL has been introduced in chapter 4.

Conventional MuSR experiments are performed using the ARTEMIS spectrometer installed in the MLF S1 Instrument of the J-PARC. These experiments measured the time-dependent muon decay asymmetry $A(t)$ under a zero field of LF mode and weak TF mode, where the B is set to 2 mT. A 100% spin-polarized pulsed μ^+ beam with a full width at half maximum of around 100 ns and momentum of 27 MeV/c is used to irradiate a polycrystalline stoichiometric $BaSi_2$ sputter target (Tosoh Corporation) loaded on a He-flow cryostat to monitor $A(t)$ over a temperature range from 6 to 300 K.

In order to estimate possible energy positions of defect levels caused by atomic H in the interstitial sites in the $BaSi_2$ bulk we have implemented the first-principles total energy projector-augmented wave method (code VASP) as mentioned in chapter 3. We set the energy cutoff at 325 eV.

5.3 Results and discussions

Figure 5.6(a) shows the PL spectra of these samples measured at 8 K. The PL intensity significantly depended on $t_{BaSi:H}$. $BaSi_2$ is an indirect band gap semiconductor; therefore, its PL can be ascribed to the radiative transition of electrons between localized states within the band gap region. In the reference sample ($t_{BaSi:H}$ = 0 min), we observe weak and broad PL. This PL spectrum is reproducible by two Gaussian curves with peaks at 0.81 and 0.99 eV as shown in Fig. 5.6(b). The energy of 0.81 eV is approximately 0.5 eV smaller than the E_g of $BaSi_2$, indicating that the presence of deep defect levels and that the photogenerated carriers in $BaSi_2$ film recombined via such defect levels. As $t_{BaSi:H}$ increases to 1 and 5 min, the PL intensity becomes higher in Fig. 5.6(a). The PL spectra of these samples can also be fitted by two Gaussian curves in Fig. 5.6(b). As $t_{BaSi:H}$ increases much further, however, the PL intensity starts to decrease. Note that the PL at around 0.8 eV, corresponding to radiative transition of electrons between deep localized states, disappeared in samples at $t_{BaSi:H} \geq$ 5min. According to the Shockley-Read-Hall recombination model, deep levels promote recombination of photogenerated carriers more than shallow levels. Therefore, we attribute the photoresponsivity enhancement of H passivated undoped $BaSi_2$ to the reduction of deep defect levels in $BaSi_2$. We should not overlook the fact that the $t_{BaSi:H}$ for the highest photoresponsivity is different from that of the highest PL. This difference is attributed to the difference in carrier recombination mechanism between the PL and photoresponsivity. In the case of photoresponsivity, carrier recombination of any kind degrade the photoresponsivity. In contrast, the PL intensity decreases by nonradiative recombination. Therefore, we interpret the $t_{BaSi:H}$ dependences of photoresponsivity and PL as follows. With increasing $t_{BaSi:H}$ up to 5 min, the nonradiative recombination rate decreased, and thus the PL intensity increased. For further increase of $t_{BaSi:H}$ up to 15 min, the radiative recombination rate also decreased, leading to the increase of photoresponsivity and the decrease of PL. However, for much further increase of $t_{BaSi:H}$, the nonradiative recombination rate started to increase, decreasing both the photoresponsivity and PL. At present, there is not enough evidence to trace the origin of defect levels. Thus, we cannot explain the reason why nonradiative recombination occurs. In the future study, we may focus to investigate the defects in more details.

We next move on to the results of MuSR spectra. Figure 5.7(a) shows the MuSR asymmetry time spectra obtained at 6, 96, and 300 K under a TF mode at B = 2 mT for $BaSi_2$. The implanted μ^+ are found to be in the diamagnetic state above 6 K. The data points are thus fitted to

$$A(t) = A_0 \exp(-\lambda t) \cos(\omega_\mu t + \varphi). \quad (5.10)$$

Here, A_0 is a coefficient related to the amount of μ^+, λ is the damping coefficient, and ω_μ is the precession frequency of μ^+ given by $\gamma_\mu B$, where γ_μ is the μ^+ gyromagnetic ratio equal to $2\pi \times 135.5$ MHz/T; t is the time; and φ is the phase of the corresponding decay positron detector. The activation energy E_a for μ^+e^- ionization is

found to be approximately 31 meV by fitting the fractional yield in Fig. 5.7(b) with the function of $\beta_1 + \beta_2 \exp(-E_a/k_BT)$ over the temperature range from 71 to 196 K. Here, β_1 and β_2 are coefficients which are related to the facility and density of level E_a respectively, k_B is the Boltzmann constant, and T is the absolute temperature. This activation energy represents a direct transition from the defect level to the conduction band minimum. This result suggests that atomic H in $BaSi_2$ acts as a shallow donor and would contribute to the unintentional n-type conductivity of $BaSi_2$. On the basis of these results, the reason for the marked enhancement of photoresponsivity by atomic H supply is considered as follows. Deep defect levels due to V_{Si} are filled by electrons donated by the shallow donor level of atomic H. Therefore, they no longer can accept photogenerated electrons, meaning that these deep levels are made inactivated by atomic H. When the H content increases further, the electron concentration (majority carriers) increases, leading to the reduction in photoresponsivity. In line with this assumption, the measured charge carrier concentrations and Hall mobilities of 500-nm-thick $BaSi_2$ layers at RT are p-type, $p = 1.1 \times 10^{17}$ cm^{-3}, hole mobility $\mu_p = 25$ cm^2/Vs ($t_{BaSi:H} = 1$ min), $p = 1.8 \times 10^{17}$ cm^{-3}, hole mobility $\mu_p = 97$ cm^2/Vs ($t_{BaSi:H} = 15$ min), and n-type, $n = 9 \times 10^{15}$ cm^{-3}, electron mobility $\mu_n = 1240$ cm^2/Vs ($t_{BaSi:H} = 30$ min). These results reveal that the type of majority carriers changed from holes to electron as $t_{BaSi:H}$ is increased from 1 to 30 min.

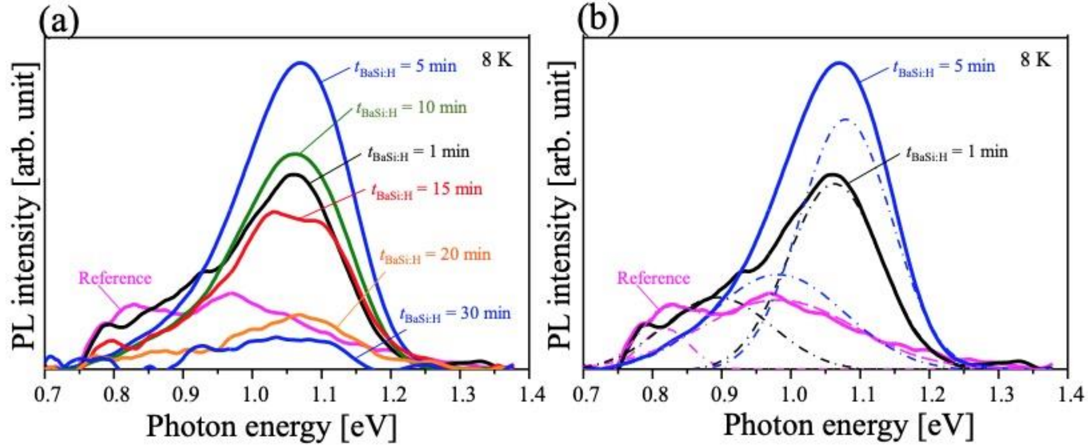

Fig. 5.6. (a) PL spectra of 500-nm-thick $BaSi_2$ with H passivation. (b) PL spectra are fitted by Gaussian curves.

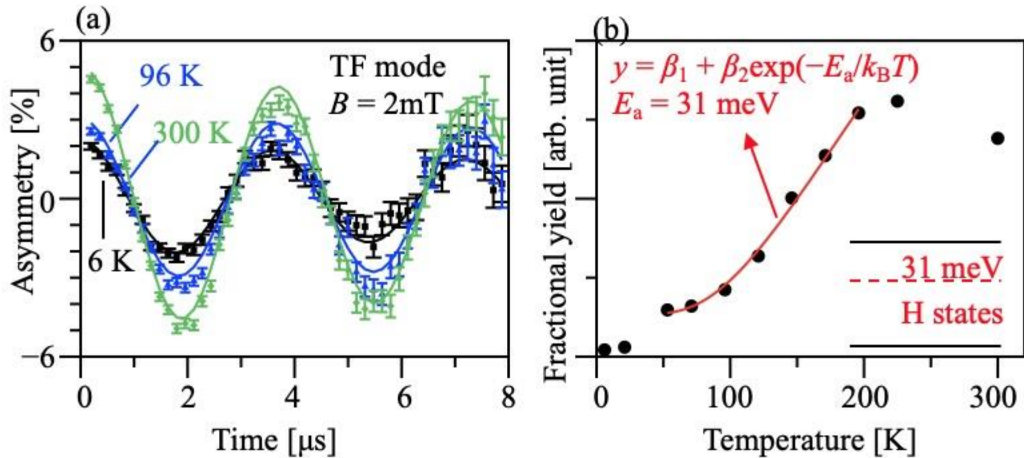

Fig. 5.7. (a) Asymmetric MuSR time spectra in $BaSi_2$ at $B_{TF} = 2$ mT measured at 6, 96, and 300 K. (b) Fractional yield of a diamagnetic state against temperature. The red solid curve is the fitting result.

In chapter 3, the significant photoresponsivity enhancement is due to the increase of carrier lifetime by atomic H passivation of V_{Si}, meaning that H atoms saturate dangling bonds at V_{Si}. However, it is hard to believe that all atomic H are involved to neutralize Si dangling bonds caused by the presence of V_{Si}, we have also investigated possible changes in the $BaSi_2$ energy spectrum if atomic H is present as an interstitial impurity. This issue has been earlier studied by identifying two distinct cases. Thus, if the first neighbors of a H atom are two Ba atoms, $BaSi_2$ behaves as a degenerate semiconductor because the Fermi level crosses the conduction band, as shown in Fig. 5.8(a). It is similar to the situation when one electron is added to the system. The second case is shown in Fig. 5.8(b), if the first neighbors of a H atom are two Si and two Ba atoms providing a localized peak in the energy spectrum located close to the middle of the gap in the corresponding DOS. This peak can be viewed as a half-filled state and it is due to the H-*s*, Si-*s*, Si-*p* states (Si atoms belong to the same tetrahedron with two Si atoms bonded to H). In addition to that we could detect the third case which is shown in Fig. 5.8(c) if the first neighbors of a H atom are one Si atom and one Ba atom. Here a localized half-filled state appears approximately 40 meV below the bottom of the conduction band. It can be treated as a shallow donor level in perfect agreement with this MuSR experiment data. We have identified the H-s, Ba-d, Si-s, and Si-p states (Si atoms belong to the same tetrahedron with one Si atom bonded to H and Ba atom is the neighbor to H atom) to define this shallow donor level. Moreover, it is necessary to point out here, the most stable case in the total energy is the one with the shallow donor level which is presented in Fig. 5.8(c), while, the least stable case is a degenerate semiconductor in Fig. 5.8(a).

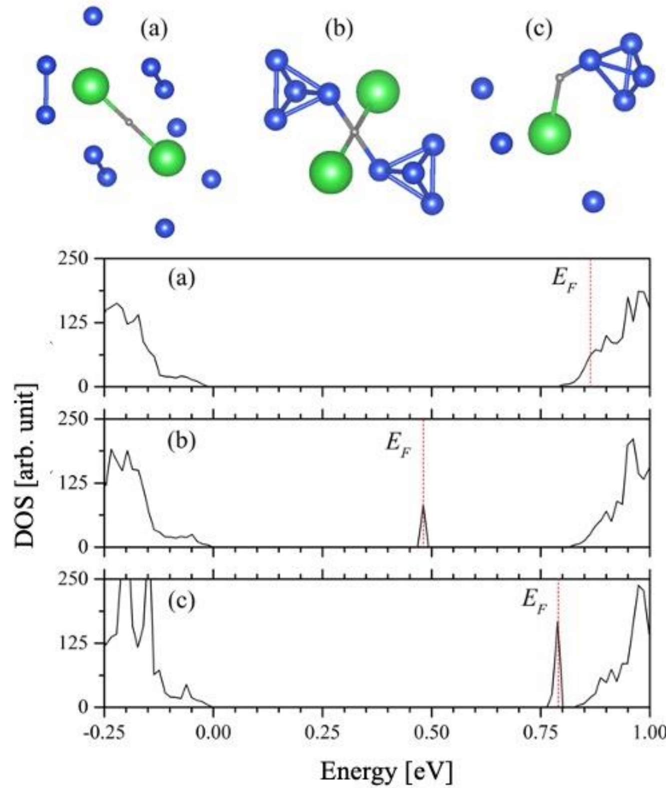

Fig. 5.8. Total density of states of $BaSi_2$ with atomic H acting as an interstitial impurity at different sites.

Figure 5.9(a) shows the MuSR spectra at 50 K under different longitudinal external magnetic fields of 0−35 mT. The increase of $A(0)$ from 4% to approximately 20% as B increases from 0 to 35 mT clearly indicates that a fraction of μ^+ forms a paramagnetic state. Under the LF mode, wherein B is applied parallel to the initial spin polarization, the time evolution of μ^+ spin polarization for the μ^+e^-like paramagnetic states $p(t,b)$ is described

by that of the spin-triple (F = 1) and spin singlet (F = 0) states, and is given by

$$p(t, b) = \frac{1}{2(1+b^2)}[(1+2b^2) + \cos\omega_b t], \tag{5.11}$$

where, ω_b is the μ^+ spin precession frequency for the $F = 0$ state and $b = B/B_C$, and B_C is the effective magnetic field corresponding to the magnitude of the hyperfine parameter. The second term in Eq. (11) can be zero because the observed time is very small. The residual polarization (= 1/2 for B = 0) therefore corresponds to the F = 1 state. As shown in Fig. 5.9(b), the experimental data are reproduced well by setting B_C = 8.8 mT. This value is equivalent to a frequency of 246 MHz and is about 1/18 that in vacuum (4.46 GHz). From this value, we estimate the Bohr radius in $BaSi_2$ to be increased by $(18)^{1/3} \approx 2.6$ via charge screening. This value agrees relatively well with that calculated using the effective electron mass of $m_e = 0.4m_0$ (m_0 is the free electron mass) and dielectric constant (ε = 14) of $BaSi_2$ in a sample hydrogen-atom model.

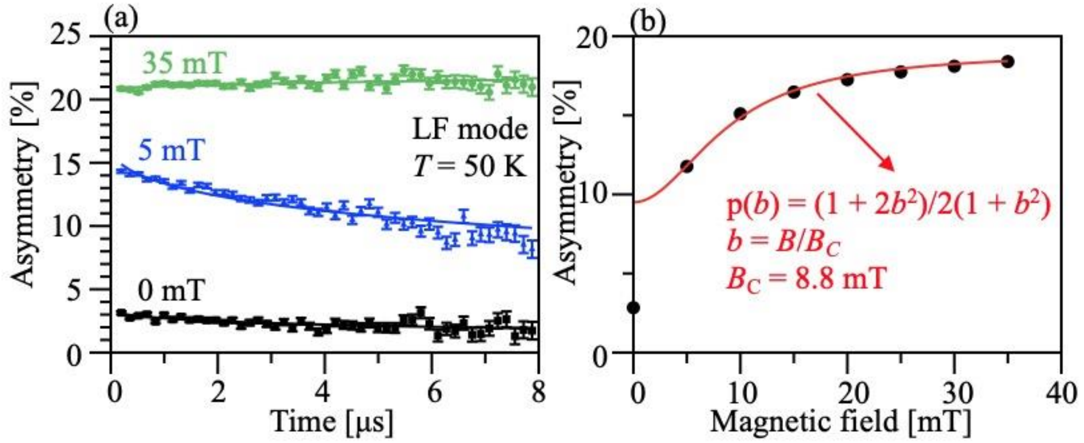

Fig. 5.9. (a) Asymmetric MuSR time spectra measured at 50 K. The data points are experimentally obtained, and the curves are the fitting results. (b) Initial asymmetry against B_{LF} and its fitting curve at 50 K. The magnetic field corresponding to the hyperfine parameter is estimated to be 8.8 mT.

5.4 Summary

We have demonstrated the highest photoresponsivity ever reported in 500-nm-thick $BaSi_2$ films passivated with atomic H. This directly verifies the contribution of atomic H to improving minority-carrier properties of $BaSi_2$ thin films. A paramagnetic μ^+e^- is confirmed in $BaSi_2$ by MuSR. The temperature dependence of the yield for this state shows that H in $BaSi_2$ acts as a shallow donor with an activation energy of approximately 31 meV. The presence of such shallow donor level is verified by *ab initio* studies when a H atom is located at an interstitial site and its first neighbors are one Si atom and one Ba atom. The hyperfine parameter obtained is approximately 246 MHz (8.8 mT).

5.5 Reference

1. S. H. Neddermeyer and C. D. Anderson, Phys. Rev. **51**, 884 (1937).
2. Y. Nishina *et al.,* Phys. Rev. **52**, 1198 (1937).
3. T. D. Lee and C. N. Yang, Phys. Rev. **104**, 254 (1956).
4. K. Shimomura *et al.,* Phys. Rev. Lett. **92**, 135505 (2004).
5. H. Amano *et al.,* Jpn. J. Appl. Phys. **28**, L2112 (1989).
6. J. M. Gil et al., Phys. Rev. B **64**, 075205 (2001).
7. B. D. Patterson, Rev. Mod. Phys. **60**, 1 (1988).

Chapter 6 Conclusion and prospects

My thesis focused on the H passivation on $BaSi_2$ as a new material for solar cell applications. The obtained results and the significant contributions can be summarized as follows:

1. It is the first time to demonstrate that H passivation is effective to improve the photoresponsivity of $BaSi_2$ thin films. We irradiate atomic H to 500-nm-thick $BaSi_2$ film at a substrate temperature of 580 ℃ for 15 min using an RF plasma generator. The photoresponsivity reaches a maximum value of 2.5 A/W at a wavelength of 800 nm under a bias voltage of 0.3 V. It is approximately ten times higher than the highest value previously reported for $BaSi_2$ thin film. We believe that the photoresponsivity improvement is because H atoms occupy the V_{Si}, located at Si(3) site in the Si tetrahedron, and passivate point defects there in $BaSi_2$. The microwave-photoconductivity decay measurement reveals that the minority-carrier lifetime of 500-nm-thick $BaSi_2$ film with the highest photoresponsivity is 14 μs, equals its bulk carrier lifetime ever reported. To explain the results of microwave-photoconductivity decay, we apply Auger recombination and various trap-related recombination mechanisms. The calculated trap concentration is decreased from 10^{13} to 10^{12} cm^{-3} after H incorporation. These estimates are in good agreement with previous experimental results. *Ab initio* studies show that the localized states become inactive because the Fermi level is positioned above the localized states when two H atoms occupy the V_{Si}. It is used to explain that the photoresponsivity improvement depends on H supply duration.

2. H passivation is suitable to improve the optical properties of lightly B-doped $BaSi_2$ films and undoped $BaSi_2$ films, whereas it is not useful to boost the optical properties of heavily B-doped $BaSi_2$ films and Sb-doped $BaSi_2$ films. The highest photoresponsivity of 4 A/W at a wavelength of 800 nm is obtained by H passivated lightly B-doped $BaSi_2$ when a bias voltage is 0.3 V, indicating that it has great potential to be an absorber layer in $BaSi_2$ homojunction solar cells. The hole concentration of lightly B-doped $BaSi_2$ films does not change so much with H passivation, which is approximate 10^{16} cm^{-3}. *Ab initio* studies also show that the localized states become inactive because the Fermi level is positioned above the localized states when only one H atom incorporates in lightly B-doped $BaSi_2$. This is the reason why the H supply duration for lightly B-doped $BaSi_2$ is shorter than that for undoped $BaSi_2$.

3. Atomic H approaches the $BaSi_2$/Si heterointerface and reduces the interface defects significantly. It is confirmed by deep-level transient spectroscopy. Without H passivation, the majority carrier (electron) traps exist at the interface of p-$BaSi_2$/n-Si. These interface defects cause a relative large reverse saturation current density and a low η. With H passivation, H atoms diffuse to the interface. The majority carrier (electron) traps are reduced significantly. Thus, the η is improved from 2.6% to 6.2%. This η will be further improved when we have an excellent growth chamber condition, such as a higher vacuum level, a stable R_{Ba}/R_{Si}.

4. The electron concentration of Sb-doped $BaSi_2$ is decreased from 10^{19} to 10^{16} cm^{-3} due to H passivation. We think that it is due to one electron of the Sb atom connects to one electron of the H atom. Therefore, H passivated Sb-doped $BaSi_2$ is not suitable to be an n-type layer in *pn* junctions. Although, the η of Sb-doped n-$BaSi_2$/p-Si is improved by H passivation because the interface defects are reduced, similar to the H passivated p-$BaSi_2$/n-Si heterojunction. The η of n-$BaSi_2$/p-Si is much lower than p-$BaSi_2$/n-Si, due to the low electron concentration of H passivated Sb-doped $BaSi_2$.

5. Atomic H induces a shallow localized state below the conduction band minimum of 31 meV, which is

revealed by muon spin rotation. According to first-principles calculations, the trap states are occupied by electrons from the shallow localized state and become inactive. This is why H passivation improves the photoresponsivity of $BaSi_2$ thin films. Two kinds of H position in $BaSi_2$ were proposed by the first-principles calculation. One is that H connects to one Si atom and one Ba atom. The other one is that H occupies V_{Si}. So far, we do not have enough evidence to state which one is more probably in H passivated $BaSi_2$. Thus, further investigation should be carried on.

Prospects:

1. At present, discussions about the position of H based on the MuSR experiments performed in TRIUMF, Canada, with the help of first-principles calculation is ongoing, where a continuous muon beam is provided. Thus, all electron oscillations between the energy levels in Fig. 5.5 can be observed. With the help of the first-principles calculation, the muon or H position will be known in the near future.

2. We have confirmed that H passivation is an effective method to improve the optical properties of $BaSi_2$ thin film. Therefore, the next step is to apply H passivation to $BaSi_2$ homojunction solar cells. The η is considered to be improved due to the excellent optical properties of the H passivated light absorber layer. One potential problem is to prevent H atom diffusion to Sb-doped n-$BaSi_2$ layer and heavily B-doped p-$BaSi_2$ layer.

3. Trying to apply H passivation to the sputtered $BaSi_2$ is of particular importance. From the viewpoint of photoresponsivity, the sputtered $BaSi_2$ thin films have a larger photoresponsivity than those by MBE. Furthermore, the sputtering method is more practical than MBE. Thus, the H passivated sputtered $BaSi_2$ thin film is essential before industrial manufacture.

Acknowledge

Here, I want to thank many people, without whom it would be impossible for me to finish my Ph.D program.

First and foremost, I would like to gratefully appreciate my supervisor Prof. T. Suemasu, who has been a tremendous mentor for me, for his enthusiasm, patience, motivation, and broad knowledge. His advices on both research as well as life have been priceless and he always encourages me to enjoy the life in Tsukuba. As an international student, he helps me a lot not only on supporting me financially but also providing opportunities to attend international conferences. I could not have imagined having a better supervisor for my Ph.D study.

In addition to my supervisor, I would like to thank my thesis committee members, Prof. Y. Ohno, Prof. T. Sekiguchi, Prof. T. Sakurai and Prof. H. Udono, for letting my defense be an enjoyable moment, and for their brilliant comments and helpful suggestions.

I would also like to thank Dr. K. Toko, who is really a hardworking researcher. He is a good role model for me. Besides, I would express my appreciate to Prof. N. Usami, Dr. K. Gotoh of Nagoya University and Prof. K. Shimomura and A. Koda of KEK for MuSR in J-PARC, Prof. D. B. Migas and A. B. Filonov from Belarusian state University of Informatics and Radioelectronics for the first-principle calculates, Dr. K. Kojima, who helped us to complete MuSR in TRIUMF, Canada and discuss the obtained results.

Special thanks to Madam E. Ito, who helps me deal with the travel expense reimbursement every time after attending domestic or international conferences.

I would like to thank the lab members; W. Du, T. Deng, R. Takebe, T. Gushi, T. Sato, K. Moto, H. Murata, Y. Yamashita, K. Kodama, T. Imajo, R. Sugiyama, S. Sugiyama, T. Nishida, Louise Benincasa, S. Aonuki, M, Saito, M. Tsuji, T. Nemoto, T. Hirose,…… I will not forget the great moment when we travelled Nikko, Mt. Fuji, and Nasu during summer seminar. Your company made my study much easier and happier.

Thanks my girlfriend T. Wang to support and color my free time in Tsukuba.

Last but not the least, I must express my very profound gratitude to my parents. Words cannot express how grateful I am to my father and mother for all of the sacrifices they have made throughout my life.

January 2021

Xu Zhihao

Award

1. **Young Scientist Award**, 5th Asia-Pacific conference on semiconducting silicides and related material, Miyazaki, Japan, July. 23, 2019.

List of publications

2020:

1. **Z. Xu**, T. Sato, L. Benincasa, Y. Yamashita, T. Deng, K. Gotoh, K. Toko, N. Usami, A. B. Filonov, B. D. Migas, and T. Suemasu, “Atomic hydrogen passivation for photoresponsivity enhancement of boron-doped p-$BaSi_2$ films and performance improvement of boron-doped p-$BaSi_2$/n-Si heterojunction solar cells,” Journal of Applied Physics 127, 233104 (2020).

2. **Z. Xu**, T. Sato, J. Nakamura, A. Koda, K. Shimomura, A. B. Filonov, D. B. Migas, and T. Suemasu, “Hydrogen states in hydrogen-passivated semiconducting barium disilicide measured via muon spin rotation,” Japanese Journal of Applied Physics 59, 071004 (2020). (citations: 1)

3. T. Deng, **Z. Xu**, Y. Yamashita, T. Sato, K. Toko and T. Suemasu, “Modeling the effects of defect parameters on the performance of a p-$BaSi_2$/n-Si heterojunction solar cell,” Solar energy materials and solar cells 205, 110244 (2020).

4. S. Aonuki, Y. Yamashita, T. Sato, **Z. Xu**, K. Gotoh, K. Toko, Y. Terai, N. Usami, and T. Suemasu, “Significant enhancement of photoresponsivity in As-doped n-$BaSi_2$ epitaxial films by atomic hydrogen passivation,” Applied Physics Express 13, 051001 (2020).

5. L. Benincase, **Z. Xu**, T. Deng, T. Sato, K. Toko, and T. Suemasu, “Effects of boron and hydrogen doping on the enhancement of photoresponsivity and photoluminescence of $BaSi_2$ epitaxial films,” Journal of Applied Physics 59, SFFA08 (2020). (citations: 1)

2019:

1. **Z. Xu**, D. A. Shohonv, A. B. Filonov, K. Gotoh, T. Deng, S. Honda, K.Toko, N. Usami, D. B. Migas, V. E. Borisenko, and T. Suemasu, “Marked enhancement of the photoresponsivity and minority-carrier lifetime of $BaSi_2$ passivated with atomic hydrogen,” Physical Review Materials 3, 065403 (2019). (citations: 14)

2. T. Sato, Y. Yamashita, **Z. Xu**, K. Toko, S. Gambarelli, M. Imai, and T. Suemasu, “Correlation of native defects between epitaxial films and polycrystalline $BaSi_2$ bulks based on photoluminescence spectra,” Applied Physics Express 12, 111001(2019). (citations: 2)

3. L. Benincasa, H. Hoshida, T. Deng, T. Sato, **Z. Xu**, K. Toko, Y. Terai, and T. Suemasu, “Investigation of defect levels in $BaSi_2$ epitaxial films by photoluminescence and the effect of atomic hydrogen passivation,” Journal of Physics Communications 3, 075005 (2019). (citations: 4)

4. T. Sato, C. Lombard, Y. Yamashita, **Z. Xu**, L. Benincase, K. Toko, S. Gambarelli, and T. Suemasu, “Investigation of native defects in $BaSi_2$ epitaxial films by electron paramagnetic resonance,” Applied Physics Express 12, 061005 (2019). (citations: 9)

2018:

1. **Z. Xu**, K Gotoh, T. Deng, T. Sato, R. Takabe, K. Toko, N. Usami, and T. Suemasu, “Improving the photoresponse spectra of $BaSi_2$ layers by capping with hydrogenated amorphous Si layers prepared by radio-frequency hydrogen plasma,” AIP Advance 8, 055306 (2018). (citations: 7)

2. T. Deng, T. Sato, **Z. Xu**, R. Takabe, S. Yachi, Y. Yamashita, K. Toko, and T. Suemasu, “p-$BaSi_2$/n-Si heterojunction solar cells on Si(001) with conversion efficiency approaching 10%: comparison with Si(111),” Applied Physics Express 11, 062301 (2018). (citations: 30)

2017:

1. **Z. Xu**, T. Deng, R. Takabe, K. Toko, and T, Suemasu, “Fabrication and characterizations of nitrogen-doped $BaSi_2$ epitaxial films grown by molecular beam epitaxy,” Journal of Crystal Growth 471, 37 (2017).

2. T. Deng, K. Gotoh, R. Takabe, **Z. Xu**, S. Yachi, Y. Yamashita, K. Toko, N. Usami, and T. Suemasu, “Boron-

doped p-$BaSi_2$/n-Si solar cells formed on textured n-Si(001) with a pyramid structure consisting of {111} facets," Journal of Crystal Growth 475, 186 (2017). (citations: 5)

List of conference (International only)

2019:

1. (Poster) **Z. Xu** et al., Investigation of hydrogen states in semiconducting $BaSi_2$ by muon spin rotation, Materials Research Meeting 2019, E3-13-p02, Yokohama, Japan Dec. 13, 2019.

2. (Oral) **Z. Xu** et al., Significant improvement on photoresponsivity and minority carrier lifetime of atomic H passivated $BaSi_2$ epitaxial films, The 5th Asia-Pacific Conference on Semiconducting Silicides and Related Materials July 21, 2019, Miyazaki, Japan.

3. (Oral) **Z. Xu**, et al., Significant improvement of optical properties of $BaSi_2$ due to atomic H passivation by radio-frequency plasma, 46th IEEE Photovoltaic Specialists Conference June 16-21, 2019, Chicago, USA.

4. (Oral) **Z. Xu**, et al., Significant photoresponsivity improvement of $BaSi_2$ films by using atomic hydrogen passivation, 2019 International Conference on Energy Materials and Nanotechnology, May 5, 2019, Wuhan, China.

2018:

1. (Poster) **Z. Xu,** et al., Optimal growth condition of hydrogenated amorphous silicon on $BaSi_2$ epitaxial film, Tsukuba Global Science Week Interdisciplinary Workshop on Science and patents 2018, IWP044, Tsukuba, Sept. 21, 2018.

2. (Poster) **Z. Xu**, et al., Improvement of photoresponsivity of passivated $BaSi_2$ thin film layers by hydrogenated amorphous Si using radio-frequency of H_2 plasma, 2018 International Conference on Solid State Devices and Materials (SSDM 2018), N-8-03, Tokyo, Japan, Sept. 13, 2018.

3.(Poster) **Z. Xu**, et al., Photoresponsivity improvement of $BaSi_2$ epitaxial films by capping with hydrogenated amorphous Si layer by radio-frequency H_2 plasma, 7th World Conference on Photovoltaic Energy Conversion, B8-583, Hawaii, USA, June 13, 2018.

2017:

1.(Poster) **Z. Xu,** et al., Nitrogen-doped $BaSi_2$ thin film on n-Si(111) by molecular beam epitaxy and radio-frequency plasma generator, 27th International Photovoltaic Science and Engineering Conference, 2TuPo.78, Shiga, Japan, Nov. 14, 2017.